THE UNIVERSITY *of* EDINBURGH

Probing the brain's white matter with diffusion MRI and a tissue dependent diffusion model

Jakub Przemysław Piątkowski

Doctor of Philosophy

Institute for Adaptive and Neural Computation
School of Informatics
University of Edinburgh

2013

Abstract

While diffusion MRI promises an insight into white matter microstructure in vivo, the axonal pathways that connect different brain regions together can only partially be segmented using current methods. Here we present a novel method for estimating the tissue composition of each voxel in the brain from diffusion MRI data, thereby providing a foundation for computing the volume of different pathways in both health and disease. With the tissue dependent diffusion model described in this thesis, white matter is segmented by removing the ambiguity caused by the isotropic partial volumes: both grey matter and cerebrospinal fluid. Apart from the volume fractions of all three tissue types, we also obtain estimates of fibre orientations for tractography as well as diffusivity and anisotropy parameters which serve as proxy indices of pathway coherence.

We assume Gaussian diffusion of water molecules for each tissue type. The resulting three-tensor model comprises one anisotropic (white matter) compartment modelled by a cylindrical tensor and two isotropic compartments (grey matter and cerebrospinal fluid). We model the measurement noise using a Rice distribution. Markov chain Monte Carlo sampling techniques are used to estimate posterior distributions over the model's parameters. In particular, we employ a Metropolis Hastings sampler with a custom burn-in and proposal adaptation to ensure good mixing and efficient exploration of the high-probability region. This way we obtain not only point estimates of quantities of interest, but also a measure of their uncertainty (posterior variance).

The model is evaluated on synthetic data and brain images: we observe that the volume maps produced with our method show plausible and well delineated structures for all three tissue types. Estimated white matter fibre orientations also agree with known anatomy and align well with those obtained using current methods. Importantly, we are able to disambiguate the volume and anisotropy information thus alleviating partial volume effects and providing measures superior to the currently ubiquitous fractional anisotropy. These improved measures are then applied to study brain differences in a cohort of healthy volunteers aged 25-65 years. Lastly, we explore the possibility of using prior knowledge of the spatial variability of our parameters in the brain to further improve the estimation by pooling information among neighbouring voxels.

Acknowledgements

Many thanks to my supervisors, Amos and Mark, for their professional guidance, but most of all for their support.
Many thanks to my parents, to Kamila and of course to Giulia.

Declaration

I declare that this thesis was composed by myself, that the work contained herein is my own except where explicitly stated otherwise in the text, and that this work has not been submitted for any other degree or professional qualification except as specified.

(*Jakub Przemysław Piątkowski*)

Table of Contents

Chapter 1

Introduction to diffusion MRI

Diffusion-weighted magnetic resonance imaging (MRI) is a modality uniquely suited to provide insight into the human neuroanatomy non-invaisvely and *in vivo*. In particular, it enables the segmentation of white matter fasciculi and assessment of their micro-structural coherence, based on the water diffusion anisotropy caused by highly ordered bundles of axons [81, 82]. Diffusion MRI is well established as an imaging technique of choice in ischæmic stroke [7]. It is also used to study brain changes in a range of (non-acute) conditions such as Alzheimer's disease, multiple sclerosis and schizophrenia [54, 72], as well as during healthy development [85] and ageing [106]. However, linking the measured MRI signal intensities with the underlying micro-structural properties of brain tissue remains challenging. This is principally due to the low contrast between grey and white matter in spin-echo echo-planar MRI volumes collected in this modality. Additionally, the imaging resolution (typically of the order of 8mm^3 compared to $1\text{–}2\text{mm}^3$ for structural T_1- and T_2-weighted scans) is limited compared to the thickness of most white matter pathways. As a result, volume elements (voxels) in a typical diffusion MRI experiment often contain more than one tissue type, for example cerebrospinal fluid and grey matter, a situation known as *partial voluming*. Modelling partial volumed data is difficult and in general the parameters estimated under single-tissue assumption do not correspond to any of the constituent tissue types. Current methods seem to focus on circumventing this fundamental problem by excluding the affected voxels from analysis. Prominent examples include constructing white matter skeleton in TBSS described on page 25 and stopping criteria for tractography (page 21). A general, direct modelling solution yielding reliable, uncorrupted results for all voxels has yet to be established; this work takes a step towards developing such a solution.

In this chapter we provide a brief introduction to the field of diffusion MRI, from the basics of water diffusion in brain tissue and its measurement with MRI to modelling and analysis approaches. We also describe how the results from many individuals can be pooled in group studies and discuss the usefulness of various techniques. Throughout the chapter, we focus on how partial voluming affects diffusion MRI analysis and results on various levels. This survey leads us to propose an explicit, physically plausible forward model of diffusion in partial volume voxels, a tissue dependent diffusion model. This new approach is fully developed in Chapter 2, validated in detail on data from human volunteers in Chapter 3 and applied to the study of brain changes in adulthood and the early stages of normal, healthy ageing in Chapter 4. Chapter 5 explores the possibility of using prior knowledge about the expected variability of the parameters of the brain tissue to further stabilise their estimation by pooling together information from neighbouring voxels. Discussion of the results, usefulness and limitations of our method, as well as of possible directions for future development follows in Chapter 6.

1.1 Looking into the tissue structure with diffusion MRI

1.1.1 Spontaneous transport of mass

Diffusion is a process of spontaneous, random displacement of liquid particles by the means of thermal motion, proportionally to their kinetic energy (for a thorough introduction, see for example Crank [38]). This microscopic phenomenon is difficult to observe directly with the naked eye; it manifests itself macroscopically when two liquids of different colours or opacities are brought in contact with one another in the same container: over time, they mix without external intervention until reaching a stable distribution, independent of their initial concentrations. Early quantitative measurements of this phenomenon were performed by Thomas Graham, a Scottish chemist; a macroscopic description in terms of flows and concentrations was later developed by Adolf Fick and inspired by Fourier's formulæ for the conduction of heat. According to Fick's first law:

$$\mathbf{J} = -\mathcal{D}\nabla C, \tag{1.1}$$

where $\mathbf{J}$ is the flow of fluid measured in units of volume per unit time, C the concentration and ∇ denotes the gradient operator (nabla). It has to be stressed that throughout this work we consider the diffusivity coefficients (or tensors) to be constant during the

measurement of the diffusion process — an assumption that seems reasonable given the short diffusion time of a typical experiment (50–100ms). In an isotropic medium, where the diffusivity properties are independent of the orientation, $\mathcal{D}$ is the scalar diffusivity constant (equivalently $\mathcal{D} = d\mathbb{I}$), indicating how easy it is for the liquid to flow and dependent on the viscosity of the environment. Under such conditions, Fick's law states that the liquid flows towards the decreasing gradient of concentration ($\mathbf{J} \parallel \nabla C$) so as to uniformize its spatial distribution. In a more general setting, where the properties of the medium depend on the orientation of its internal structures diffusivity can be described using a 3-by-3, symmetric, anisotropic diffusivity tensor $\mathcal{D}$ and the equation (1.1) expands into:

$$\begin{bmatrix} J_x \\ J_y \\ J_z \end{bmatrix} = - \begin{bmatrix} D_{xx} & D_{xy} & D_{xz} \\ D_{xy} & D_{yy} & D_{yz} \\ D_{xz} & D_{yz} & D_{zz} \end{bmatrix} \begin{bmatrix} \frac{\partial C}{\partial x} \\ \frac{\partial C}{\partial y} \\ \frac{\partial C}{\partial z} \end{bmatrix} \tag{1.2}$$

It is worth noting that in this case the flow vector needs not be aligned with the concentration gradient, $\mathbf{J} \nparallel \nabla C$. In an isolated system the change in concentration is entirely due to the diffusive flow; from this principle of the conservation of mass it follows that:

$$\frac{\partial C}{\partial t} = -\nabla \mathbf{J} \tag{1.3}$$

Substituting equation (1.1) for the flow $\mathbf{J}$ we obtain the diffusion equation (also known as Fick's second law):

$$\frac{\partial C}{\partial t} = \nabla(\mathcal{D}\nabla C) \tag{1.4}$$

One of the most interesting solutions of this differential equation is obtained when the initial concentration is a delta function $\delta(\mathbf{x})$, i.e. the diffusing substance is at first constrained to a single point. It turns out that in this case the concentration can be described by a Gaussian distribution with dispersion growing with time according to $\Sigma = 2\mathcal{D}t$. This solution provides a link to the molecular view of diffusion, which was discovered independently by Robert Brown, a Scottish botanist, through observations of big particles, such as grains of pollen, suspended in a liquid and undergoing jerky, random motion of unknown origin. Brownian motion was initially regarded as a separate phenomenon, unrelated to diffusion. The unification of the theory of Brownian motion and that of the mixing of liquids via diffusion was first proposed by Albert Einstein in his seminal papers from 1905 and 1906 (collected in [41]). Einstein was the first to derive the formula for the mean square displacement of a particle: $\langle |\mathbf{x}|^2 \rangle = 2\mathcal{D}t$, where $\mathcal{D}$ depends (only) on the size (mass) of the molecule, the temperature and the

viscosity of the medium. In his microscopic description, diffusion is a process where every molecule frequently collides with other molecules and environmental barriers, which renders its final location intractable. Statistical description, however, is still possible: for each molecule, the probability of diffusion by vector $\mathbf{x}$ during time t is quantified by a displacement distribution, $p_t(\mathbf{x})$. Analogically to the Gaussian formula for concentration when $C_{t=0}(\mathbf{x}) = \delta(\mathbf{x})$, we have:

$$p_t(\mathbf{x}) = \mathrm{N}(\mathbf{x}|\mu = 0, \Sigma = 2\mathcal{D}t) = \frac{1}{\sqrt{(4\pi t)^3|\mathcal{D}|}} \exp\left(\frac{-\mathbf{x}^T \mathcal{D}^{-1}\mathbf{x}}{4t}\right) \tag{1.5}$$

Under this unified framework the process of mixing two liquids through diffusion is described as one type (or species) of particles diffusing in the environment of solvent particles. However, it is easy to consider the situation in which the same substance is both the diffusing liquid and the medium. In this case the spontaneous movement of the molecules is usually referred to as self-diffusion. As we shall see in Section 1.1.3, the behaviour of self-diffusing liquid (usually water) can be measured during an MRI experiment, based on the movement of molecules with respect to a non-uniform magnetic field, for the purpose of indirectly examining the microstructure of the brain tissue.

1.1.2 Water diffusion in the brain

Similarly to the majority of biological tissue types, the brain's parenchyma contains large quantities of water molecules, making it the main diffusing species. At the same time, it is characterised by complex, diverse microstructure on the cellular and subcellular level, with numerous types of glial cells and neuronal morphologies. The movement of water molecules is thus impeded by a variety of obstacles, such as semipermeable membranes, macromolecules, cellular filaments and organelle. Given diffusion time of 50–100ms, used in many diffusion MRI experiments, the typical average distance covered by water molecules in the brain is around 1–15μm [18], compared to 17μm for free water[1]. It is also true that the displacement distribution is no longer Gaussian or dependent only on the local, intrinsic viscosity of the medium. Rather, it is determined by a mixture of the effects of various barriers and local medium properties. In general, the longer the diffusion time, the more the former dominate over the latter. This is why we can probe the microstructure of the neural tissue and infer its characteristics by studying statistical patterns of motion of water molecules.

[1] At 37°C, more than 30% of water molecules arrive at least this far from their starting point during 100ms, while only 5% are displaced by more than 34μm. This corresponds to a diffusion coefficient of 3×10^{-3}mm^2/s. Example after [18].

Biological function, physiology and anatomy vary between brain structures and regions; in general most of the obstruction to water diffusion is tissue-specific. In the cerebrospinal fluid diffusion is unrestricted and thus large and approximately isotropic. Accordingly, its diffusivity is similar to that of the free water. In grey matter, on the other hand, tightly packed neurons and glia hinder diffusing molecules significantly in all directions, which results in diffusion that is much slower than in the cerebrospinal fluid, but still nearly-isotropic (although a recent *ex vivo* study [78] shows that some structure can be seen in the cortex with highly effective acquisition parameters; cortical anisotropy has also been found in premature infants [85]). The situation is different for white matter, where coherent axonal bundles hinder diffusion more strongly perpendicular to their direction than in parallel. This introduces measurable anisotropy into the diffusion MRI signal [81, 82] and enables the reconstruction of local tract direction (which aligns with the direction of greatest diffusivity) as well as estimation of additional parameters of interest, based on the shape of the diffusion profile (see Section 1.2). It is still uncertain which cells or cellular structures are the primary source of the diffusion anisotropy in white matter. It is generally thought that myelin, the protective fatty coating around the axons, might be the leading factor, but measurable diffusion anisotropy has also been detected in the developing brain, before complete myelination [85]. Spatially coherent organisation of membranes and other cellular structures are also thought to play a role. The modelling work to date has failed to fully connect the measured signal attenuation to the underlying cellular substrate; in particular, the volumes of the estimated intra- and extracellular compartments (17.5% and 82.5%, respectively) do not agree with known true values [18].

The magnitude and anisotropy of water molecule diffusion in white matter have been linked to microstructural tract coherence, although it is still not entirely clear how this translates to pathway integrity and function. Nevertheless, numerous studies have examined the changes in quantitative diffusion measures in acute and chronic conditions [7, 54, 72] as well as during normal, healthy development [85] and ageing (e.g. [93, 105, 12, 75, 11]). We provide a brief overview of the ageing research in Section 4.1.2, before presenting the results of our own investigation of a cohort of healthy individuals between 25 and 65 years of age.

1.1.3 Measuring diffusion with MRI

MRI relies on manipulating the spin of molecules found in the examined tissue (see for example [95] for a general introduction). Often, the molecules in question are water's hydrogen nuclei, i.e. protons, H^+. Spin is a quantum, vector valued property of particles that is related, but not identical to classical angular momentum; in particular, it is an intrinsic property of the molecules and does not imply rotation around an axis. We shall sometimes refer to the hydrogen nuclei as spins, to emphasize the fact that this is the property we are primarily interested in. In this section we follow the semi-classical description of spin systems, whereby all spin orientations are allowed. While such description is not compatible with modern quantum mechanics, it is a sufficiently good approximation that allows an appropriately detailed description of the physics underlying MRI techniques. It also provides a good intuitive background for the experimental manipulations and their effects. Another crucial property of protons is their non-zero magnetic dipole moment, which for our purposes means that they behave like tiny bar magnets. This means that coherent motion of a population of spins can be detected by measuring the current induced in an appropriately placed receiver coil.

In the presence of external magnetic field $\mathbf{B}_0$ the spins of water protons tend to align with the field direction, producing non-zero net magnetisation: $\mathbf{M}_0 \parallel \mathbf{B}_0$. Their energy depends on the orientation of the spin vector: the parallel (or *up*) state has lower energy than the anti-parallel (*down*) state. The energy gap ΔE between these two states is small; at brain temperature the spins can flip spontaneously due to their thermal energy. This is why the net magnetisation of a collection of protons is small compared to the sum of their individual magnetic moments: the number of parallel spins is only marginally greater than that of anti-parallel ones (10 excess parallel spins in a million).

The alignment of spins with the external $\mathbf{B}_0$ field is not perfect: they precess around the $\mathbf{B}_0$ direction much like a rotating top in the earth's gravitational field. The frequency of this *Larmor* precession is proportional to the strength of the magnetic field:

$$\omega = \gamma B_0,$$

where γ is the gyromagnetic ratio (42.6MHzT^{-1} for protons) and $B_0 = |\mathbf{B}_0|$. It has to be noted that the spin precession is not macroscopically measurable because the precessing spins are out of phase and as a result the net magnetisation of the sample remains constant. ω is the resonant (Larmor) frequency of the protons; it also describes the size of the energy gap between up and down states: $\Delta E = \hbar\omega$. The most efficient

energy transfer occurs at the resonant frequency; for water at brain temperature and the magnetic field typical for a clinical MRI scanner (1.5T) this frequency corresponds to the radio frequency (RF) range, roughly 64MHz.

Using an additional magnetic field pulsating at the Larmor (RF) frequency, it is possible to excite some water protons, thus disturbing their equilibrium distribution. As all the excited spins are in phase with this RF field, the net magnetisation is no longer aligned with the direction of the static B_0 field. Instead, it is tilted at an angle dependent on the duration of the RF pulse and precessing around the B_0 direction (axis). The existence of transverse, oscillating components of the net magnetisation is the source of measured MRI signal: it induces electric current in the receiver coils located in the plane perpendicular to the main B_0 coil. Any angle between the field direction and the net magnetisation vector can be achieved by regulating the duration of the RF pulse; different pulses are commonly named after the angle they produce. Two commonly used pulse types are the 90° excitation pulse, which results in flipping all the available net magnetisation into the transverse plane where it can be measured, and a 180° inversion pulse.

Excitation of the spin system does not last: it decays exponentially and with it, the MRI signal. There are two main relaxation mechanisms, both of which can serve as the basis of MRI contrast. Firstly, spins give off energy to the surrounding environment in the form of heat. The effects of this *spin-lattice relaxation* are governed by the T_1 time constant according to:

$$M_z = M_0(1 - e^{-t/\mathrm{T}_1}), \tag{1.6}$$

where $M_0 = |\mathbf{M}_0|$ is the total net magnetisation available and M_z denotes the z component of the net magnetisation vector $\mathbf{M}$. Additionally, spins exchange energy between themselves, which introduces random variation in their phases: the phase distribution widens and as a result the traverse magnetisation (M_{xy}) decays:

$$M_{xy} = M_0 e^{-t/\mathrm{T}_2}, \tag{1.7}$$

where $\mathrm{T}_2 \leq \mathrm{T}_1$ is a constant that characterises this *spin-spin relaxation*. Equations (1.6) and (1.7) are known as Bloch equations [23]. The dephasing of the excited spins is even quicker if local field inhomogeneities are present. In this case, the spins' resonant (Larmor) frequencies depend on their position and the precession itself introduces additional dephasing. As a result, following a simple 90° excitatory pulse the signal decays according to $\mathrm{T}_2^* < \mathrm{T}_2$ time constant. Depending on the tissue type or pathology, different relaxation mechanisms might provide the required image contrast; careful de-

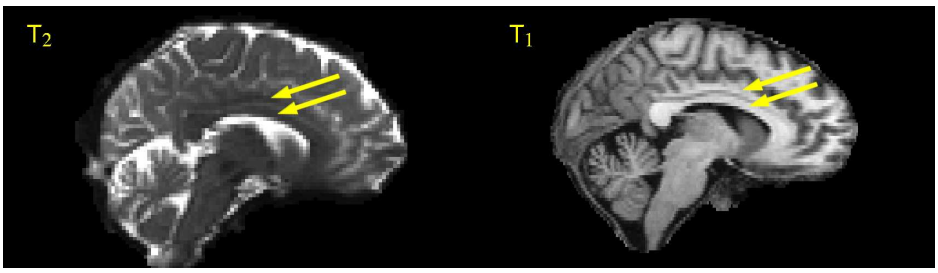

Figure 1.1: T_2- and T_1-weighted volumes from the same subject in a sagittal cross-section. Yellow arrows mark two of the major association and commisural white matter pathways: cingulum bundle (top arrows) and corpus callosum (bottom arrows). Note that the images were not co-acquired (and have different resolution) and thus the slice correspondence is only approximate.

sign of the acquisition pulse sequence can sensitise the resulting signal to either of the basic time constants (see Figure 1.1). Popular sequences include *inversion recovery* for T_1 and *spin echo* for T_2.

The diffusion MRI acquisition is typically based on the spin echo sequence used for T_2-weighting. The basic version of this technique consists of a 90° excitation pulse, followed, after time TE/2, by a 180° refocusing pulse (see Figure 1.2). After the excitation, the spins dephase according to the T_2^* time constant, depending on the (locally inhomogeneous) field strength. The refocusing pulse flips the spin orientation and now the different resonant frequencies serve to reverse the dephasing produced previously. At time TE after the original 90° pulse, a maximum echo signal is formed, subject to (non-reversed) T_2 relaxation (see Figure 1.2). In a spin-echo-based diffusion-weighted sequence the field strength is not uniform between the excitation and inversion pulses. Instead, a small gradient field oriented in a carefully specified direction is added on top of B_0. Since the resonant (Larmor) frequency depends on the strength of the external magnetic field, spins at different positions along the field gradient will rotate with slightly different frequencies. This has no effect on (hypothetical) stationary spins, because they experience the same field strength during dephasing and re-phasing. On the other hand, spins that move *along* the gradient direction during the sequence accumulate a phase difference due to varying resonant frequency at different spatial locations. This phase shift affecting some spins leads to incomplete refocusing and loss, or attenuation, of echo signal. The magnitude of the signal attenuation depends on the number of moving molecules and their displacements: it is proportional to the diffusion during the acquisition sequence. It is worth noting that the diffusion process itself

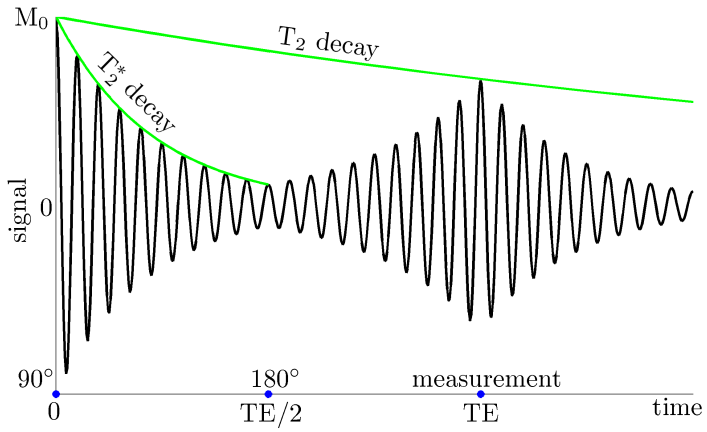

Figure 1.2: Radio frequency pulses and MR signal in a spin echo experiment. After the 90° excitation pulse, the signal decays exponentially according to the T_2^* time constant. Following the 180° refocusing pulse at time TE/2, the position-dependent differences in the Larmor frequency due to local field inhomogeneities act to cancel the acquired phase differences leading to the formation of echo signal at time TE (echo time). Note that the T_2 relaxation is not recovered. Time constants in this schematic illustration are not to scale.

is not affected by the measurement. Each gradient direction sensitises the scanner to a (Fourier transform of) different portion of the diffusion profile, which (given the time between the RF pulses) stays the same. A typical diffusion MRI acquisition consists of at least one T_2-weighted volume (without diffusion weighting) and a number of diffusion weighted volumes (see Figure 1.3) acquired using a set of gradient directions designed to uniformly cover the whole angular space (see for example [62]). This yields diffusion-related signal attenuation in every gradient direction and provides a measure of diffusion anisotropy which is used to look at white matter.

MRI image formation is beyond the scope of this introduction; it is salient to note that a number of steps are needed in order to localise the source of the measured signal. These steps usually include slice selection (where a combination of gradient field and appropriately tuned, narrow bandwidth RF pulse is used to excite only voxels in particular XY plane) followed by phase and frequency encoding, whereby both the resonant (Larmor) frequency and the phase of the precessing spins vary across space and can thus be used for localisation. While the position encoding enables the identification of finite volume elements, its precision is restricted both by the hardware requirements that limit the pulse sequences (waveforms) that can be achieved (due to induction from

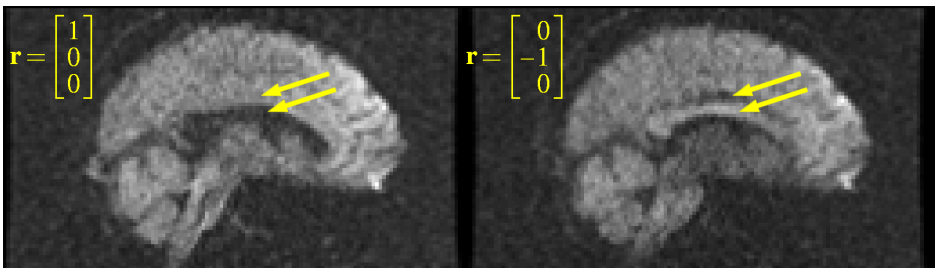

Figure 1.3: Two diffusion-weighted images of the same brain slice acquired with different diffusion-sensitising gradients (orientations given by **r**): gradient orientation in the left plot is perpendicular to the plane of the image, whereas in the right plot the gradient is oriented horizontally (the sagittal cross-section shows the YZ image plane). The axons of the cingulum bundle (top arrows) run horizontally in both plots; we note a marked signal attenuation when a diffusion gradient aligns with their orientation (i.e. in the right plot). Analogously, the fibres of the corpus callosum (bottom arrows) run perpendicularly to this particular slice and thus align with the gradient direction in the left plot, leading to signal attenuation due to water molecule diffusion along the local tract direction. A relatively weaker attenuation can be observed where the orientations of the white matter fibres and the diffusion-sensitising gradients are different.

fast switching gradients) and, fundamentally, by the amount of spins necessary to produce a signal with acceptable signal-to-noise ratio. One important consequence of the limited imaging resolution is the integration of contributions from different intra- and extracellular components – even different tissue types – over the voxel volume. We shall discuss the implications of this fact in Section 1.2. Another feature of the position encoding is that the measured MRI signal corresponds to the 2D Fourier transform of the image rather than the image itself. In the context of MRI acquisition, the Fourier space is often referred to as k-space. Using a simple encoding sequence a series of points (frequency encoding) along a horizontal line in k-space (selected with phase encoding) are collected (see Figure 1.4, left). Imaging a whole brain slice involves measuring from sufficient number of lines in k-space to enable inverse transformation via the Fast Fourier Transform (FFT). Diffusion-weighted imaging is a technique that requires a large number of volumes to be collected (using diffusion-sensitising gradients with different orientations) and is sensitive to subject motion. It therefore benefits from fast imaging techniques, such echo-planar imaging (EPI). Instead of populating k-space line-by-line, EPI measures all required values in one sweep, following a single excitatory pulse (see Figure 1.4, right). For this reason, EPI is often referred to as a

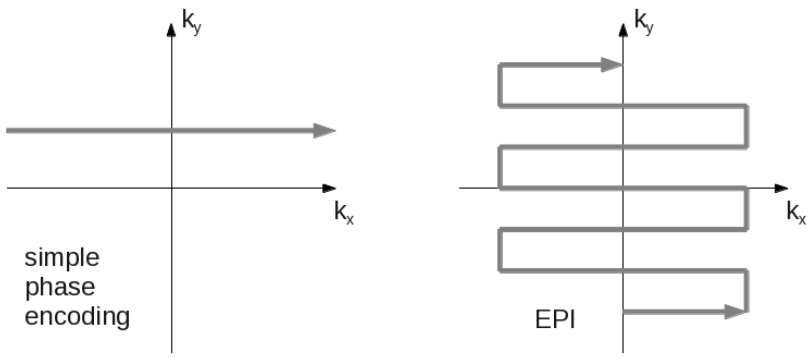

Figure 1.4: Comparison of echo-planar imaging (EPI) and standard phase encoding; plots show k-space trajectories for which values are measured after a single spin echo sequence.

single shot technique.

The measured signal is the Fourier transform of the displacement distribution [2]. There are two main approaches to using diffusion MRI to look into the tissue architecture. Given enough measurements of s it is possible to recover the displacement probability $p_t(\mathbf{x})$ by numerically inverting the Fourier transform (see Section 1.2.3 on page 19). This is in general a hard problem when the signal is noisy. In order to avoid the numerical inversion of the Fourier transform, model-based methods assume a simple parametric form of $p_t(\mathbf{x})$ which can easily be transformed analytically (see Section 1.2 on page 12). In fact, tissue properties of interest can usually be obtained from the resulting signal attenuation formula, without the need to compute the displacement distribution at all.

There are two main sources of image acquisition artefacts in diffusion-weighted MRI: subject motion and the discrepancy between the theoretical and actual magnetic field [8, 63, 115]; both types of artefacts are in some ways aggravated in diffusion MRI with respect to other MRI modalities. Consider, for example, that even small amount of motion can be picked up during this type of acquisition, since diffusion-weighting field gradients sensitise the spin echo sequence to the displacement of excited spins measured in micrometres. Apart from diffusive flow, the position of water molecules can be affected by head and eye motion, as well as pulsation of cerebrospinal fluid and blood. Fortunately, head and other bulk motion is not an issue in (single shot) EPI, since it introduces a uniform phase shift which does not affect the echo time and amplitude. Incoherent motion, on the other hand, introduces additional dephasing of the spins and thus leads to further, unwanted attenuation of the signal. High motion

sensitivity is yet another reason (apart from the number of volumes acquired) for using fast imaging sequences, such as EPI. Additionally, blood pulsation-related distortions are most commonly countered by using cardiac gating, where each measurement is taken at the same phase of the cardiac cycle.

Apart from non-diffusive displacement of spins, diffusion MRI acquisitions suffer from artefacts produced when the actual magnetic field differs from the theoretical one. This can occur for two reasons. In the areas where brain parenchyma borders air-filled spaces, such as sinuses, or bone, the abrupt differences in magnetic susceptibility alter the B_0 field; this effect is more pronounced at higher field strengths. Another source of image-degrading magnetic field alteration are eddy currents: electric currents induced in the wiring of the scanner by the powerful, fast-switching diffusion encoding magnetic field gradients. Diffusion-sensitising gradients are a particularly powerful source of eddy currents because of their high field strength, fast switching and non-negligible duration. The field alterations caused by eddy currents are manifested as distortions of the diffusion-weighted image, such as stretches, shears and translations. Although eddy current-induced distortions affect the entire image, they are typically easiest to spot on the edges of the brain. Due to the fact that distortions differ between consecutive diffusion-weighted volumes, voxels on the border of the brain are sometimes assigned the measurements taken from the outside. This in turn results in extreme, high anisotropy values.

1.2 Modelling diffusion in single voxels

1.2.1 Diffusion tensor

As discussed in Section 1.1.2, water diffusion in the brain is affected by the microstructure of parenchyma, especially for longer diffusion times. At the currently attainable imaging resolution, many different intra- and extracellular compartments with different viscosities, as well as membranes with varying permeabilities, will contribute to alter the measured MRI signal. For this reason dependence of the diffusion profile on the underlying tissue parameters remains intractable. However, we can still approximately treat the entire voxel volume as if it contained a medium characterised by homogeneous viscosity. Using this formalism, proposed by LeBihan [20], the diffusion is approximated as Gaussian (see Section 1.1.1) and quantified by the scalar apparent diffusion coefficient (ADC). As discussed in Section 1.1.1, in some circumstances scalar dif-

fusivity is not appropriate and the tensor description can be used instead. The tensor equivalent of the ADC is the effective diffusion tensor $\mathcal{D}_{\text{eff}}$. In what follows, effective diffusion tensors are used and implied, though for simplicity of notation we shall continue to use the $\mathcal{D}$ symbol. The approximation of highly complex diffusion processes in the brain tissue by simple Gaussian diffusion in a homogeneous, anisotropic medium is a powerful concept; this approach is known as the *diffusion tensor model* [9].

The Gaussian displacement probability distribution $p_t(\mathbf{x})$ given by equation (1.5) is fully determined by its covariance matrix, which in turn is proportional to a diffusion tensor: $\Sigma = 2\mathcal{D}t$. $\mathcal{D}$ is a real-valued, symmetric, positive definite matrix; it provides a complete description of the Gaussian diffusion. In a diffusion MRI experiment, the diffusion time is typically fixed and the measured signal attenuation serves to estimate $\mathcal{D}$. Bloch magnetisation equations (1.6) and (1.7) with diffusion terms are known as Bloch-Torrey equations [112]. Early demonstration of diffusion sensitisation was performed by Stejskal and Tanner [103], who solved Bloch-Torrey equations for the pulse sequence they developed, obtaining:

$$S/S_0 = \exp\left[-\gamma^2 G^2 \delta^2 (\Delta - \delta/3)\text{ADC}\right], \tag{1.8}$$

where ADC is the scalar apparent diffusion coefficient, S/S_0 denotes diffusion-related signal attenuation, γ is the gyromagnetic ratio, G is the strength of the diffusion-sensitising magnetic field gradient, and δ and Δ quantify the duration and timing of the gradient pulses. As the development of acquisition techniques continues with ever more elaborate sequences, the solution does not have a simple and elegant form. For this reason the dependence of signal attenuation on the strengths, shapes and durations of the gradient pulses is usually computed separately and encapsulated using a single *b*-value measured in diffusivity units (original idea due to LeBihan [19]). In the case of non-isotropic diffusion, the MRI signal attenuated by a gradient oriented along $\mathbf{r}$ is given by:

$$S(\mathbf{r}) = S_0 \exp(-b\mathbf{r}^T \mathcal{D}\mathbf{r}), \tag{1.9}$$

where, as usual, $\mathcal{D}$ denotes the effective diffusion tensor. It is worth noting that b depends linearly on diffusion time; this means that the signal attenuation is exponential in time. Unfortunately, it is well known that in the brain the time-dependent attenuation profile is more similar to that of a bi-exponential decay [86, 83], thus suggesting the existence of two pools of water molecules characterised by fast and slow diffusion. Modelling work to date has not provided conclusive evidence of the existence

of such distinct compartments, and if they compared to intra- and extracellular water [18]. Alternative explanations, including more specific compartment types [14] and the presence of barriers in a single-compartment system [104] have also been explored.

With a Gaussian displacement distribution, the mean square displacement profile (similarly to all equidensity contours) is given by an ellipsoid; the local tract direction is thought to be aligned with its longest axis, corresponding to greatest diffusivity or least obstacles to molecular motion. $\mathcal{D}$ is usually decomposed into a diagonal matrix of eigenvalues Λ and a rotation matrix R:

$$\mathcal{D} = R\Lambda R^T, \quad \text{where} \tag{1.10}$$

$$\Lambda = \begin{bmatrix} \lambda_1 & 0 & 0 \\ 0 & \lambda_2 & 0 \\ 0 & 0 & \lambda_3 \end{bmatrix} \quad \text{and} \quad R = [\mathbf{e}_1\mathbf{e}_2\mathbf{e}_3].$$

Columns of R ($\mathbf{e}_i$) define the orientation of the ellipsoid's axes; λ_i are the diffusivities along these axes and mean square displacement along $\mathbf{e}_i$ during the diffusion time τ is equal to $2\lambda_i\tau$. The eigenvalues are usually sorted, so that λ_1, measured in the direction $\mathbf{e}_1$, is the greatest diffusivity and λ_3 is the smallest. A set of Euler angles (θ, ϕ, ψ) is a common alternative for R used to specify the eigenspace. Both R and (θ, ϕ, ψ) define a set of rotations used to transform an ellipsoid aligned with the axes of the current coordinate system (defined by Λ) into an arbitrarily oriented one. While it might seem that substituting a 3×3 R matrix with three values results in loss of information, it is worth stressing that R has 9 coefficients, but only 3 degrees of freedom. This is because it is a rotation matrix and its columns $\mathbf{e}$ form an orthonormal basis. For cylindrical tensors (see below) only 2 values are needed because ψ corresponds to the rotation around the axis of symmetry. Since $\mathcal{D}$ is determined by its 3 eigenvalues and 3 Euler (rotation) angles, 6 gradient directions are, in principle, sufficient to estimate it. In practice, a greater number of directions is usually used in order to alleviate the impact of noise. The diffusion tensor model can then be fitted to the diffusion-attenuated signal using, for example, multiple regression [9]. WM voxels belonging entirely to one fasciculus can be adequately described by a cylindrical or *prolate* tensor with high anisotropy ($\lambda_1 \gg \lambda_2 \approx \lambda_3$, see Figure 1.5), while the crossing fibre regions are characterised by an *oblate* tensor ($\lambda_1 \approx \lambda_2 \gg \lambda_3$) with anisotropy lower than that of the constituent tracts [43]. Isotropic diffusion corresponds to a spherical tensor ($\lambda_1 = \lambda_2 = \lambda_3$, again see Figure 1.5 for comparison); such profile indeed tends to be observed in cerebrospinal

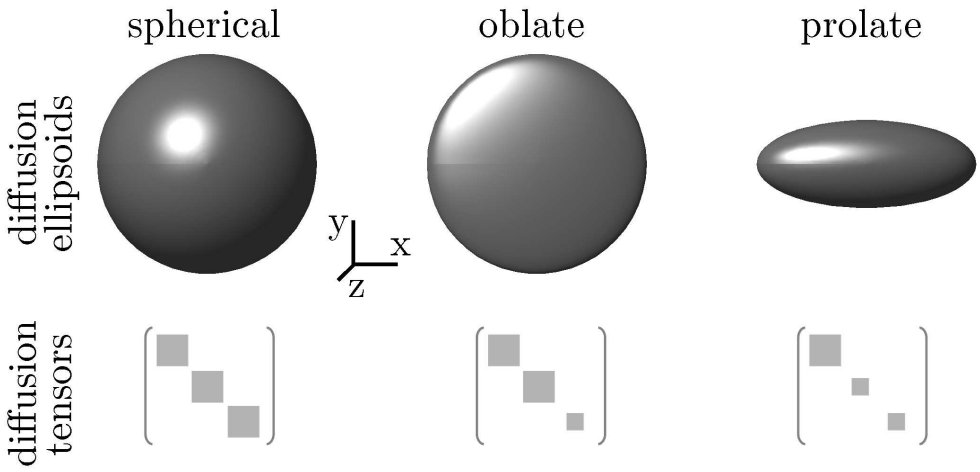

Figure 1.5: Shapes of diffusion ellipsoids typical for isotropic diffusion (spherical, left), diffusion in the area of crossing fibres (oblate, centre) and diffusion in a single white matter fibre (prolate, right). Corresponding diffusion tensors are given below, with squares scaled according to the magnitude of appropriate eigenvalues (though not exactly to scale).

fluid and grey matter.

While the effective diffusion tensor might provide a useful summary description of the properties of a particular tissue type, it has to be remembered that in a typical diffusion MRI experiment the measured signal originates from volume elements (voxels) 1.5-2.5 mm in dimension: a scale comparable to that of many functional structures in the brain. For white matter the Gaussian approximation of the diffusion process is useful when a single, straight axonal bundle is present in a voxel, but not for more complex architectures, such as crossing, bending or fanning fibres [9, 43, 1]. When two or more fasciculi pass through a voxel, for instance, the diffusion tensor model has been shown to yield an averaged estimate of fibre direction rather than any of the true orientations [43]. Not only can a voxel contain crossing white matter fibres from different pathways; other tissue types, such as grey matter or cerebrospinal fluid, can also be present. These tissue type inhomogeneities are usually referred to as isotropic *partial volume effects*, or simply partial voluming. Analysis of the parameters of the Gaussian diffusion profile is made difficult as a result of incorrect estimation of these parameters in voxels where partial voluming from different tissue types contaminates the measured signal. Approximating the diffusion process as Gaussian, the diffusion tensor model simplifies the description of the complexity not only on the level of mi-

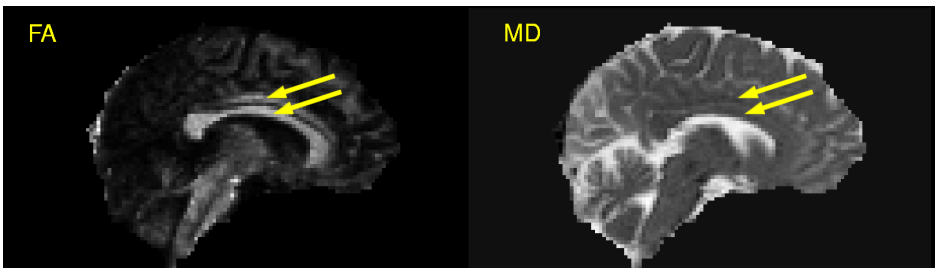

Figure 1.6: FA and MD images of the same brain slice. Note high anisotropy (quantified by FA) and relatively low diffusivity of the marked white matter pathways: cingulum bundle (top arrows) and corpus callosum (bottom arrows).

crostructure, but also fibre architecture and tissue type.

Nevertheless, the diffusion tensor model is ubiquitously used to study healthy and diseased white matter. While it is possible to consider individual eigenvalues of the diffusion tensor, such as radial ($\frac{\lambda_2+\lambda_3}{2}$) and axial ($\lambda_1$) diffusivities (see discussion in Section 4.1.2), it is more common to examine summary statistics of tensor shape that quantify the overall amount of diffusion and its anisotropy. The two most prominent tensor-derived metrics are mean diffusivity (MD) and fractional anisotropy (FA), presented in Figure 1.6 and given by:

$$\mathrm{MD} = \frac{1}{3}\mathrm{Trace}(\mathcal{D}) = \frac{\lambda_1+\lambda_2+\lambda_3}{3}, \tag{1.11}$$

$$\mathrm{FA} = \sqrt{\frac{3}{2}}\left[\frac{\sum_{i=1}^{3}(\lambda_i-\mathrm{MD})^2}{\sum_{i=1}^{3}\lambda_i^2}\right]^{\frac{1}{2}}. \tag{1.12}$$

One aspect of the diffusion tensor model where rapid progress and improvement has been made is in the estimation of fibre orientations for fibre tracking and segmentation (see Section 1.3.1). The first important development was to quantify the uncertainty of the orientation estimates. For the diffusion tensor model, Jones [61] proposed the use of bootstrap methods to compute confidence intervals on the fibre orientations and uncertainty cones to visualise them. Alternative methods, such as the ball-and-stick [16], use Markov chain Monte Carlo (MCMC) sampling techniques to estimate the probability distribution function (*pdf*) over the fibre orientation. In this model, attenuated signal is expressed as a sum of two diffusion tensor terms: isotropic “ball” and infinitely anisotropic “stick” (see signal attenuation equation in Table 1.1). The anisotropic component is described by an axially symmetric tensor with only one non-zero eignenvalue, indicating the local fibre direction. Importantly in the context of our work, ball-and-stick components do not correspond to white mat-

ter or other tissue within a voxel. The anisotropic term, in particular, has no physical or biological meaning because of zero diffusivity in the transverse plane (λ_2, λ_3). Rather the model seeks to estimate the distribution over the fibre angles and the additional parameters simply control the amount of anisotropy and overall diffusivity to enable a better signal fit. The ball-and-stick model has been hugely influential due to freely available software implementation (`bedpost`) and integration with a popular fibre tracking algorithm (`probtrack`, both parts of the FSL toolkit [100, 121, 60], `http://www.fmrib.ox.ac.uk/fsl`). Another model by Friman et al. [45] uses a single, cylindrical tensor (see Table 1.1). Here, Markov chain sampling for θ and ϕ is replaced with uniform sampling on a sphere. Since the focus of attention is on fibre angles, point estimates are used instead of sampling for other "nuisance parameters".

The methods described so far are limited in their expressive power in that they cannot correctly describe the partial voluming, either from additional white matter bundles or from the isotropic tissue types, cerebrospinal fluid and grey matter. In order to develop such a description, let us consider a richer class of models, with more than one tensor term.

1.2.2 Multi-tensor methods

As we have seen above in the case of the ball-and-stick model, it is often useful to use more than one tensor to describe the diffusion-induced MRI signal attenuation. Let us now consider the general class of such multi-tensor models, in particular how they can be used to handle partial voluming. We start by dividing each voxel into K Gaussian diffusion compartments, potentially containing different tissue types, with volume fractions $\{v_k\}$ and tensors $\{\mathcal{D}_k\}$. Assuming no exchange between these compartments, a displacement distribution in the form of a mixture of Gaussians can be used:

$$p_t(\mathbf{x}) = \sum_{k=0}^{K} v_k G(\mathbf{x}|\Sigma_k = 2\mathcal{D}_k t) \quad \text{with} \quad \sum_{k=0}^{K} v_k = 1, \tag{1.13}$$

which yields attenuated signal given by [2]:

$$S(\mathbf{r}) = S_0 \sum_{k=0}^{K} v_k \exp(-b\mathbf{r}^T \mathcal{D}_k \mathbf{r}), \tag{1.14}$$

where the unattenuated signal, S_0, is estimated jointly for all compartments. In general, multi-tensor modelling greatly increases the number of parameters that need to be estimated, making it more computationally expensive. More importantly, it can

yield ambiguous, non-unique solutions [44], where different parameter settings produce identical signal attenuation profiles and are therefore indistinguishable based on the data alone (see discussion in Section 2.1.2). Nevertheless, it is employed by a number of multi-tensor methods in order to accommodate more than one (straight) fibre within a voxel, i.e. anisotropic partial voluming. A number of constraints and simplifications is usually needed.

An extension of the ball-and-stick model by Hosey et al. [55, 56], for example, tackles the estimation issues by reducing the number of parameters such that $\mathcal{D}_1 = \mathcal{D}_2$ are cylindrically symmetric tensors (see Table 1.1). Additional, arbitrary constraints are imposed on the volume fractions (v_1, v_2) and on the difference between eigenvalues $(d_\Delta = \lambda_1 - \lambda_{2,3})$ in order to stabilise the MCMC sampling. A Bayes factor is then used to compare one- and two-fibre models to avoid overfitting. Although both tensors have physical meaning (i.e. all non-zero eigenvalues) unlike in the original ball-and-stick, the goal of this work is the retrieval of the white matter fibre orientations, rather than correct description of partial volumes. A more recent version of ball-and-stick by the same authors [15] also facilitates crossing fibres modelling by using more than one anisotropic component (all described by an identical, infinitely anisotropic tensor; see Table 1.1). The number of such "sticks" is controlled using Automatic Relevance Determination: a technique that uses parametrised relevance priors on volume fractions of additional fibres. Imposing a threshold on this parameter results in the rejection of redundant components and a model of complexity adjusted to the underlying data. Using available acquisition parameters (60 gradient directions with a b-value of 3000s/mm^2), the model's complexity is limited to a two-fibre case and angular resolution to crossings at 30°or more [15].

While the multi-tensor modelling to date has been focused predominantly on the estimation of white matter fibre orientations, the possibility of using this framework to account for isotropic partial voluming has also been explored. Notably, a two-tensor attenuation equation has been employed by Pasternak et al. [90] in their free water elimination approach (see Table 1.1). The objective of their work is to rectify the estimation of the diffusion tensor in the presence of cerebrospinal fluid, on the borders of ventricles and sulci as well as in cerebral œdema. The effect of such "contamination" is an apparent, spurious increase in overall diffusivity accompanied by a decrease in diffusion anisotropy. The authors employ a variational regularisation framework (see Section 5.2) in order to ensure spatial smoothness of the estimates in the neighbouring voxels and stabilise the estimation. In addition, hard constraints are placed on the

Model	Signal attenuation equation
Diffusion tensor, [9]	$S(\mathbf{r}) = S_0 A_{\lambda_1,\lambda_2,\lambda_3}$
Friman, [45]	$S(\mathbf{r}) = S_0 A_{d_\perp + d_\Delta, d_\perp, d_\perp}$
Ball-and-stick:	
(a) basic, [16]	$S(\mathbf{r}) = S_0 \left((1-f)A_d + f A_{d,0,0}\right)$
(b) extended, [15]	$S(\mathbf{r}) = S_0 \left[(1-f_1-f_2)A_d + f_1 A_{d,0,0} + f_2 A_{d,0,0}\right]$
Hosey, [55]	$S(\mathbf{r}) = S_0 \left[(1-f_1-f_2)A_d + f_1 A_{d_\parallel, d_\perp, d_\perp} + f_2 A_{d_\parallel, d_\perp, d_\perp}\right]$
Free water elimination, [90]	$S(\mathbf{r}) = S_0 \left[(1-f)A_d + f A_{d_\parallel, d_\perp, d_\perp}\right]$

Table 1.1: Selected models of water diffusion in the brain and the corresponding signal attenuation equations. $A_{\lambda_1,\lambda_2,\lambda_3}$ are exponential attenuation terms in the form $A_{\lambda_1,\lambda_2,\lambda_3} = \exp(-b\mathbf{r}^T \mathcal{D}\mathbf{r})$, where $(\lambda_1, \lambda_2, \lambda_3)$ are the eigenvalues of $\mathcal{D}$.

allowed white matter diffusivity values (implemented as band limits on the non-water volume fraction) and point estimates are used for the values of the diffusivity of cerebrospinal fluid and the non-diffusion-weighted signal. The fitting itself is achieved by minimising a hand-crafted variational functional. Grey matter is not directly modelled and in voxels where partial voluming from this tissue type occurs we still expect to see spuriously low anisotropy in comparison with that of pure white matter. Additionally, introducing hard constraints and arbitrary smoothing mechanism, even across different neural structures, might bias the estimation of the volume fractions and other parameters. We believe, however, that free water elimination presents a step in the right direction by directly modelling the cerebrospinal fluid compartment and attempting to estimate its true volume.

1.2.3 Model-free and non-Gaussian methods

We have briefly reviewed modelling work based on the Gaussian diffusion approximation, which uses an explicit, computationally convenient model of the displacement distribution for which it is easy to obtain the formula for signal attenuation. An alternative approach is that of model-free estimation of the diffusion profile relying on numerical inversion of Fourier transform to directly estimate the displacement distribution $p_t(\mathbf{x})$. This inversion usually requires complex acquisition sequences, involving multiple b-values. This is why the practically useful methods, such as q-ball [116], PAS-

MRI [58], focus on describing the angular dependency of $p_t(\mathbf{x})$, neglecting the radial part. Spherical harmonic decomposition of the attenuation profile has been proposed to identify voxels containing multiple fibres and filter out artifacts [2, 44]. The same technique can be used for the spherical deconvolution approach [114, 113, 66, 65, 67]. Here, the measured signal is modelled as a convolution of a single fibre response function and a fibre orientation density function. No underlying model of diffusion is used and fibre response function (identical for all fibres) is estimated from the data. It is worth pointing out that orientation density function is not enough to resolve complex fibre structures. This is because crossing tracts, local curvature and noise might result in a function that is difficult to interpret.

The advantage of model-free methods is the independence of any assumptions regarding the tissue type composition, number of fibres in a voxel or how a single tract affects diffusivity. This allows direct modelling of the angular structure of the measured signal, not biased by such assumptions, but linking the approximated orientation density functions to the actual white matter structure remains difficult. More fundamentally, a lack of an explicit description of partial voluming means that no information about the white matter volume or diffusivity can be obtained using these methods.

More than the angular information can be extracted using elaborate acquisition protocols and low-level, non-Gaussian diffusion modelling. A notable framework for modelling white matter structure at a very fine level is CHARMED [6, 5]. In an effort to account for bi-exponential signal decay, signal attenuation is described by combination of two different type of compartments. A hindered, Gaussian diffusion compartment is designed to model the extra-axonal space, whereas a restricted, non-Gaussian diffusion compartment corresponds to water within axons. More than one restricted compartment can be used to facilitate the crossing fibres description. Initially, the method required as much as 16 different b-values of up to 44000s/mm^2 and 18 hours of acquisition time [6], which made it unsuitable for use with human subjects; later, a more efficient acquisition scheme limited to 10 slices and a resolution of $3\times3\times3$mm, was developed [5], cutting the imaging time to 17 minutes. The authors admit that the hindered diffusion component might be influenced by contributions from glia and astrocytes and that volume fractions of the compartments do not necessarily reflect true extra- and intracellular volume fractions [6]. Non-Gaussian diffusion modelling has also been used by Alexander et al [3] to estimate the distribution of axonal diameters. These contributions, however interesting, are of little importance to our work, because they examine brain tissue at much smaller scales; it would be difficult to obtain tissue

composition of voxels from their results.

1.3 Combining results from single voxels

1.3.1 Fibre tracking

Another reason for combining information across many voxels is to compare the tissue properties averaged over structures of interest, such as whole fasciculi. Since the principal diffusion direction in general aligns well with the orientation of neural fibre bundles, following this direction through the brain can be expected to reveal the course of white matter pathways. The majority of early fibre tracking algorithms [37, 80, 10] were built on a concept of streamlining, that is generating a piecewise linear approximation to an actual tract (a streamline). First of all, a *seed point* was located manually within a fasciculus of interest, based on local landmarks. Angular data (typically from the diffusion tensor model) was then interpolated to create a continuous orientation field and standard integration methods, such as Euler's or Runge-Kutta methods, were used to compute the evolution from this starting point, much as a trajectory of a particle in a physical vector field. The dependence of early tracking algorithms on diffusion models that are inaccurate for voxels with partial volume effects (especially crossing fibres) often resulted in false angle estimates and spurious trajectories as well as premature tract truncation due to incorrectly low FA. A more important flaw stems from the fact that the streamline methods are deterministic, in the sense that that the same seed is guaranteed to yield the same streamline as long as precision parameters (e.g. step size) stay the same. As a consequence, the streamline produced using a particular seed is a "best guess" without any measure of uncertainty attached to it. Additionally, even assuming that the output streamline approximates the core of the fasciculus of interest well, it contains no information about its physical extent (since streamlines have no thickness).

Probabilistic tractography methods differ from deterministic ones in that they supply probabilities of connection from the seed point to a given voxel. They achieve this by following the direction of greatest diffusivity stochastically, based on the local, estimated orientation uncertainty, so that the same starting point can yield different streamlines. ProbTrack [16] was the first widely used probabilistic tracking method. It uses fibre angle estimates computed using ball-and-stick (see pages 16 and 18) to generate probabilistic streamlines. The direction of the next step is drawn at ran-

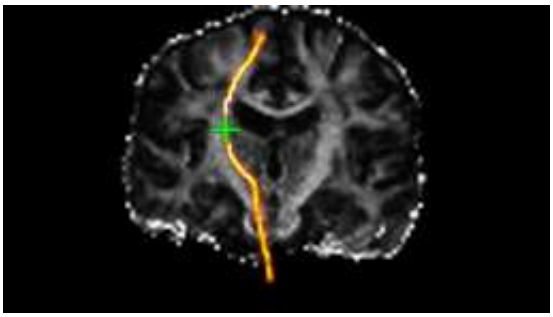

Figure 1.7: Coronal FA slice featuring right corticospinal tract segmented with ProbTrack. Colours from bright yellow through to deep red encode the probability of connection from the seed point (cross). The seed point itself has been selected using the neighbourhood tractography approach described below.

dom from the sample set accumulated by MCMC. Probabilistic interpolation is used to draw the voxel the samples are sourced from at random, with probability proportional to the distance from the current position. Tracking is repeated a number of times (typically 5000) and a fraction of streamlines that reach a particular voxel approximates the probability of connection from the seed point. The resulting probability field can be used for visualisation (see Figure 1.7) or as weighting factors to calculate tract-specific FA, sometimes with misleading results (see discussion in Section 1.4). Other examples of probabilistic tracking methods include the algorithm proposed by by Friman et al [46, 45] based on their diffusion model described above, probabilistic index of connectivity (PICo, see [88]), which uses PAS [58] and Gibbs tractography [70].

Apart from segmenting white matter pathways of interest for further analysis, it has recently been proposed that tractography can be used to better visualise the anatomy of white matter, on a scale smaller than that of the acquisition voxel. Calamante et al [28, 27, 29] have demonstrated how such super-resolution can be achieved by track-density mapping. The authors start by performing whole-brain probabilistic tractography (i.e. seeding in every voxel) with an adequately small step size (0.1mm). The generated streamlines then serve, subject to a length threshold, to create a track-density map by counting their streamline points on a fine grid: in this way authors achieve up to 0.125mm isotropic resolution from the original 2.3mm isotropic acquisition voxels [28]. In a similar manner, streamlines obtained with targeted, rather than whole-brain tractography can be used to highlight and examine particular white matter structure. It has to be noted that this approach does not estimate the volume of the white

matter pathways directly, but rather provides an entirely new quantity, track density, whose properties need to be thoroughly investigated. In particular, it is not clear how track density can be used to recover other tissue parameters derived from the shape of diffusion profile (such as the amount of anisotropy), rather than simply from the streamlines themselves (basically fibre orientation). Nevertheless, the method presents an interesting approach to using the continuity information contained in the diffusion MRI data (in this case, continuity of fibre orientation exploited by the tractography).

We have already mentioned that the areas most difficult to track through are the voxels in which the fibres cross. This difficulty is usually attributed to the use of voxel-level models inappropriate for crossing fibres (such as the diffusion tensor). More fundamentally though, it might be impossible to disambiguate fasciculi locally, without looking at the global tract structure. Jbabdi et al [59] proposed to constrain local diffusion models (ball-and-stick) using the global connectivity information defined by specifying pairs of connected cortical regions. A space of streamlines running between these areas is sampled using MCMC; the streamlines, in turn, determine the local fibre orientation estimates in the voxels they pass through, thus effectively linking global connectivity and local diffusivity information.

Apart from the crossing fibre issue, the quality of segmentation delivered by tractography crucially depends on the correct choice of a seed point. While early tracking methods were usually initiated from a seed point placed manually in the image, more modern approaches define the starting point in standard space and then project it back to the subject space. This helps avoid bias when performing group studies — all seed points are produced from the same standard space seed via projections that optimise the fit of the registered dataset to the template. Unfortunately, due to individual differences in the brain's topography (greatly amplified in ageing and some forms of pathology, e.g. tumors), this simple approach is less than optimal and occasionally fails to find the desired fasciculi altogether by placing the seed points outside white matter, e.g. in the ventricles. More subtly, the segmented pathways might follow the course different than that predicted by the anatomical knowledge or terminate prematurely.

One way to address the issues of tracking through crossing fibres' areas and inaccurate seed point location when registering from the standard space, while at the same time avoiding the manual placement has been proposed by Heiervang et al [52]. The authors constrain the tractography using a set of masks (regions-of-interest or ROIs) delineated by hand in the standard space, separately for each tract. Fibre tracking is started from *seed masks* and required to reach *target masks*. At the same time, stream-

lines that reach *termination masks* are stopped and those which enter *removal masks* are discarded. The same set of masks is used when segmenting a given pathway in all subjects. While the authors were able to produce better test-retest coefficients of variation for tract-averaged FA than those found by Ciccarelli et al [32] in the case of landmark-guided manual seed placement in subject space, their approach offers no measure of acceptability for particular reconstructions.

Neighbourhood tractography [33, 35, 76, 36] has been developed to aid reproducible, automated segmentation of the brain's neural pathways by entirely eliminating the bias introduced by manual seed or ROI placement. The algorithm starts from the reference seed point projected from standard space. Tractography is initiated from all voxels within a $7\times7\times7$ neighbourhood of this seed point, subject to minimal FA. The pathways segmented by starting probabilistic tractography from each of these voxels are processed to extract median streamlines and finally a cubic B-spline representation. Splines of this type are completely parametrised by the positions of their knots, which become the basis of further processing. A set of up to 343 *candidate tracts* produced in this way are transformed to standard space in order to be compared against a *reference tract*, which represents the desired pathway shape. The *reference tract* itself is typically constructed from a white matter atlas directly in standard space and also represented by the B-spline knots [76]. A tract similarity model (based on the similarity cosines between the inter-knot vectors for candidate and reference tracts) is then used to estimate, for each candidate tract, the probability that it is the best match to the reference in terms of length and shape. Based on this probability one of the candidate voxels is selected as the final seed, thus concluding the *matching phase*. In the following *tracking phase*, standard tractography is performed once again, starting from the chosen seed, to produce final pathway segmentation. The parameters of the matching model needed to be fitted separately in the early versions of the method, which required additional training data; more recently, the authors have developed an unsupervised approach, which employs the expectation-maximisation (EM) algorithm to estimate the relevant probabilities and the model's parameters, iteratively, at the same time [36].

1.3.2 Comparing white matter between individuals

Group studies usually involve comparison of one or more of quantities between a number of individuals (perhaps grouped into two cohorts), which poses two basic ques-

tions: which quantities to investigate and how to compare them. Possible markers of interest are discussed in some detail in Chapter 4; below we use FA as an example quantity of interest. Choosing a comparison method requires finding balance between many factors.

The most crude way of examining group differences is by looking at whole-brain histograms of FA or other index of interest. The usefulness of this method is restricted, as all spatial information is discarded; in fact the basic version is not even white matter specific. Differences found with voxel-based morphometry (VBM), on the other hand, can be spatially localised down to the voxel level [4, 50]. VBM is a method originally devised to study changes in grey matter density between 2 groups. It facilitates voxel-wise comparison by using nonlinear registration of all images to the same space and smoothing designed to alleviate the effects of noise and shifts caused by differences in the anatomy of each person. As a whole-brain technique, VBM doesn't require prior specification of an ROI and enables an exploratory approach; it is fully automated and easy to apply. Since perfect alignment cannot be expected with any registration, however, the results of VBM have to be examined with caution. This is because any detected group differences (e.g. pointing to a drop in white matter coherence) can be due to residual misalignment and partial voluming. There is no principled way of choosing the size of the smoothing filter, either, and this choice can strongly influence the final conclusions [64].

Pros and cons of ROI based approaches are somewhat complementary to those of VBM: they allow hypothesis-driven, but not exploratory investigation. Manual ROI placement is the earliest example; it can be highly non-reproducible, biased and is certainly time consuming, but helps avoid misalignment and partial voluming if ROIs are only placed inside major, thick tracts. Automatic, reproducible segmentation of meaningful ROIs is possible with tractography. Tract-averaged FA or other markers can be computed using the output of deterministic or probabilistic algorithms, as discussed in Section 1.3.1. This requires that fasciculi of interest can be segmented reliably and is thus not applicable for minor pathways which are difficult to track. Partial volume effects limit the confidence in the results, even when probability weighting is used to calculate tract averages. This is essentially because the underlying forward model of diffusion is still inaccurate when it comes to partial volume effects. While probability of connection to the seed provides a means of voxel selection, or weighting, corrupted marker values remain an issue.

Tract-based spatial statistics (TBSS) [99] is intended to combine the exploratory

nature of VBM and white matter specificity of tractography-based methods. The algorithm starts with affine registration of the diffusion-weighted to their respective T_2-weighted volumes, followed by a non-linear, intermediate degrees of freedom registration to the FA map of one representative subject chosen to require the least warping. Registered FA volumes are then averaged; the resulting group FA volumes undergoes thinning (by finding tract perpendiculars and locally maximal FA along them) and thresholding (only FA greater than 0.2 or 0.3 is kept) to create an FA skeleton. Each subject's FA map is then projected onto the skeleton by searching for maximal FA along the perpendiculars. Once these stages are complete, it is possible to perform voxel-wise statistics as all values are now on the same FA skeleton. It is also possible to project on the skeleton and examine other markers of interest. By using FA skeleton, TBSS aims to only examine the pure white matter voxels from the core of each pathway and thus to circumvent the partial voluming issues.

When performing voxel-wise analysis, for example with VBM or TBSS, accidental findings from isolated, single voxels are meaningless and likely due to chance. Rigorous multiple comparison correction is essential in this case. On the other hand, such results become convincing and interpretable when reproducible clusters of voxels with similar patterns of change emerge. TBSS now supports automatic discovery of such clusters, although they need to be labelled by eye, which might impact on the reproducibility, not to mention associated cost and time. TBSS thus relies on the experimenter to decide which pathways are affected. On the other hand, results from the whole pathways segmented with tractography are easier to interpret because they directly highlight the connections which are particularly strongly affected, for example by ageing. In this case identifying these frail links is crucial for understanding how neuronal changes affect cognitive ability. Ultimately, the optimal scale of investigation depends on the spatial patterns of change in the brain tissue: the better matched the two scales are, the easier it is to detect subtle trends and differences (see discussion in Section 6.3).

1.4 Outstanding issues

In this chapter we have presented a necessarily broad introduction into the process of water diffusion in brain tissue and the rudiments of its measurement with MRI. We then described modelling approaches at different spatial scales aimed at obtaining and analysing useful tissue-characterising parameters from diffusion MRI datasets.

Throughout this introduction, we have seen that partial volume effects, where more than one tissue type is present in a voxel, corrupt parameter estimation and analysis. This important issue has only partially been addressed by current methods.

As far as modelling water diffusion in single voxels is concerned, the focus of the majority of the methods we described (Section 1.2) is firmly on the angular information and its use for tracking rather than on correct diffusivity and tract volume estimation. As a consequence, current local models of diffusion either do not describe partial volume effects at all (the diffusion tensor [9], Friman [45], q-space methods), or do it in a highly simplified or incorrect way (Hosey [55, 56], ball-and-stick [16, 15]). Diffusion coefficients and 'volume fractions' in these models are treated as parameters that improve fit to the signal, but their actual values have so far been of little interest. Free water elimination [90] is a notable exception; it uses a realistic diffusion model to estimate and 'filter out' the contribution to the signal from the cerebrospinal fluid ('free water') compartment. Grey matter, however, remains beyond the scope of this method at the moment. CHARMED [6, 5] comes closest to describing the actual white matter architecture, but it has been developed to investigate intra- and extracellular contributions, rather than partial voluming. As a result, the volume fractions in this model do not correspond to particular tissue types.

Looking at a higher level, white matter pathways can be segmented with tractography. Unfortunately, this approach does not address the problem of finding the pathway volume in the presence of partial voluming – it merely identifies the voxels belonging to a particular tract. Probabilistic methods such as ProbTrack [16, 15] or the fibre tracking algorithm proposed by Friman et al [46, 45] output a set of streamlines radiating from a chosen seed point. These streamlines then yield probabilities of connection to the seed, which can be seen as a quantification of tract location uncertainty. This probability field is often used for tract visualisation (perhaps using thresholding), but this introduces ambiguity as tract thickness is not estimated (contrary to what might appear to the viewer). An additional flaw of this approach is that the apparent confidence in the estimated location is disproportionally high around the seed (with a narrow "bottleneck" at the seed voxel) and low at the extremities (highly diffuse profile due to accumulation of uncertainty). The global connectivity estimation method by Jbabdi et al. [59] promises to address some of the issues, but does not look at the tract thickness explicitly and directly. The recent tract density approach [28, 27, 29] offers super-resolved maps that hint at the real spatial extent of the white matter pathways. Tract density, however, is not a measure of volume and could be replaced by the fraction of

a voxel taken up by white matter; in Chapter 2 we develop a framework that directly models this quantity and estimates its uncertainty.

When it comes to the assessment of the structural coherence of white matter fibres, most group studies (Section 1.3.2) examine diffusion tensor based markers (FA, MD and sometimes tensor eigenvalues). We have discussed the impact of partial voluming on this model in Section 1.2.1. FA, for example, has been shown to decrease in voxels with partial volume effects [1]. A recent study [97] also shows that tracts look thicker on FA maps in high resolution (0.71mm) and thinner when using data averaged to simulate low resolution (3.5mm). This suggests the need to compute 'true' FA and other markers. The issues of white matter volume and local diffusivity estimation are coupled, as computation of fibre-induced anisotropy requires the disambiguation of the partial volumes and finding the volumes requires the knowledge of the shapes of the diffusion profiles of the constituent components. The modelling approach we present in Chapter 2 comprises a realistic diffusion model that describes partial volume effects and joint estimation of the diffusion parameters and volume fractions.

Chapter 2

Modelling framework

Chapter 1 presented a brief introduction to diffusion MRI. The focus of this presentation was on voxels where more than one major tissue type is present, a situation we refer to as *partial voluming*. Such voxels are abundant in the brain, yet to date no direct and complete method allowing the estimation of volume fractions of different tissue types and their diffusion characteristics has been developed.

In this chapter, we develop a three-tensor modelling framework, a tissue dependent diffusion model, that explicitly describes the diffusion profiles of the partial volume voxels, with a view to estimating the fraction of each voxel's volume occupied by white matter and the diffusivity parameters of this compartment. As discussed in Section 1.2.1, the original diffusion tensor model is not sufficient in this case: the eigenvalues of the tensor do not correspond to the properties of any of the constituent tissues, but rather describe a mixture as a whole. We then present the estimation procedure for the tissue dependent diffusion model we propose, based on a Metropolis-Hastings MCMC sampler. The convergence properties of this sampler, as well as the plausibility and reliability of the results are tested for different partial voluming scenarios.

2.1 Forward model of diffusion

2.1.1 Partial voluming and the three tensor model

Let us start by partitioning a partial volume voxel into small sub-volumes δv. If the size of such sub-voxels is sufficiently small, most of them will contain only one tissue type and in this case the diffusion tensor will be a reasonable model. Denoting the T_2-weighted signal by S_0 and the gradient directions by $\mathbf{r}_i$, the diffusion-attenuated signal,

analogously to (1.9), is given by:

$$S_i(\delta v) = S_0\,\delta v\,\exp\left(-b\mathbf{r}_i^T\,\mathcal{D}\mathbf{r}_i\right) \quad \text{for} \quad i = 1\ldots n, \tag{2.1}$$

where $\mathcal{D}$ is the diffusion tensor, b quantifies the amount of diffusion-weighting and n is the number of gradient directions used. In order to obtain the formula for the signal measured from the whole voxel, we need to sum (integrate) the contributions from all the small volume elements (which might contain different tissue types):

$$S_i(\text{voxel}) = \sum_{\delta v \in \text{voxel}} S_i(\delta v)$$

Let us now group together the terms describing each of the three tissues. Let us also assume that the parameters (S_0 and $\mathcal{D}$) describing each of the tissue types are locally (i.e. within one voxel) constant. Further, we assume the exchange between the compartments to be negligible. The forward diffusion model then becomes a three-tensor equation:

$$\begin{aligned} S_i = \quad & S_{\text{CSF}} v_{\text{CSF}} e^{-b\mathbf{r}_i^T\,\mathcal{D}_{\text{CSF}}\mathbf{r}_i} \\ & + S_{\text{GM}} v_{\text{GM}} e^{-b\mathbf{r}_i^T\,\mathcal{D}_{\text{GM}}\mathbf{r}_i} \\ & + S_{\text{WM}} v_{\text{WM}} e^{-b\mathbf{r}_i^T\,\mathcal{D}_{\text{WM}}\mathbf{r}_i} \quad \text{for} \quad i = 1\ldots n \end{aligned} \tag{2.2}$$

For the T_2-weighted volume ($b = 0$), this reduces to:

$$S_0 = S_{\text{CSF}} v_{\text{CSF}} + S_{\text{GM}} v_{\text{GM}} + S_{\text{WM}} v_{\text{WM}} \tag{2.3}$$

The number of parameters in (2.2) and (2.3) above is unnecessarily large: the use of full tensors is redundant when we want to describe the properties of a particular known tissue type. In the isotropic cases, for cerebrospinal fluid and grey matter, it makes sense to use a spherical tensor: $\mathcal{D} = d\,I$, where d is a scalar diffusivity constant and I is the identity matrix. This reduces the complexity of the exponent, which no longer depends on the diffusion gradient direction:

$$\begin{aligned} &\mathbf{r}_i^T\,\mathcal{D}_{\text{CSF}}\mathbf{r}_i = d_{\text{CSF}}\mathbf{r}_i^T\,I\,\mathbf{r}_i = d_{\text{CSF}} \quad \text{and} \\ &\mathbf{r}_i^T\,\mathcal{D}_{\text{GM}}\mathbf{r}_i = d_{\text{GM}} \end{aligned}$$

White matter is conveniently described by a cylindrical tensor: $\mathcal{D} = \mathcal{R}\Lambda\mathcal{R}^T$, where Λ is a diagonal matrix of tensor eigenvalues: $(d_\perp + d_\Delta, d_\perp, d_\perp)$ and $\mathcal{R}(\theta,\phi)$[1] is a matrix rotating Λ to align with the fibre orientation. Expressing $\mathcal{R}$ in terms of the fibre

[1] ϕ, θ and ψ are Euler's angles. ψ rotation has been omitted because of the cylindrical symmetry of $\mathcal{D}_{\text{WM}}$.

orientation angles θ and ϕ, expanding the matrix product and simplifying leads to

$$\mathbf{r}_i^T \mathcal{R}\Lambda\mathcal{R}^T \mathbf{r}_i = d_\perp + d_\Delta \cos^2\gamma_i,$$

where γ_i is the angle between the diffusion gradient direction $\mathbf{r}_i$ and the fibre orientation given by θ and ϕ (equivalently, $\cos\gamma_i = \mathbf{r}_i^T \mathbf{e}_i$). Further reduction in the number of parameters can be achieved by using the volume of the acquisition voxel as a unit of volume, irrespective of the image resolution, leading to:

$$v_{\mathrm{CSF}} + v_{\mathrm{GM}} + v_{\mathrm{WM}} = 1 \tag{2.4}$$

In order to automatically enforce this constraint, we re-parametrise the model using two volume variables, v_1 and v_2, defined as:

$$\begin{cases} v_1 = v_{\mathrm{CSF}} \\ v_2 = \frac{v_{\mathrm{GM}}}{v_{\mathrm{GM}}+v_{\mathrm{WM}}} \end{cases} \quad \text{or} \quad \begin{cases} v_{\mathrm{CSF}} = v_1 \\ v_{\mathrm{GM}} = (1-v_1)v_2 \\ v_{\mathrm{WM}} = (1-v_1)(1-v_2) \end{cases} \tag{2.5}$$

The full forward model we propose for the attenuated and non-attenuated MR signal, the tissue dependent diffusion model, is given by:

$$\begin{aligned} S_i = \quad & S_{\mathrm{CSF}} v_1 e^{-bd_{\mathrm{CSF}}} + (1-v_1)\left[S_{\mathrm{GM}} v_2 e^{-bd_{\mathrm{GM}}} + S_{\mathrm{WM}}(1-v_2) e^{-bd_\perp - bd_\Delta \cos^2\gamma_i}\right] \\ & \text{for} \quad i = 1 \ldots n \quad \text{and} \\ S_0 = \quad & S_{\mathrm{CSF}} v_1 + (1-v_1)\left[S_{\mathrm{GM}} v_2 + S_{\mathrm{WM}}(1-v_2)\right] \end{aligned} \tag{2.6}$$

It is worth stressing that in our work the three terms in (2.6) relate to actual physically separate compartments of the voxel. The volume fractions and tensors used are therefore meaningful quantities which can serve further analysis. Additional anisotropic terms could, in principle, be used to account for more than one tract within a voxel (see discussion in Chapter 6).

It might seem that a model with fewer components could suffice for the task at hand. Since the two-tissue partial volumes should be more prevalent than voxels comprising all three tissues, one might be tempted to use a two-compartment, two-tensor model with an isotropic compartment describing either the grey matter or the cerebrospinal fluid, whichever is present. At the same time, the white matter term with low anisotropy could fit the grey matter contribution if necessary. Unfortunately, it seems that such a set-up could introduce additional, unnecessary mixing issues during the estimation, as one or both terms of such a two-component model would need to jump between the energy minima corresponding to the different tissues it can claim

responsibility for. This would require the use of hand-made prior distributions and mixing-enhancers, such as facilitating the jumps between the prior peaks, but even then there would be considerable uncertainty connected to the identifiability of the components used. An alternative option could be to start off with a full three-tensor model, but allow the elimination of redundant components by explicitly bringing the volume of one or more tissue types to zero. This could conceivably be achieved using the reversible jump MCMC. We note that this is an interesting direction for future research (see Chapter 6). Even the method presented in this work, however, can reliably assign low volume fractions to the absent tissues in most voxels and it is not clear whether introducing the reversible jumps would help solve difficult cases.

2.1.2 Indeterminacy and sources of information

Fitting multi-tensor models to diffusion MRI data is generally considered an ill-posed problem. Indeed, careful examination of Equation 2.6 shows that a small variation in some parameters can be balanced by adjusting the other parameters so that the diffusion profile remains the same. As an example, let us consider the following transformation:

$$\begin{aligned} S_{\mathrm{GM}} &\rightarrow S_{\mathrm{GM}} + \Delta S_{\mathrm{GM}} \\ v_2 &\rightarrow v_2 \frac{S_{\mathrm{GM}}}{S_{\mathrm{GM}} + \Delta S_{\mathrm{GM}}} = v_2 Q_{\mathrm{GM}} \\ S_{\mathrm{WM}} &\rightarrow S_{\mathrm{WM}} \frac{1 - v_2}{1 - v_2 Q_{\mathrm{GM}}} \end{aligned}$$

Both S_0 and S_i (for $i = 1 \ldots n$) defined in Equation 2.6 are invariant under this transformation as any change ΔS_{GM} of S_{GM} is absorbed into the other two parameters, v_2 and S_{WM}. In other words, all parameter values produced by the transformations similar to the one above explain the measured signal equally well. The tissue dependent diffusion model thus suffers from parameter indeterminacy, at least as far as the likelihood is concerned. Additionally, some components might become indistinguishable for some parameter values. Consider for instance the case when the estimated anisotropy of the white matter term (controlled by d_Δ) is low. There will be large uncertainty between the white and grey matter volumes, since their contributions to the signal will be very similar.

The main source of information that helps overcome the indeterminacy issues are weak plausibility constraints. They are introduced using broad Gamma distributions as priors for the signal and diffusivity parameters (see Section 3.1.2 for a practical

example). This ensures that the parameters stay within reasonable regions of space. Additionally, in some cases the adjustments needed to keep the predicted signal constant under the transformations such as the one shown above turn out to be large. For example, if $\Delta S_{\mathrm{GM}} = 0.1 \times S_{\mathrm{GM}}$ and $v_2 = 0.8$, it turns out that S_{WM} has to be reduced by a quarter: $S_{\mathrm{WM}} \rightarrow 0.73 \times S_{\mathrm{WM}}$. The results presented in Section 2.5 suggest that the plausibility priors we use are sufficient to produce accurate and reliable estimates the posterior distribution over the parameters of the tissue dependent diffusion model.

2.2 Noise model

We assume the values measured from different voxels to be independent. We also assume the diffusion-weighted measurements with different gradient directions as well as the T_2-weighted signal to be independent and Rician distributed. The resulting likelihood is a product of Rice distributions:

$$p(y_{ij}|\omega_j) = \mathrm{Rice}(y_{ij}|S_{ij},\varsigma_j) \quad \text{and} \tag{2.7}$$

$$p(Y|\Omega) = \Pi_{j=1}^{m}\Pi_{i=1}^{n} p(y_{ij}|\omega_j), \tag{2.8}$$

where ς_j is the Rician scale parameter. It quantifies the dispersion of the distribution, but is not equal to the standard deviation (root of variance). ς completes the tissue dependent diffusion model's parameter set, which totals 12 variables for a single voxel:

$$\omega = (S_{\mathrm{CSF}}, S_{\mathrm{GM}}, S_{\mathrm{WM}}, v_1, v_2, d_{\mathrm{CSF}}, d_{\mathrm{GM}}, d_{\perp}, d_{\Delta}, \theta, \phi, \varsigma)$$

The Rice distribution is given by:

$$\mathrm{Rice}(y_{ij}|S_{ij},\varsigma_j) = \frac{y_{ij}}{\varsigma_j^2} \exp\left(\frac{-(y_{ij}^2 - S_{ij}^2)}{2\varsigma_j^2}\right) I_0\left(\frac{y_{ij}S_{ij}}{\varsigma_j^2}\right),$$

where $I_0(\cdot)$ is the modified Bessel function of the first kind with order zero. This distribution arises from the theoretical description of the MRI measurement process. Unlike Gaussian noise, it's guaranteed to produce positive signal values. The tail of the Rice distribution is also heavier than that of a Gaussian, which makes the parameter estimation less sensitive to outliers.

2.3 Parameter estimation

2.3.1 Markov chain Monte Carlo

Having defined a forward model of diffusion, the model that predicts the signal measured in a diffusion-weighted MRI experiment, we now turn to the question of finding good parameter values for this model given the observed data. A simple approach might involve searching for values that minimise the difference between the predicted and observed signal values, for example using non-linear least-squares methods (the signal is a non-linear function of the parameters, so ordinary least-squares approach is not applicable). Minimising sum squared error is equivalent to maximum likelihood (ML) estimation using additive Gaussian noise, which is a theoretically incorrect noise model for MRI imaging (see Section 2.2). More importantly, ML approaches are prone to instability in the context of the tissue dependent diffusion model, due to the indeterminacy issues described in Section 2.1.2.

The inclusion of prior distribution over the model's parameters is not only a way to stabilise the estimation, but can also be used to encode additional information, such as spatial coherence constraints, anatomical plausibility or information obtained by segmenting other MRI modalities. Combining the prior distribution $p(\omega)$ with the likelihood $p(y|\omega)$ yields the posterior distribution over the parameters, given by the Bayes formula:

$$p(\omega|y) = \frac{p(y|\omega)p(\omega)}{\int_\omega p(y|\omega)p(\omega)}, \tag{2.9}$$

where y is the observed data and ω are the model's parameters. Maximum posterior (MAP) estimation is the equivalent of ML estimation in the context of $p(\omega|y)$. Unfortunately, the mode needs not be representative of the entire distribution. A better approximation is offered by Monte Carlo methods, which summarise the distribution by a collection of random samples that can be used, for example, for computing expectations. In particular, Markov chain Monte Carlo (MCMC) methods gather samples from a *stationary* or *target distribution* (in this thesis, $p(\omega|y)$) by generating, at each step, a new parameter configuration based on the current one. For example, Metropolis-Hastings sampler proposes parameter space jumps according to a *proposal distribution* centered on the current state. The jumps are then accepted or rejected according to the criterion designed to ensure convergence to the stationary distribution of the chain regardless of the choice of the initial state.

Two related issues have to be kept in mind when using MCMC sampling methods.

Given that the starting position of the chain is not, as a rule, drawn from the target distribution, the sampling chain needs time to converge to the target distribution and 'forget' this starting position. For this reason the samples are not collected during the initial *burn-in* period. Secondly, it takes time for the sampler to 'forget' the current state; in general, every state will be strongly correlated with the previous one. In order to gather independent samples from the target distribution, only every *n*th sample is usually saved, where *n* can be heuristically assessed by examining the autocorrelation of the sampling chain.

A thorough review of MCMC methods is provided in Neal's *Probabilistic Inference Using Markov Chain Monte Carlo Methods* [84]; a brief introduction can be found in any machine learning textbook, for example in Bishop's *Pattern Recognition and Machine Learning* [22].

2.3.2 Sampling procedure

MCMC sampling is used to estimate posterior distributions over the parameters of interest (Ω); the algorithm of choice is a one-dimensional Metropolis-Hastings sampler with a Gaussian proposal distribution. The variance of this distribution is adapted during the burn-in phase in order to attain the acceptance rate of roughly 50%. This variance tuning is a crucial part of any efficient Metropolis-Hastings sampling scheme as excessively small or large acceptance rates indicate slow exploration of the posterior distribution. A phased burn-in have been designed in order to ameliorate the issue of the identifiability of the model components outlined in Section 2.1.2, above. In each phase (see Figure 2.1), some of the variables remain fixed, while others are allowed to explore the space and reach the regions of high posterior probability. In particular, the first phase allows the angular adjustment of the anisotropic component without changing any other variables. The second phase is designed to move the volume fractions to the approximately correct region of the parameter space without changing the diffusivity ($d_\cdot$) or T_2-weighted signal ($S_\cdot$) values. Without this constraint, white matter diffusivity, d_Δ, might get stuck in the low value region (which is normally not where it should be) and this would prevent correct volume fraction estimation because white and grey matter components would become indistinguishable. The volume fractions in all voxels are initialised to ($v_{\mathrm{CSF}} = 1/3$, $v_{\mathrm{GM}} = 1/6$ and $v_{\mathrm{WM}} = 1/2$), initial fibre orientations are drawn from the prior distribution and other variables are set to their prior means. This set-up ensures that all compartments have non-zero volumes and can

adjust their parameters to the data in the first and second phases of the burn-in.

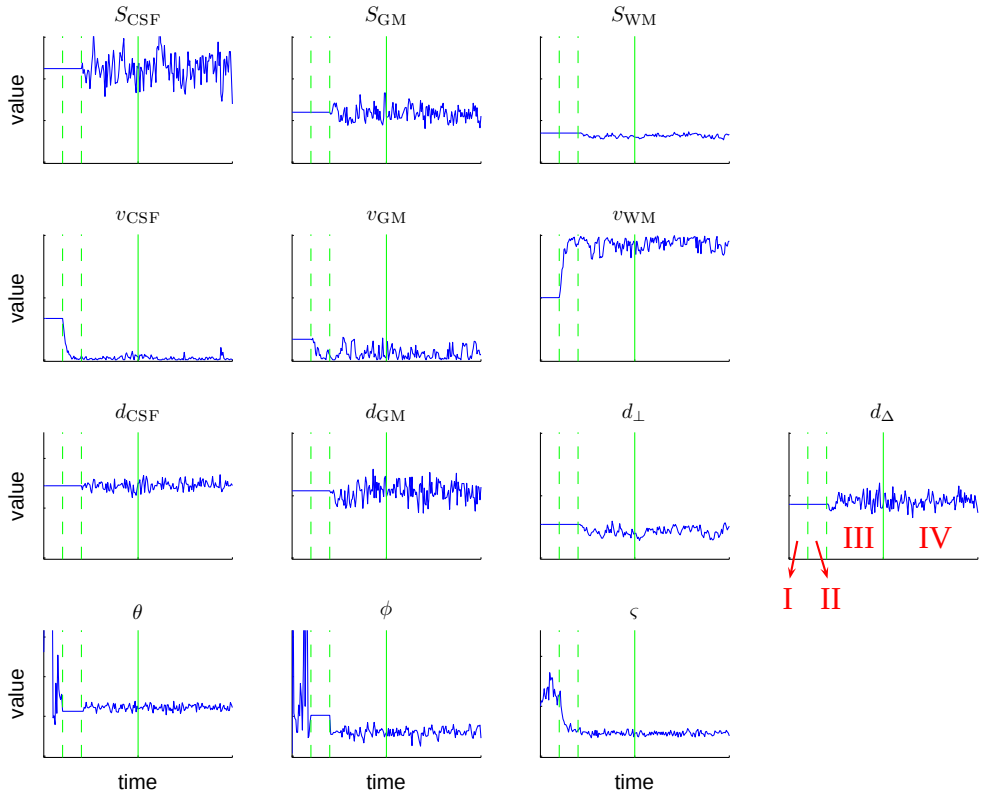

Figure 2.1: Example set of sample traces for a single voxel. Vertical lines separate angular burn-in (I), volume burn-in (II), all-variables burn-in (III) and the sampling phase (IV).

It is usually not desirable to perform Metropolis-Hastings MCMC in a space where hard constraints are placed on some variables. This is the case here as the T_2-weighted signal ($S_.$) and diffusivity ($d_.$) parameters are required to be positive and the volume fractions (v_1, v_2) vary from 0 to 1. We apply a standard technique of sampling in the space where all variables are unconstrained. In particular, positive variables are transformed into the log space and the vs into the inverse-sigmoid space using:

$$v_{\mathrm{sig}} = \log\left(\frac{v}{1-v}\right)$$

Collected samples are then transformed back into the original space.

2.4 Implementation

All data handling, parameter estimation and plotting has been implemented in Matlab (`http://www.mathworks.co.uk/products/matlab/`), a high level, interpreted lan-

guage for numerical computation. This includes in particular the sampling procedure outlined in Section 2.3.2, as well as custom plotting routines used to produce volume-scaled maps and fibre orientation plots used in Chapter 3 (see Figures 3.17, 3.13, 3.14) and signal space plots used in Chapter 5 (see Figure 5.5), adding up to over 4000 lines of code in the core module and 12000 in total. As detailed in Section 2.2, the tissue dependent diffusion model is defined by 12 parameters in each voxel. For each parameter, the proposal distribution and the unnormalised log posterior distribution are evaluated at each step of the estimation. With 500-step burn-in and 1000-step sampling (see Section 3.1.3), it adds up to 1.8×10^4 such operations for a single voxel. A typical brain mask used in this thesis contains 10^5 voxels (out of more than 10^6 image voxels), leading to over 10^9 MCMC jumps for a whole brain parameter estimation (saving around 10^8 parameter samples). A single estimation run can take up to a month on a stand-alone server. For this reason, all whole brain estimation runs were performed on a computational cluster provided by the Edinburgh Compute and Data Facility (ECDF, `http://www.ecdf.ed.ac.uk/`), using up to around 100 nodes at a time, depending on the overall load (number of other jobs on the cluster).

2.5 Evaluation of the results

2.5.1 Reconstruction of synthetic spatial maps

In order to validate our approach on diffusion MRI data with known ground truth, we have created a synthetic spatial diffusion MRI phantom. A simple geometry was overlaid on top of a 24×24×24 grid of sub-voxels defining a true pure-tissue segmentation (see Figure 2.2, left-hand side of each column). Mimicking the human brain imaging protocol described in Section 3.1.1, 7 T_2- and 64 diffusion-weighted volumes were generated using realistic signal parameters and biologically plausible diffusivity parameters:

$$(S_{\text{CSF}}, S_{\text{GM}}, S_{\text{WM}}) = (2500; 1200; 700) \quad \text{and}$$

$$(d_{\text{CSF}}, d_{\text{GM}}, d_{\perp}, d_{\Delta}) = (2.9; 1.1; 0.54; 0.86) \times 10^3 \,\text{mm}^2\text{s}^{-1}$$

The values for the signal parameters above were found using a procedure similar to that described and illustrated in Section 3.1.2. The simulated signal was then integrated over 4×4×4 sub-voxel neighbourhoods to create a low-resolution, partial-volumed 6×6×6 image with known tissue volume fractions (see Figure 2.2, right-hand side

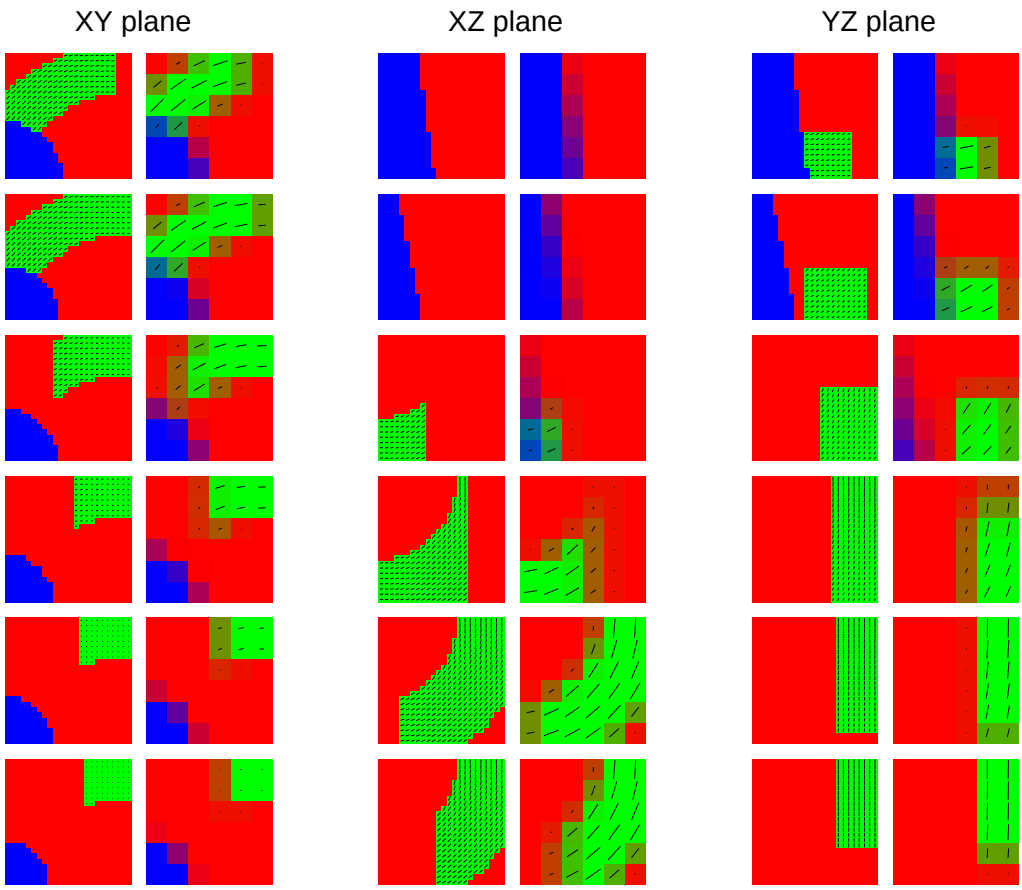

Figure 2.2: True segmentations (white matter, grey matter, cerebrospinal fluid) for the synthetic diffusion MRI phantom with fibre orientations overlaid as black bars. Each column features a different plane of view. The original, pure tissue map is shown on the left and the low-resolution map with partial volumes on the right of each column. Note that all slices of the partial volumed map are shown in the figure, but only every fourth slice of the original, high resolution image.

of each column). Finally, the data was made Rician distributed with different levels of noise ($\varsigma = 0, 50, 100, 150$). These values correspond to the signal-to-noise ratio of the real data; our own results from Section 3.4.2 suggest that for almost all voxels $\varsigma \in (0, 100)$ with a peak around 50 ($\varsigma = 150$ is thus a high noise regime). Figures 2.3, 2.4 and 2.5 show colour-coded maps of estimated volume fractions (posterior mean), as well as white matter fibre orientation (posterior mean as well). Excellent reconstruction is possible with noiseless data, but even with rather high ς the different tissues seem reasonably well separated and estimated orientation of the axonal bundles aligns well with the ground truth.

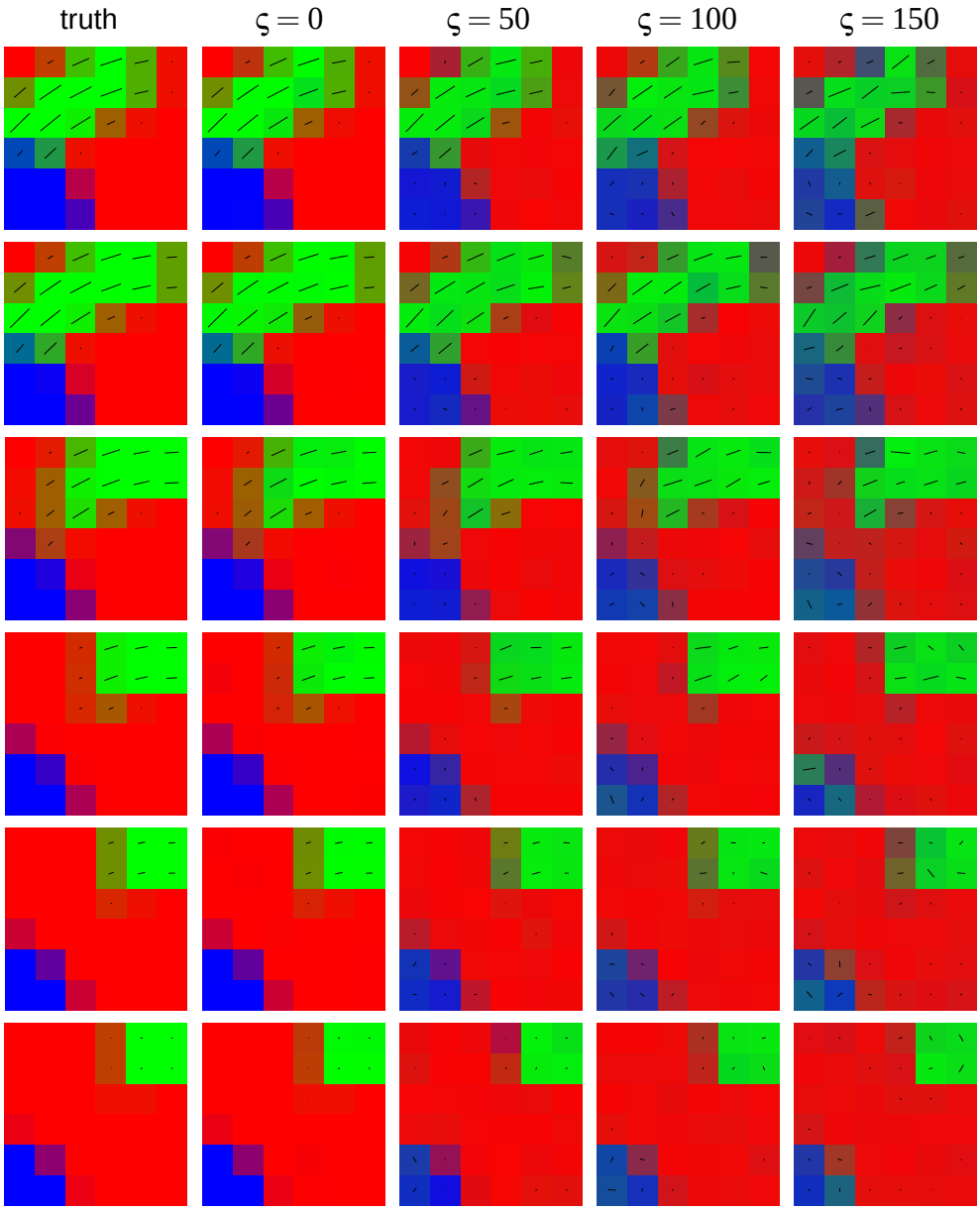

Figure 2.3: XY plane: True and reconstructed tissue maps (mean volume fractions of white matter, grey matter and cerebrospinal fluid) with different noise levels ς. True and estimated fibre orientations overlaid as black bars scaled according to the white matter volume fraction.

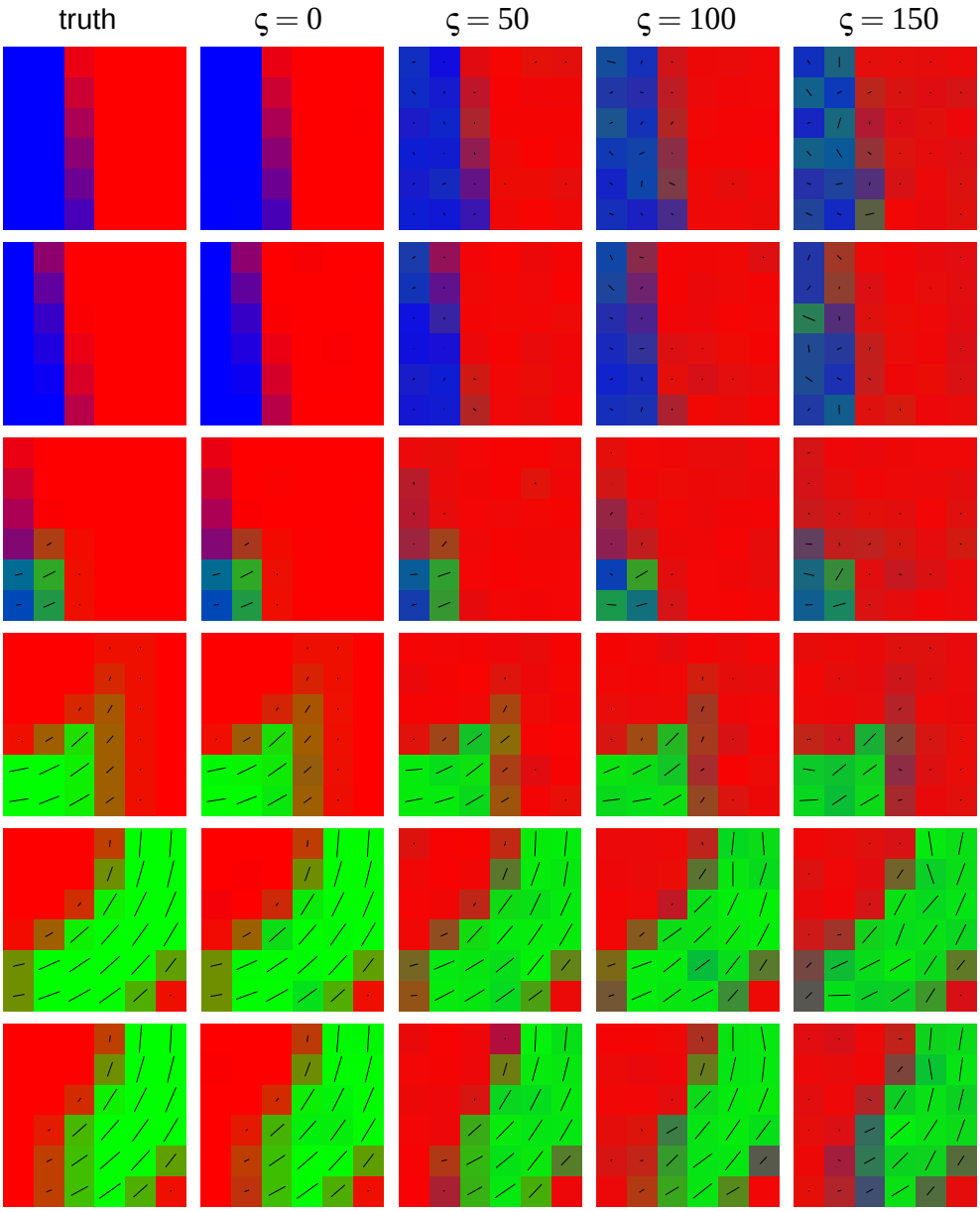

Figure 2.4: XZ plane: True and reconstructed tissue maps (mean volume fractions of white matter, grey matter and cerebrospinal fluid) with different noise levels ς. True and estimated fibre orientations overlaid as black bars scaled according to the white matter volume fraction.

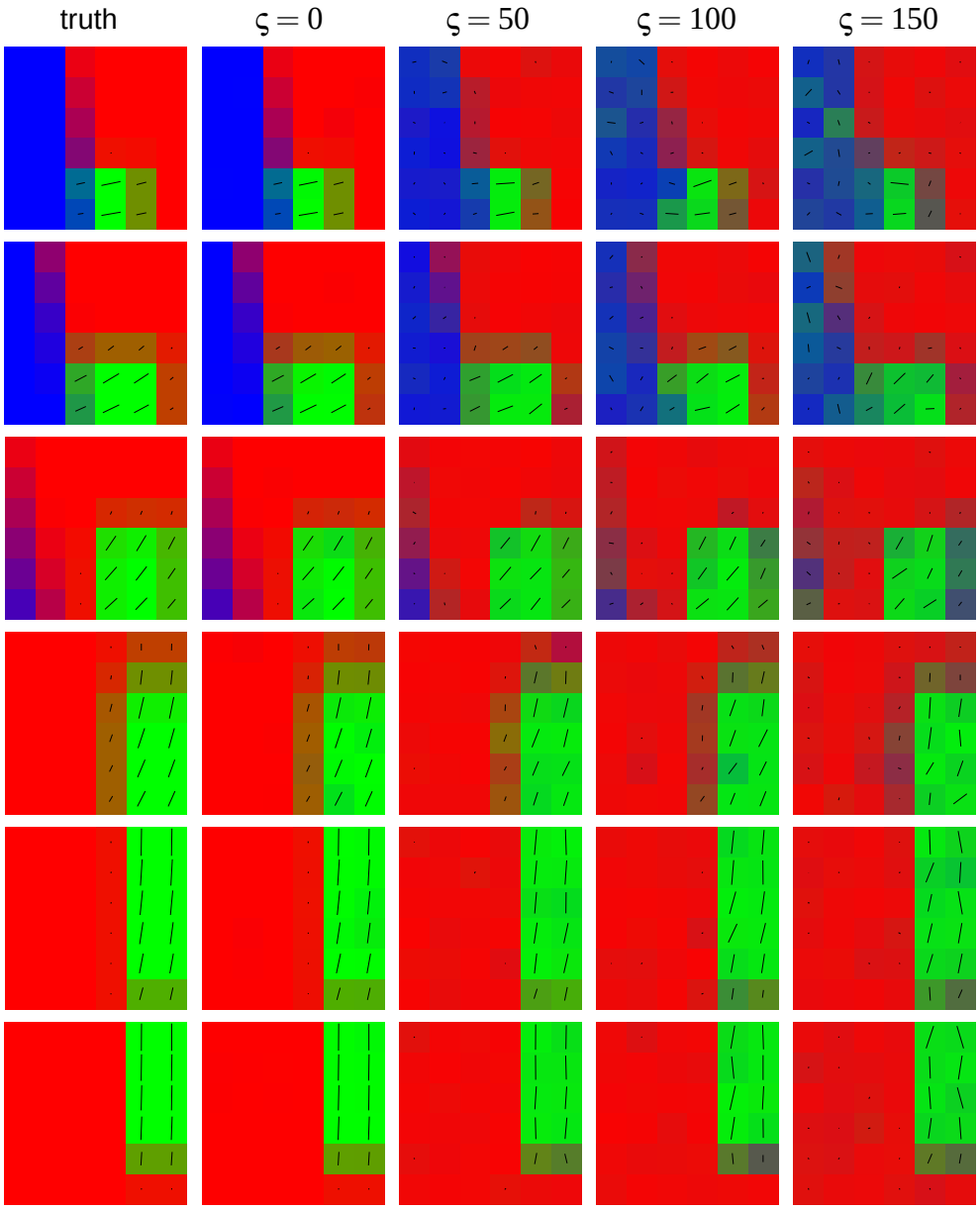

Figure 2.5: YZ plane: True and reconstructed tissue maps (mean volume fractions of white matter, grey matter and cerebrospinal fluid) with different noise levels ς. True and estimated fibre orientations overlaid as black bars scaled according to the white matter volume fraction.

2.5.2 Examining partial voluming description

The spatial phantom allows visual inspection of how the estimated tissue segmentations compare to the ground truth and how they change for different noise levels. To quantify how well particular partial volume effects are handled, however, we need to use a dataset with finer control over the parameters. To this end, we designed 3 phantoms, each containing a mixture of 2 tissue types:

- white matter and grey matter,
- white matter and cerebrospinal fluid,
- cerebrospinal fluid and grey matter.

We find these two-tissue phantoms more instructive than a hypothetical three-tissue dataset. Not only do they make the results easier to present and interpret, they also have more practical importance, as—given the scale of brain structures—there should be many more two-tissue-partial-volumed voxels compared to those containing all three tissue types. The proportion of the tissue types in each phantom was varied from 0 to 1 with a step of 0.05. T_2- and diffusion-weighted data were generated using the same parameter values as for the spatial phantom. Different Rician noise levels were tried, in the discussion below we present only the low noise ($\varsigma = 25$) and high noise ($\varsigma = 125$) regimes for clarity. Estimation for each set of parameter values was run 20 times to evaluate the reproducibility of the results.

Mean tissue volume fractions for the white–grey matter phantom are presented in Figure 2.6. Cerebrospinal fluid fraction stays consistently low (compared to the true 0). The other tissues' volumes are generally estimated correctly, although there is a visible tendency to explain noise effects using the white matter component in voxels where its true presence is marginal. As a result, there is a slightly enlarged white matter component, while the grey matter volume fraction is underestimated. This effect is markedly stronger for a higher noise level. Looking at the white matter–cerebrospinal fluid phantom (Figure 2.7), the cerebrospinal fluid volume fraction is, again, accurately estimated, as is white and grey matter volume for low noise level. Using data with more noise results in a spurious grey matter component appearing in voxels with strong partial voluming (as much as 0.2 of a voxel when the true proportion of white matter is 0.5–0.8). At the same time, the white matter volume is underestimated. The cerebrospinal fluid–grey matter phantom (Figure 2.8) is an interesting case, because the two components present can only be distinguished by taking into account the prior

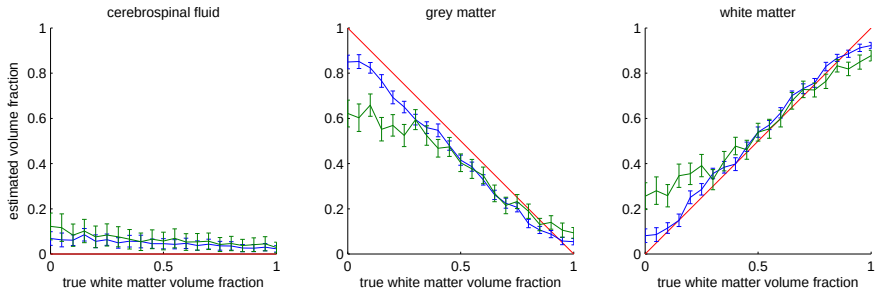

Figure 2.6: Estimated volume fractions for the white–grey matter phantom, based on low noise ($\varsigma = 25$) and high noise ($\varsigma = 125$) data. Error bars indicate posterior standard deviation and the means are across 20 repetitions of the same estimation procedure. Red lines correspond to the ground truth.

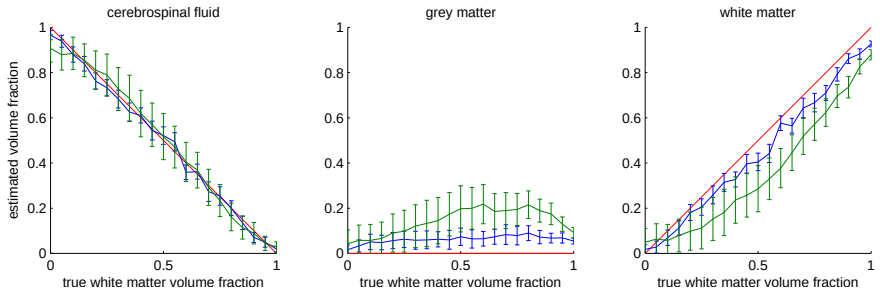

Figure 2.7: Estimated volume fractions for the white matter–cerebrospinal fluid phantom, based on low noise ($\varsigma = 25$) and high noise ($\varsigma = 125$) data. Error bars indicate posterior standard deviation and the means are across 20 repetitions of the same estimation procedure. Red lines correspond to the ground truth.

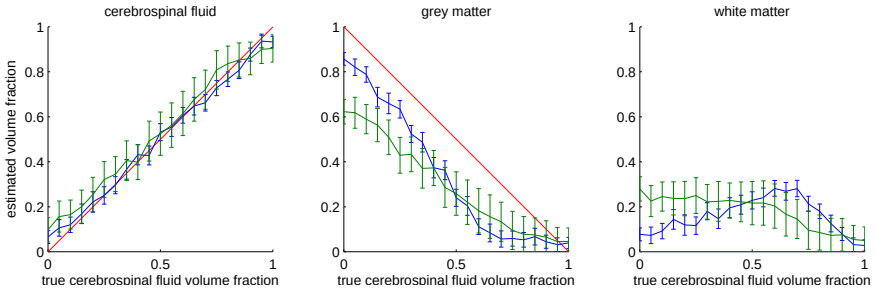

Figure 2.8: Estimated volume fractions for the cerebrospinal fluid–grey matter phantom, based on low noise ($\varsigma = 25$) and high noise ($\varsigma = 125$) data. Error bars indicate posterior standard deviation and the means are across 20 repetitions of the same estimation procedure. Red lines correspond to the ground truth.

knowledge about the typical signal values (encoded in gamma priors) — they are not identifiable given the signal alone. We find that the estimated cerebrospinal fluid volume is close to the true value, whereas the grey matter component appears smaller than it really is. This seems once again to be caused by the white matter term being used to explain the random effects of noise. The surprising finding is that low noise seems to impede the estimation in voxels composed predominantly from the cerebrospinal fluid more than high noise. For voxels where grey matter is the dominating tissue, the estimation with lower noise values is more accurate, as expected.

In all cases it is relatively easy to correctly estimate the proportion of cerebrospinal fluid in a voxel. Looking at the typical signal values in Table 2.1, it is easy to see why. While T_2-weighted signal for the cerebrospinal fluid (S_{CSF}) is significantly larger than for white or grey matter, the diffusion weighted signal is actually lower in both cases. This means that adding spurious cerebrospinal fluid volume will pull the voxel's total T_2-weighted signal up, but its diffusion-weighted signal down. Adjusting the contributions from the other components cannot cancel this effect and thus the overall fit is bound to deteriorate. This is unfortunately not the case for grey and white matter. Here, both T_2- and diffusion-weighted values for the grey matter are larger (or similar) to those for the white matter. As a result, incorrect volume fractions can in some situations be hidden by adjusting other parameters. The main source of information that aids the disambiguation of the two components is the shape of the diffusion attenuation profile, namely the amount of anisotropy.

Tissue type	Diffusivity $[10^{-3}\text{mm}^2/\text{s}]$	MRI signal	
		T_2-weighted	Diffusion weighted
Cerebrospinal fluid	$d_{CSF} = 3.19 \pm 0.10$	$S_{CSF} = 2673 \pm 482$	$S^{att}_{CSF} = 110 \pm 23$
Grey matter	$d_{GM} = 0.83 \pm 0.05$	$S_{GM} = 1202 \pm 182$	$S^{att}_{GM} = 524 \pm 84$
White matter (axial)	$d_{\parallel} = 1.40 \pm 0.24$	$S_{WM} = 690 \pm 138$	$S^{att}_{WM\parallel} = 171 \pm 54$
White matter (radial)	$d_{\perp} = 0.42 \pm 0.20$	$S_{WM} = 690 \pm 138$	$S^{att}_{WM\perp} = 455 \pm 130$

This means that in general:

$$d_{CSF} > d_{\parallel} > d_{GM} > d_{\perp} \tag{2.10}$$

$$S_{CSF} > S_{GM} > S_{WM} \tag{2.11}$$

$$\left[S^{att}_{GM} \approx S^{att}_{WM\perp}\right] > \left[S^{att}_{WM\parallel} \approx S^{att}_{CSF}\right] \tag{2.12}$$

Graphically:

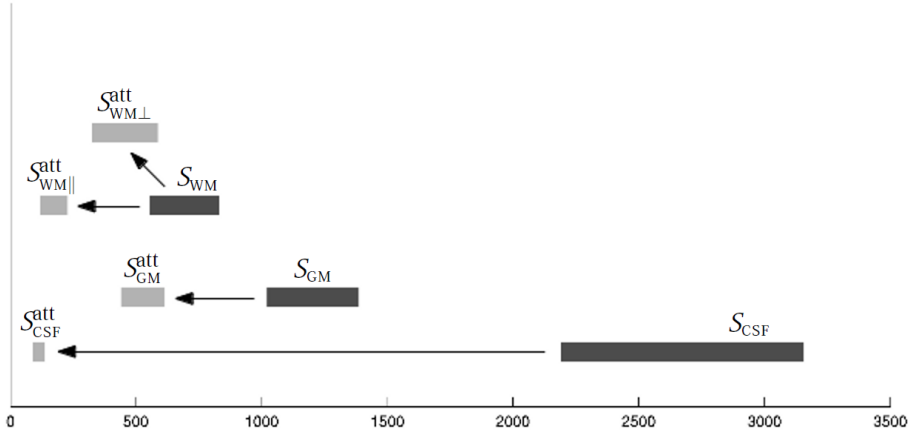

Table 2.1: Major brain tissue types and their typical diffusivities, as well as values of T_2- and diffusion-weighted signal. The diffusivity column is compiled on the basis of [94] (white matter) and [21] (grey matter and cerebrospinal fluid). Note that, while axial diffusivity of white matter (along the fibre direction) is not a variable in the tissue dependent diffusion model, it is easily calculated through $d_{\parallel} = d_{\perp} + d_{\Delta}$. T_2-weighted intensity depends on the scanner and acquisition parameters; signal values presented here are taken from the prior distributions fitted to the data acquired for this work (see Section 3.1.2 for estimation details). Given the T_2-weighted signal S and diffusivity d, the attenuated signal is given by $S^{att} = Se^{-bd}$. One standard deviation is given and displayed throughout.

2.5.3 Convergence assessment

When assessing the reliability of the MCMC sampling methods, two issues need attention: chain "mixing" and posterior approximation. Given a random starting point, the chain should reliably find the region of high posterior probability (mixing). States visited during this initial search phase (usually named burn-in) are discarded as they carry no information about the target distribution. Since burn-in has a fixed length in most applications, it is crucial that typical posterior region(s) are reached within this time regardless of the initial state. Once a high probability state is reached, the main issue remains the exploration of the target distribution. Since the aim is to obtain the sampling approximation to the true posterior, it is mandatory that the whole volume with non-negligible contribution to the target density is represented by the collected sample set. In particular, all relevant states need to be visited during the allocated number of sampling steps.

The effectiveness of sampling space exploration during the mixing phase was demonstrated in Sections 2.5.1 and 2.5.2, where the chains clearly succeeded in reaching the regions close to the known ground truth. The remaining question is whether a representative sample from the posterior distribution is collected after the burn-in. The two tools employed for this purpose are autocorrelations of the sample traces and the analysis of the distributions obtained by running independent, overdispersed chains. Note that any problems with the mixing would show here as well, because samples from non-mixed chains do not, by definition, come from the target distribution.

Chain autocorrelation

The quality of the posterior approximation is related to the amount of correlation between the subsequent states of the Markov chain. If the autocorrelation is large, every step brings little information in addition to the previous one and the effective sample size is low; for this reason in typical MCMC applications only one in every few samples is saved and used to approximate the posterior distribution. Given a chain of samples ξ_t, where $t = 1, \ldots, n$, we define the autocorrelation[2] with lag τ as:

$$C(\tau) = \frac{\sum_{t=1}^{n}(\xi_{t+\tau} - \overline{\xi})(\xi_t - \overline{\xi})}{n\sigma_\xi^2} \tag{2.13}$$

Plots of C can be found in Figures 2.10–2.16, along other convergence diagnostics. For comparison, example autocorrelation plots for independent and dependent sample

[2]The same quantity is sometimes referred to as auto-covariance.

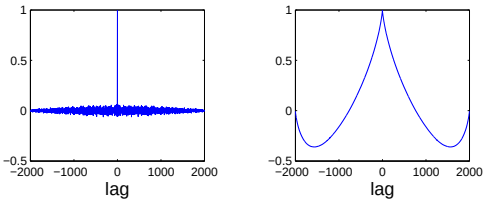

Figure 2.9: On the left, autocorrelation of a "chain" of samples drawn independently from a standard Gaussian distribution. On the right, autocorrelation of the same sample set after sorting the values. Compare to figures 2.10–2.16.

sets are presented in Figure 2.9. Note that for the independent samples the values of autocorrelation are randomly distributed around 0 (apart from zero lag where each sample is correlated with itself). For dependent sample chains, this is typically not the case and there is a certain non-zero lag for which the neighbouring states are still significantly correlated.

Multiple chains analysis

Without knowing the form or the moments of the true posterior distribution (as is the case with the tissue dependent diffusion model developed in this work), convergence assessment methods use multiple sampling chains. The distributions implied by each of these chains are then implicitly compared to the distribution obtained by using the samples from all the chains together. A variant of this method due to Brooks and Gelman [24] is used below.

We start by considering a set of samples ξ of one parameter coming from m chains of n samples each. ξ_{jt} is the tth sample from the jth chain. Mean within-chain variance W and between-chain variance B/n are given by:

$$W = \frac{1}{m(n-1)} \sum_{j=1}^{m} \sum_{t=1}^{n} \left(\xi_{jt} - \overline{\xi}_{j\cdot} \right)^2 \tag{2.14}$$

$$B/n = \frac{1}{m-1} \sum_{j=1}^{m} \left(\overline{\xi}_{j\cdot} - \overline{\xi}_{\cdot\cdot} \right)^2, \tag{2.15}$$

where $\overline{\xi}_{j\cdot}$ denotes a jth chain's mean and $\overline{\xi}_{\cdot\cdot}$ is all-samples mean. Combining these quantities gives the pooled estimate $\widehat{V}$ of the posterior variance σ^2:

$$\widehat{V} = \frac{n-1}{n} W + \frac{m+1}{m} B/n \tag{2.16}$$

The ratio $\widehat{V}/\sigma^2 = R$ is called a scale reduction factor (or variance reduction factor). Large values of R strongly suggest that further sampling is needed. True σ^2 is un-

known, but we can replace it by W, thereby computing the potential scale reduction factor:

$$\widehat{R} = \frac{\widehat{V}}{W} \tag{2.17}$$

Since W underestimates σ^2, $\widehat{R}$ is an overestimate of R. At convergence, $\widehat{R}$ should approach unity while both $\widehat{V}$ and W should stabilise and stay roughly constant as new samples are gathered. This second condition is important to prevent prematurely diagnosing convergence when $\widehat{R}$ is low, but $\widehat{V}$ and W keep changing. If either condition is not met, further sampling is needed. The converse is not true, so the convergence cannot be guaranteed, only the lack of convergence can be diagnosed. Keeping this caveat in mind, a graphical approach to monitoring convergence is to compute $\widehat{R}$, $\widehat{V}$ and W for $\tilde{n}$ first samples; values for different $\tilde{n}$s are then plotted as a trace. When the convergence criteria outlined above are met, the sample set up to time $\tilde{n}$ is deemed to be representative of the target distribution.

Results

Three partial volumed synthetic datasets were used, representing all possible combinations of the three tissues, as in Section 2.5.2. For each mixture the two tissues occupy an equal volume fraction i.e. a half of a voxel. Fifty sampling chains were run for 2000 steps after the burn-in, saving every sample. The starting points of the chains were overdispersed with respect to the posterior distribution. The initial state for the tissue parameters ($S_{\text{CSF}}, S_{\text{GM}}, S_{\text{WM}}, d_{\text{CSF}}, d_{\text{GM}}, d_{\perp}, d_{\Delta}$) as well as fibre angles (θ and ϕ) and noise level (ς) were drawn from their prior distributions. Volume fractions (v_1, v_2) were initialised to the usual values to facilitate the custom burn-in schedule as explained in Section 2.3.2. Therefore the starting volume fractions were not equal to the true values for any of the phantoms. It is worth noting that while the prior distributions for the tissue parameters ensure that they will be within a sensible ranges at the start, the priors for the angles are non-informative. Therefore the initial values can be implausible given the data. We find that this does not affect the mixing or convergence of our sampling method.

Plots of W and $\widehat{V}$, $\widehat{R}$ and additionally the autocorrelation of the chains are shown in Figures 2.10–2.16. Inspecting the convergence diagnostics for the T_2-weighted signal and diffusivity parameters, it seems that even 1000 steps are sufficient to approximate their posterior distributions for all three phantoms used. The autocorrelations also indicate that the samples are nearly independent (or weakly dependent in some cases).

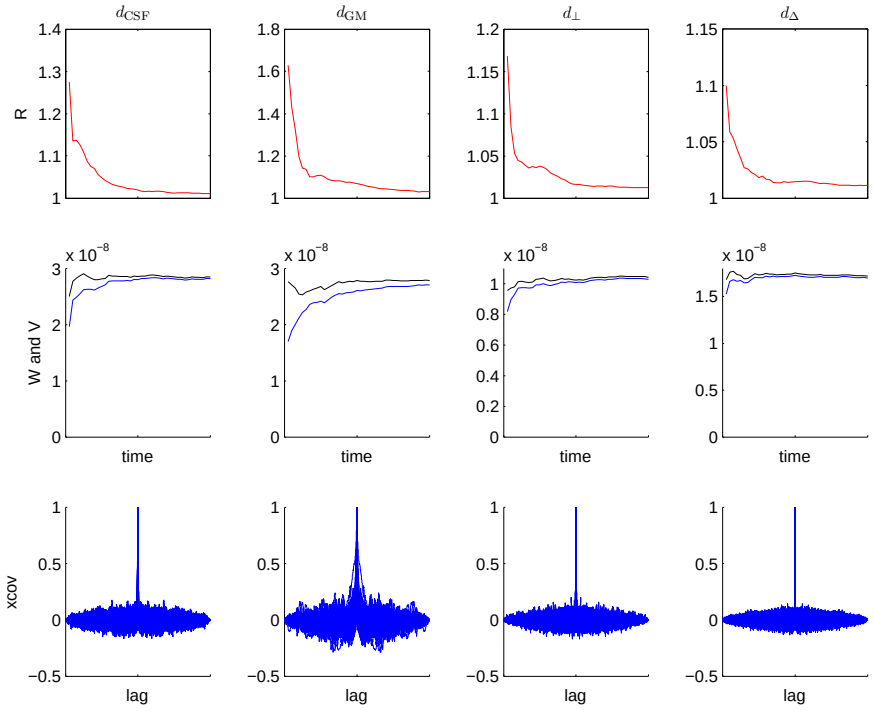

Figure 2.10: Cerebrospinal fluid–grey matter phantom. Columns: d_{CSF}, d_{GM}, $d_{\perp}$, d_{Δ}. Rows: Potential Scale Reduction Factor ($\widehat{R}$), within-chain (W, blue) and estimated posterior ($\widehat{V}$, black) variance, autocorrelation of the sample chains (overlaid for all 50 chains). Note that $W < \widehat{V}$ in all plots, in all figures.

Turning to the volume fractions in Figure 2.16, we see that it is more difficult to obtain a good posterior approximations, particularly for v_2. We still conclude that running the chains for longer than 1000 steps does not significantly improve the results. The subsequent volume samples are also more strongly correlated than for other parameters. It will therefore make sense to discard all but every tenth sample in order to keep an independent sample set.

Multivariate analysis

Extension of the above diagnostic method to the multivariate case is straightforward. In addition to monitoring the variances for all the variables separately, it is necessary to take the covariances into account. Let us redefine ξ_{jt} as a vector of length p, the dimensionality of the state space. W and B become $p \times p$ matrices:

$$W = \frac{1}{m(n-1)} \sum_{j=1}^{m} \sum_{t=1}^{n} \left(\xi_{jt} - \overline{\xi}_{j\cdot}\right) \left(\xi_{jt} - \overline{\xi}_{j\cdot}\right)^{T} \tag{2.18}$$

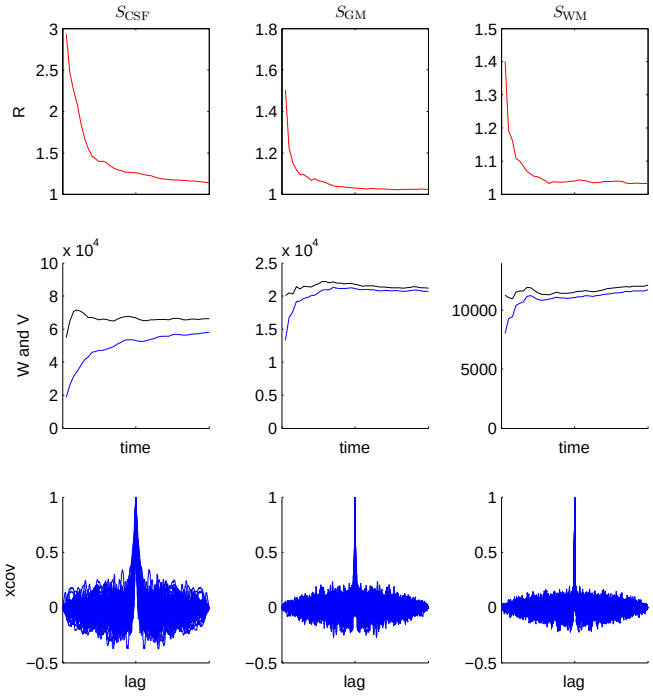

Figure 2.11: Cerebrospinal fluid–grey matter phantom. Columns: S_{CSF}, S_{GM}, S_{WM}. Rows: Potential Scale Reduction Factor ($\widehat{R}$), within-chain (W, blue) and estimated posterior ($\widehat{V}$, black) variance, autocorrelation of the sample chains (overlaid for all 50 chains).

$$B/n \;=\; \frac{1}{m-1}\sum_{j=1}^{m}\left(\overline{\xi}_{j\cdot}-\overline{\xi}_{\cdot\cdot}\right)\left(\overline{\xi}_{j\cdot}-\overline{\xi}_{\cdot\cdot}\right)^{T}, \tag{2.19}$$

where p is the number of dimensions. $\widehat{V}$ is also a $p \times p$ matrix, given by (2.16). A multivariate potential scale reduction factor $\widehat{R}^p$ can be defined using a matrix distance measure between $\widehat{V}$ and W:

$$\widehat{R}^p = \max_{\mathbf{a}} \frac{\mathbf{a}^T\widehat{V}\mathbf{a}}{\mathbf{a}^T W\mathbf{a}} \tag{2.20}$$

As before, $\widehat{R}^p$ goes to unity as convergence is reached. Brooks and Gelman [24] suggest monitoring both the univariate diagnostics ($\widehat{V}$ vs W and $\widehat{R}$) and the multivariate potential scale reduction factor $\widehat{R}^p$.

The traces of $\widehat{R}^p$ for all three phantoms are shown in Figure 2.17. The value of this diagnostic stabilises in the region of 2, rather than 1 in all cases. This is to be expected in the light of the indeterminacy issues discussed in Section 2.1.2. We have shown in previous sections (2.5.1–2.5.2) that the mean posterior estimates are meaningful and reliably close to the known ground truth. Posterior distributions over most parameters are also reasonably good approximations, even though perfect convergence seems elusive.

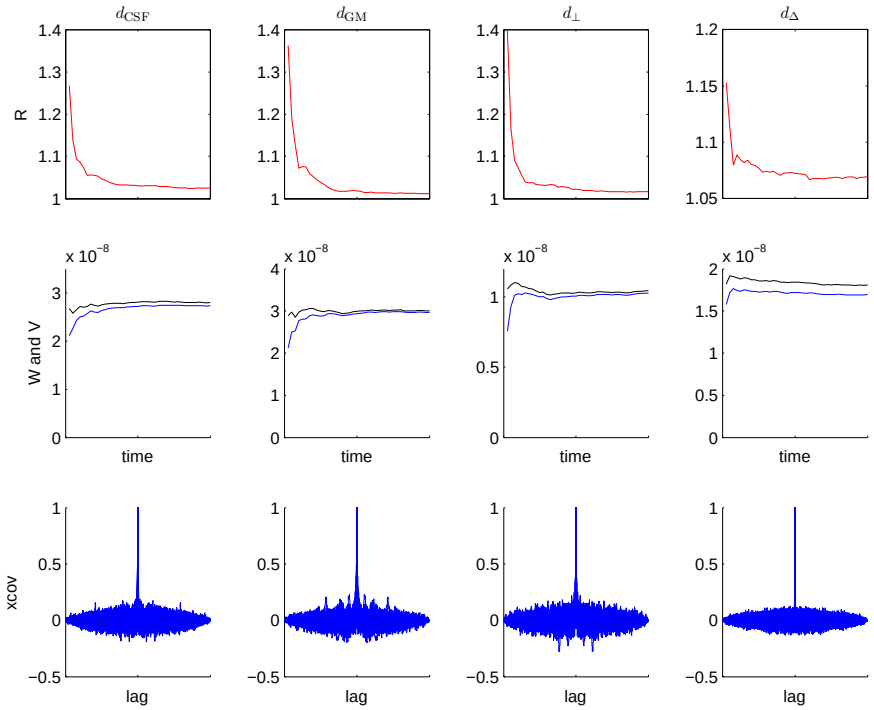

Figure 2.12: White matter–cerebrospinal fluid phantom. Columns: d_{CSF}, d_{GM}, $d_{\perp}$, d_{Δ}. Rows: Potential Scale Reduction Factor ($\widehat{R}$), within-chain (W, blue) and estimated posterior ($\widehat{V}$, black) variance, autocorrelation of the sample chains (overlaid for all 50 chains).

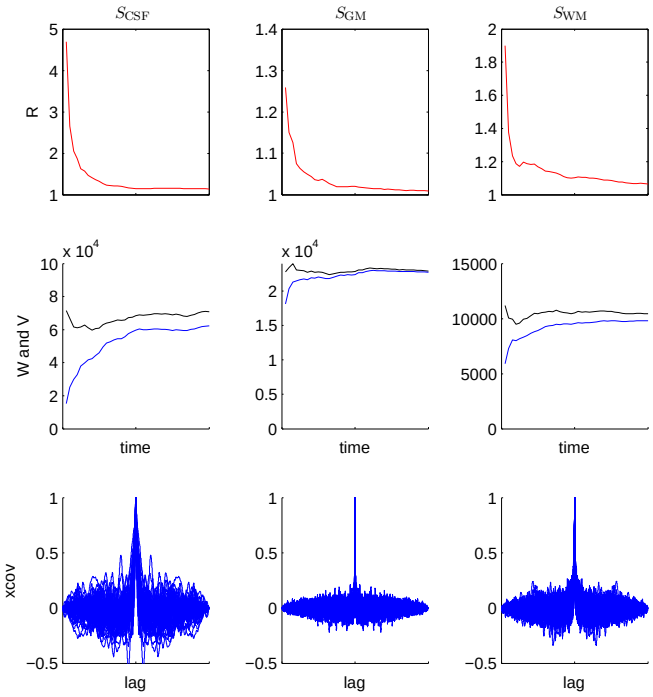

Figure 2.13: White matter–cerebrospinal fluid phantom. Columns: S_{CSF}, S_{GM}, S_{WM}. Rows: Potential Scale Reduction Factor ($\widehat{R}$), within-chain (W, blue) and estimated posterior ($\widehat{V}$, black) variance, autocorrelation of the sample chains (overlaid for all 50 chains).

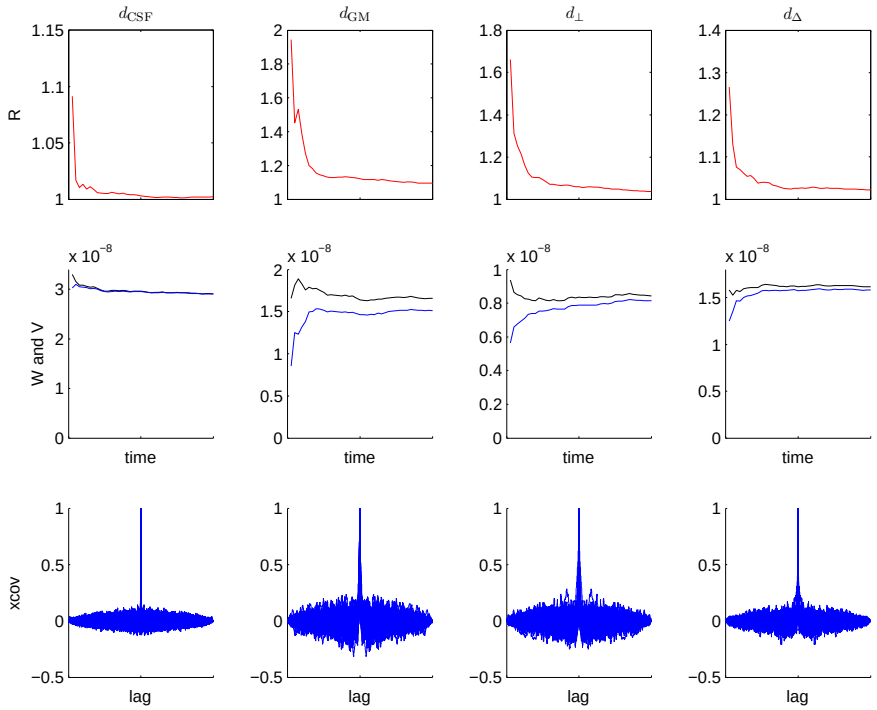

Figure 2.14: White–grey matter phantom. Columns: d_{CSF}, d_{GM}, $d_{\perp}$, d_{Δ}. Rows: Potential Scale Reduction Factor ($\widehat{R}$), within-chain (W, blue) and estimated posterior ($\widehat{V}$, black) variance, autocorrelation of the sample chains (overlaid for all 50 chains).

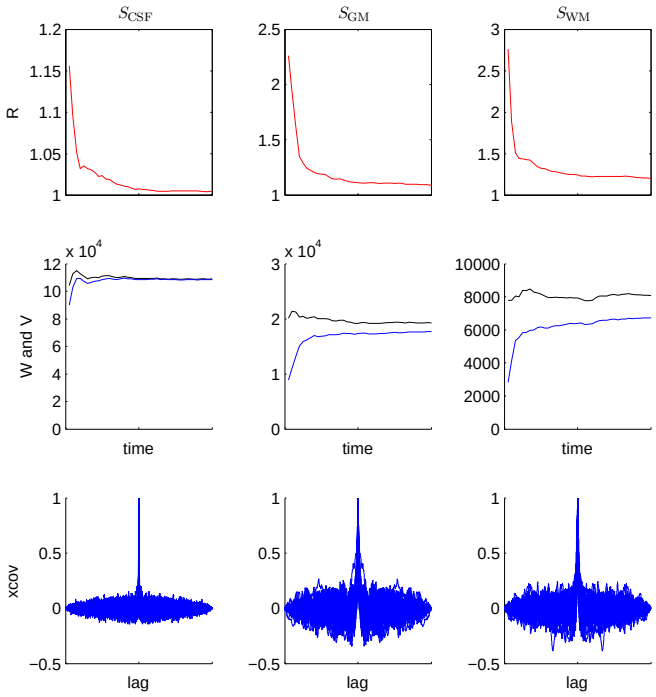

Figure 2.15: White–grey matter phantom. Columns: S_{CSF}, S_{GM}, S_{WM}. Rows: Potential Scale Reduction Factor ($\widehat{R}$), within-chain (W, blue) and estimated posterior ($\widehat{V}$, black) variance, autocorrelation of the sample chains (overlaid for all 50 chains).

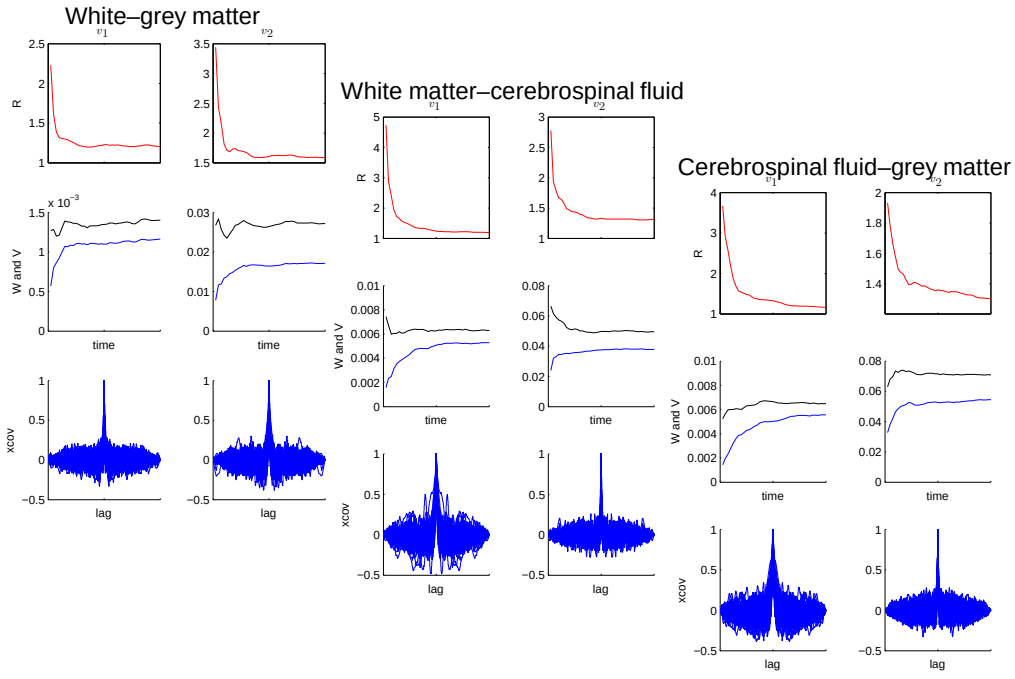

Figure 2.16: All phantoms: v_1 (left) and v_2 (right). Rows: Potential Scale Reduction Factor ($\widehat{R}$), within-chain (W, blue) and estimated posterior ($\widehat{V}$, black) variance, autocorrelation of the sample chains (overlaid for all 50 chains).

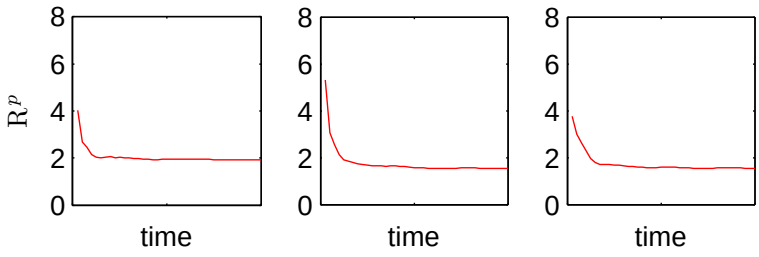

Figure 2.17: Multivariate potential scale reduction factor for all three phantoms: white–grey matter (left), white matter–cerebrospinal fluid (centre) and cerebrospinal fluid–grey matter (right).

2.6 Conclusions

This chapter laid the foundations for the joint estimation of volume and diffusivity parameters of three major tissue types in partial volumed (and pure tissue) voxels using the tissue dependent diffusion model, a three-tensor model where each Gaussian diffusion compartment corresponds to a different tissue type: white matter, grey matter and cerebrospinal fluid. Parameter estimation for this type of model is challenging due to indeterminacies in the forward model of diffusion, which mean that different parameter settings might produce an identical signal profile and that under some circumstances the terms corresponding to different tissue types might become indistinguishable from one another. Nevertheless, we have shown that sampling from the posterior distribution over the model's parameters is possible using careful sampling procedure with custom burn-in and incorporating prior knowledge about the reasonable parameter values through prior distributions.

The estimation procedure has been tested on a range of synthetic datasets, allowing visual inspection of the reconstructed spatial maps with known ground truth, quantitative assessment of the description of partial voluming in different two-tissue scenarios and diagnosis of the convergence of the sampling chains to the posterior distribution. While the convergence diagnostics for the volume fractions and in the multivariate case (jointly for all variables) indicate less than perfect convergence, other convergence and synthetic data results support the reliability of our approach. It needs to be kept in mind that testing the tissue dependent diffusion model on synthetic data can only provide a preliminary validation of the method; its usefulness depends on how well its results describe the data from human subjects. This question is the focus of Chapter 3.

Chapter 3

Human brain results

Chapter 2 introduced a new forward model of water diffusion in brain tissue accounting for partial volume effects, the tissue dependent diffusion model. A procedure to robustly estimate the posterior distributions over the parameters of interest was also presented. The plausibility and reliability of this approach were validated on synthetic datasets. This chapter goes one step further by looking at the applications of the method on real data and evaluating the results.

It is worth reiterating that the quantities estimated with the tissue dependent diffusion model are the volume fractions of white matter, grey matter and cerebrospinal fluid, white matter fibre orientations and additional tissue and noise parameters. Variables from each of these three groups are visualised on whole-brain and ROI maps for different subjects, cross-sections and slices. The objective of this presentation is to enable qualitative assessment of the plausibility of our results. Where possible, comparisons with standard or well established methods are also performed.

3.1 Materials and Methods

3.1.1 Imaging

Using a GE Signa 1.5T MRI scanner, 9 healthy volunteers aged 25–59 underwent a whole brain diffusion MRI exam (voxel dimension $2\times2\times2$mm), based on single-shot spin-echo EPI, which consisted of 7 T_2- and 64 diffusion-weighted (b = 1000 s/mm^2) volumes. 72 contiguous, 2mm thick slices were obtained, using a field of view of 256×256mm and 128×128 acquisition matrix, yielding a resolution of $2\times2\times2$mm. Echo time was 98ms and repetition time was 16.5s. The diffusion MRI data were then

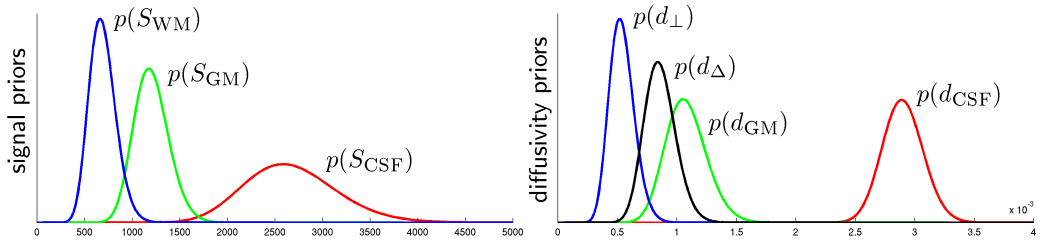

Figure 3.1: Gamma prior distributions for the T_2-weighted signal (left) and diffusivity (right) parameters. Diffusivity units are mm^2/s.

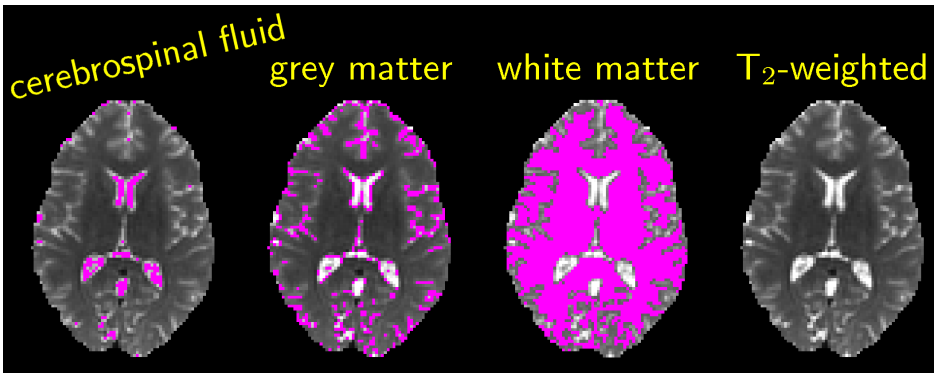

Figure 3.2: Example axial slice showing masks for cerebrospinal fluid, grey and white matter (shown in magenta) selected through manual T_2-weighted intensity thresholding. The highlighted voxels were used to fit the prior non-diffusion-weighted signal distributions as detailed in the text. An unmasked mean T_2-weighted image is shown on the right-hand side for comparison.

preprocessed to remove skull data [98] and eddy current distortions using FSL tools [100, 121, 60]. Additional T_1-weighted volumes used in Section 3.2.3 were acquired using 3D inversion recovery based protocol, with 160 slices of width 1.3mm, a field of view of 256×256mm and 192×192 acquisition matrix, zero-filled to 256×256. Final resolution for these volumes was thus 1×1×1.3mm.

3.1.2 Modelling

Appropriate prior distributions are essential to the reliable and trustworthy estimation of the parameters of many models, including the tissue dependent diffusion model developed in this work. While the typical ranges for the diffusivity-related quantities can be found in the literature, the same cannot be said about the intensity of the T_2-weighted images, which depend on a number of acquisition-related factors that we do

not model explicitly. This is why, while the diffusivity priors (see Figure 3.1, right) can be set without looking at the data at all, the non-diffusion-weighted signal priors (Figure 3.1, left) cannot. We have proposed the following procedure in order to set the shape and scale parameters of the Gamma priors for these parameters. For each tissue type T_2-weighted intensity thresholds are adjusted manually for the mean non-diffusion-weighted volume, such that for a chosen intensity range only pure voxels of this tissue type are segmented (see Figure 3.2). Given this set of voxels, all measurements without the diffusion weighting (here: 7 per voxel) are then used as samples from which to estimate the relevant distribution parameters. The prior distributions obtained in this way are then flattened by increasing their variance by 10%. By using the priors estimated on the basis of a single brain volume we assume that the T_2-weighted intensities observed for this volume are representative of all the images from our cohort. This assumption is potentially limited by the amount inter-subject variability and scanner stability.

3.1.3 Estimation and results

In order to collect samples from the posterior distribution over the parameters of the model, we use the Metropolis-Hastings MCMC sampler described in Chapter 2. As detailed in Section 2.3.2, the volume fractions in all voxels are initialised to the same non-zero default values , initial fibre orientations are drawn from the prior distribution and other variables are set to their prior means. The burn-in of 500 steps is divided into 3 phases (again, see Section 2.3.2) of 100, 100 and 300 steps, where the proposal variance is adjusted every 10 steps in order to achieve an acceptance rate of approximately 50%. After the burn-in period, the chains are run for 1000 steps, collecting samples every 10th step. Presented segmentations and other results are based on the estimated posterior means computed by averaging the collected samples, with the exception of the cones of uncertainty, which make use of the fibre orientation samples directly. The derived quantities (Section 3.4) are also computed using the posterior means.

As an anatomy reference we use *Radiographic Atlas of Skull and Brain Anatomy* by Massimo Gallucci, Silvia Capoccia and Alessia Catalucci [47].

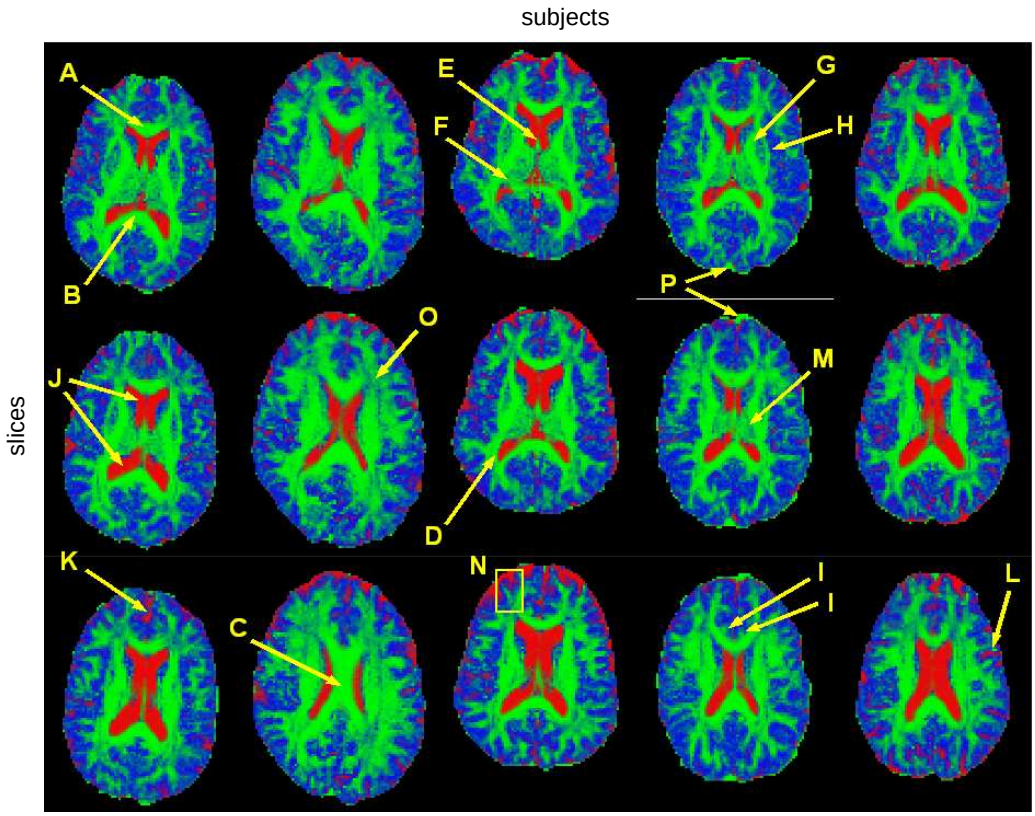

Figure 3.3: Axial slices showing reconstructed tissue maps (mean volume fractions of white matter, grey matter and cerebrospinal fluid). Examples of notable anatomical features: genu (A), splenium (B), body and isthmus (C) of corpus callosum, optic radiations (D), body (E) and crus (F) of fornix, internal (G) and external (H) capsules, cingulate bundles (I), cerebrospinal fluid in the lateral ventricles (J), interhemispheric fissure (K) and other sulci (L), thalamus (M), whole cortical gyrus (N) along with the neighbouring sulci. Crossing fibres (O). See also comments in the text.

3.2 Estimated tissue maps

3.2.1 RGB volume maps

In order to show the estimated inter-voxel volume of the three main tissue types we use whole-brain RGB-coded maps that were first presented in Chapter 2 (spatial phantom segmentations in Figures 2.3–2.5). In this coding the green level corresponds to the volume fraction of white matter, blue stands for grey matter and red for cerebrospinal fluid. Figures 3.3–3.5 show axial, coronal and sagittal cross-sections of five datasets (three slices each); examples of the notable anatomical features are identified in the images with alphabetic labels.

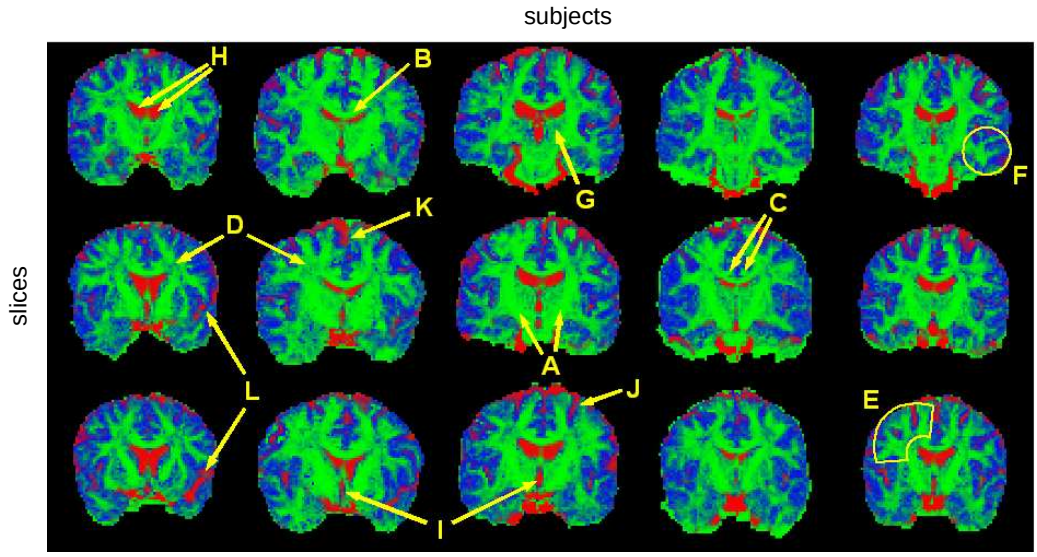

Figure 3.4: Coronal slices showing reconstructed tissue maps (mean volume fractions of white matter, grey matter and cerebrospinal fluid). Notable anatomical features: corticospinal tract (A), body of corpus callosum (B), cingulum bundles (C), corona radiata (D), gyral white matter of the frontal (E) and temporal (F) lobes, thalamus (G), ventricles: lateral (H) and third (I), longitudinal interhemispheric fissure (K), Sylvian fissure (L) and other sulci (J). See also comments in the text.

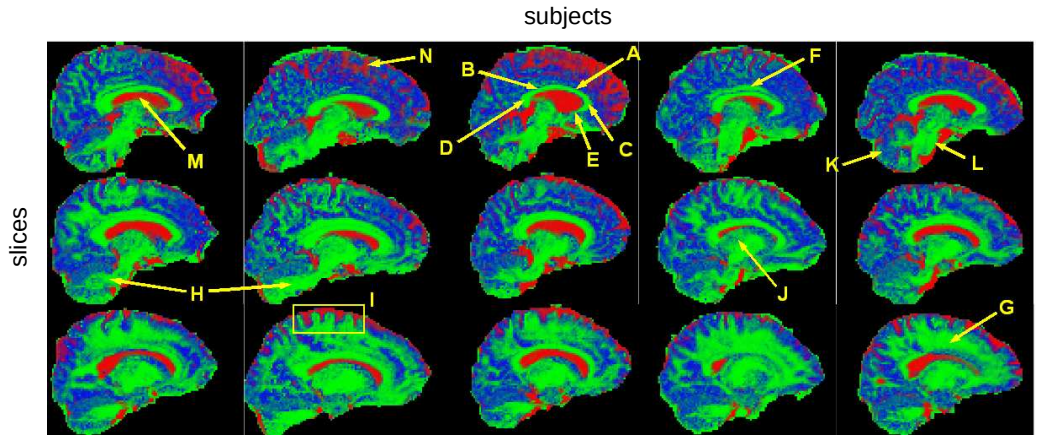

Figure 3.5: Sagittal slices showing reconstructed tissue maps (mean volume fractions of white matter, grey matter and cerebrospinal fluid). Notable anatomical features: body (A), isthmus (B), genu (C), splenium (D) and rostrum (E) of corpus callosum, cingulum bundle (F), corona radiata (G), middle cerebellar peduncle (H), cortical sulci and gyri (I), thalamus (J), cerebellum (K), pons (L), right lateral ventricle (M), cerebrospinal fluid in sulci (N) close to the interhemispheric fissure. Additional comments in the text.

We observe that the major white matter tracts and structures (Figures 3.3/A-I,N, 3.4/A-F, 3.5/A-I) are well delineated, as is cortical and sub-cortical grey matter (3.3/M,N, 3.4/G, 3.5/I-L) and cerebrospinal fluid (3.3/J-L,N, 3.4/H-L, 3.5/I,M,N) in the ventricles, fissures and sulci. In some cases, even strongly partial-volumed structures can be consistently identified, for instance cortical gyri (3.3/N, 3.4/E,F) and sulci (3.4/J, 3.5/N). Thalamus (3.3/M, 3.4/G, 3.5/J) is visible as a mixture of grey and white matter, which is an accurate description of this structure composed of many separate nuclei with distinct input and output fibres.

The only major brain areas that seem to be rendered inaccurately are the regions of crossing fibres (e.g. 3.3/O, 3.4/D), where the white matter volume fraction is lower than expected. This comes as no surprise as our current diffusion model only accommodates one anisotropic component and is thus unable to describe correctly the more complex neural architectures. It is worth noting, however, that the internal capsule (3.3/G) is delineated correctly despite containing fanning fibres from a number of fasciculi. Other artefacts are caused by the inaccurate brain extraction and image acquisition issues, such as magnetic susceptibility and eddy current distortions. These artefacts include the tissue that lies outside the brain, but is not masked out in our dataset, such as the (correctly segmented) water around the brain stem and spurious white matter voxels on the edges (3.3/P).

3.2.2 Greyscale volume maps

Since the RGB coding of tissue type segmentation presented in this work is not standard at present, we have decided to show the greyscale maps of the volume fractions of individual tissue types alongside the new RGB segmentation plots. To this end, Figures 3.6–3.7 have been constructed from the first rows of RGB volume maps in Figures 3.3–3.5. Thanks to the greater clarity of presentation, these images provide an insight into how the estimated volume maps vary across different tissue types.

Cerebrospinal fluid maps (bottom row) tend to comprise crisp white patches on black background indicating that this fluid is only found in a restricted set of spaces and partial voluming occurs only on their borders, which is consistent with known anatomy. The features visible on these maps include cerebral ventricles, main cortical fissures and sulci as well as smaller, heavily partial-volumed sulci. White matter volume maps (top greyscale row) differ from those of the cerebrospinal fluid in that they (appear to) show two classes of fasciculi. Major, thick white matter pathways suffer from little or

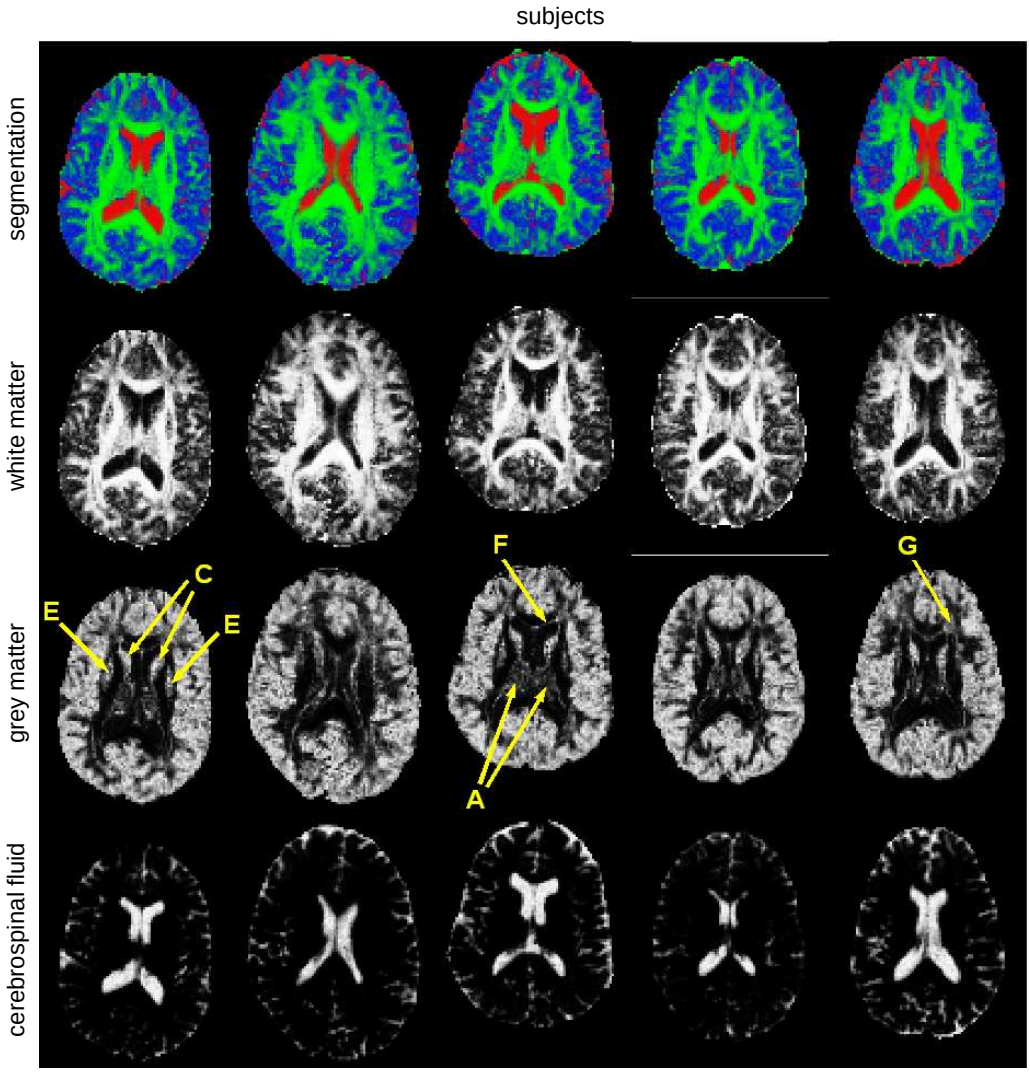

Figure 3.6: Axial slices from five different subjects showing reconstructed, RGB-coded tissue maps as well as grey-scale maps of individual tissues. Notable grey matter structures: thalamus (A), caudate nucleus (C) and putamen (E). Spurious grey matter volume: F and G. Further comments in the text.

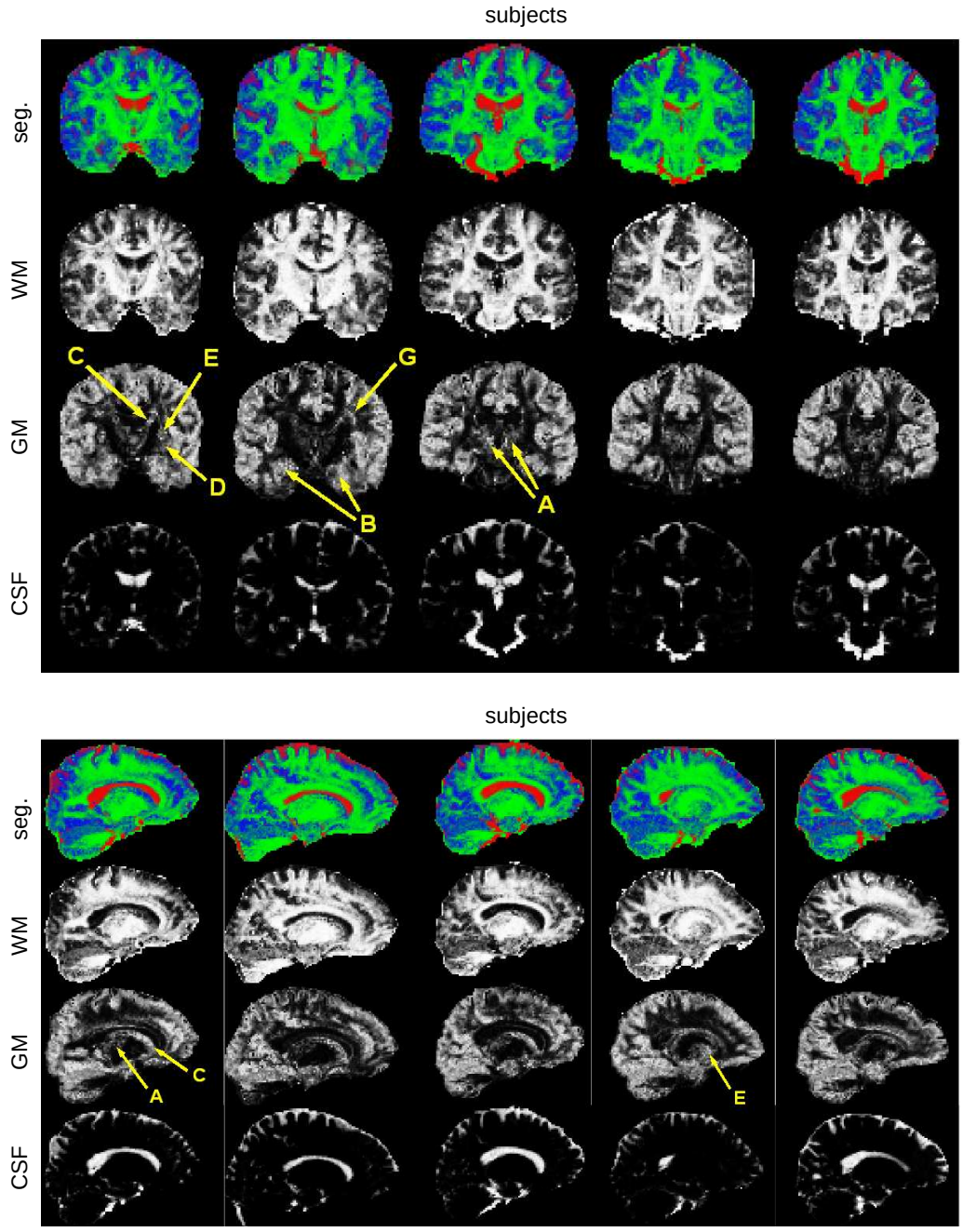

Figure 3.7: Coronal (top) and sagittal (bottom) slices from five different subjects showing reconstructed, RGB-coded tissue maps as well as grey-scale maps of individual tissues. Notable grey matter structures: thalamus (A), hippocampus (B), caudate nucleus (C), globus pallidus (D) and putamen (E). Spurious grey matter volume: G. Further comments in the text.

no partial voluming and are visible in white, while fine white matter strands close to the cortical and sub-cortical targets are usually partial-volumed (less so for larger gyri) and show in grey. Cortical and deep grey matter structure (middle greyscale row) is clearly visible, despite being partial-volumed throughout the brain. Examples include thalamus (A in Figures 3.6–3.7), hippocampus (B), caudate nucleus (C), globus pallidus (D) and putamen (E). The amount of partial voluming is not surprising as the grey matter of the brain forms fine structures such as a thin sheet (cortex), a thin elongated nucleus (hippocampus) or a set of smaller, irregular nuclei (thalamus).

Apart from the correctly segmented grey matter structures, two cases of spurious volumes can be observed. One is a thin border between the lateral ventricles and the corpus callosum (3.6/F): we expect to see only white matter and cerebrospinal fluid in this region, but apparently our model assigns a small portion of the signal to the grey matter compartment which shouldn't be there. Also problematic are the regions of crossing fibres (3.6–3.7/G), where the anisotropy drops as a result of a multi-peak distribution over the orientations and thus a smaller structural coherence. This fact cannot be accommodated by our model, which features only one white matter component, hence there is a spurious rise in the grey matter volume.

3.2.3 Volume maps compared to T_1-based segmentation

Although direct segmentation of the spin-echo EPI volumes is difficult due to low white-grey matter contrast, this can be circumvented by running the segmentation on images with better contrast and higher resolution, for example 3D T_1-weighted volumes. The tissue masks obtained in this way are then registered to the space of the diffusion acquisition. At present, this is a standard method for obtaining whole-brain tissue type-specific averages of quantities of interest, such as measures of the diffusion magnitude and anisotropy.

Figure 3.8 presents white matter masks segmented from 3D T_1-weighted volumes using FAST [122] (a segmentation tool from the FSL) along with the maps of white matter volume fraction estimated with the tissue dependent diffusion model. We observe that the former correctly flags the crossing fibre regions (3.8/A) as pure white matter, thus improving on the performance of our method. On the other hand, chunks of important fasciculi clearly visible in white matter volume fraction maps are missing from the segmentation based on the T_1-weighted volumes altogether, for example the corpus callosum (3.8/B). When trying to explain the mismatch between the two

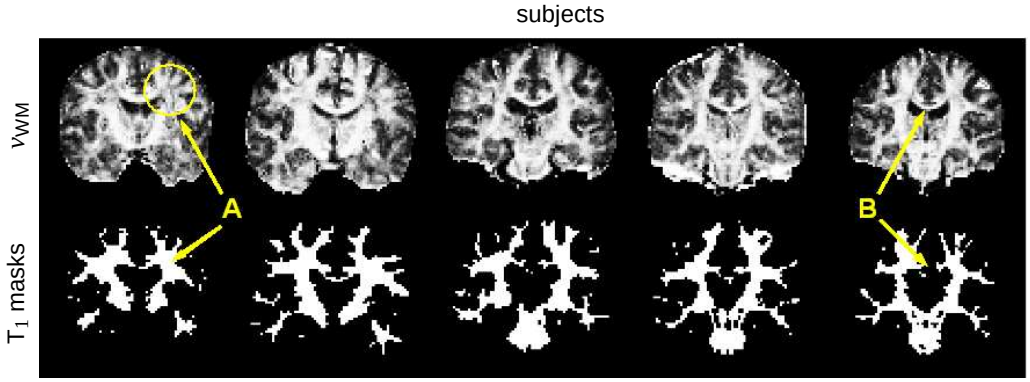

Figure 3.8: Coronal slices from five different subjects showing reconstructed grey-scale maps of white matter volume fraction (top row) and T_1-based white matter masks obtained with FAST (bottom). The latter perform consistently better in crossing fibres regions (A), but occasionally miss chunks of important, major pathways, for example corpus callosum (B).

segmentations, it has to be noted that whereas our method supplies real valued volume fraction maps which describe partial voluming, the masks segmented from the T_1-weighted images are binarised and indicate categorical classification of all voxels. Such binarisation is a common procedure when using high resolution segmentation results in diffusion studies. While making minor white matter tracts invisible due to the partial volume effects, it can improve results in areas which belong clearly to white matter, even if for some reason their overall anisotropy is below average. Unfortunately, registration of the high resolution tissue type masks might result in gaps appearing in the thin sections of the white matter pathways, as Figure 3.8 illustrates. Additionally, it is difficult to judge whether the diffusion MRI data and the T_1 masks are aligned well after the registration.

3.3 Estimated fibre orientations

Volume estimation, presented in the previous section, can provide a basis for the segmentation of the entire fasciculi and the computation of their total volume. The integration of data from single voxels requires that the local orientation of white matter fibres is also available. This type of information has been successfully extracted using both deterministic [9] and probabilistic [16, 15, 45, 55, 56] methods. In this section we evaluate the anatomic plausibility of the orientations estimated with our method, com-

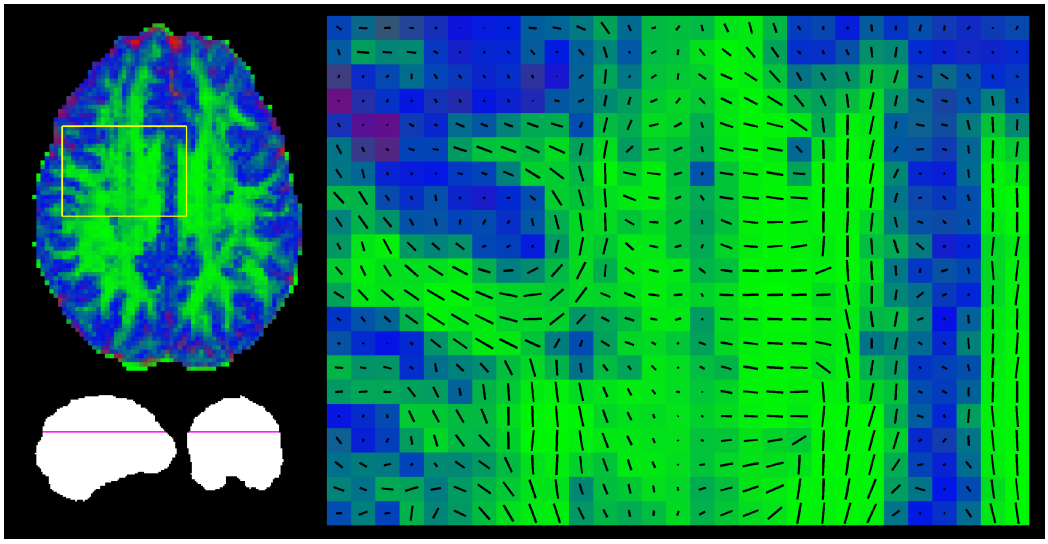

Figure 3.9: Axial slice through centrum semiovale featuring short and long association, commissural and projection fibres. Estimated fibre orientations are overlaid as black bars projected onto the image plane and scaled according to the white matter volume fraction. Both the tissue segmentation and the orientation of the fibres agree with known brain anatomy.

pare them with the results of well established approaches and examine their posterior variance.

Figures 3.9–3.11 present the mean estimated orientations of white matter fibres overlaid on the RGB-coded maps of the tissue volume. These orientations seem to align well with the major tracts we expect to find within each ROI as detailed in the figure captions. In the regions where fibres from different pathways cross the estimated volume fraction of white matter drops slightly and the estimated orientation seems to be that of the fasciculus dominant in a given voxel. This effect is clearly visible for example in Figure 3.9, where the white matter in the centre of the ROI is expected to show in bright green indicating that no other tissue type is present. Instead, some voxels appear to contain a fraction of grey matter (shown in blue). The estimated fibre orientations in these voxels can nevertheless be identified as belonging to one of the main pathway families present (association, commissural, projection). There is therefore no obvious orientation averaging, despite the fact that such an effect has been demonstrated in the case of diffusion tensor model [43]. The fanning architectures seem to be rendered correctly, at least in large structures such as the internal capsule shown in Figure 3.10 (left). It contains ascending fibres[1] that fan from the base of the brain

[1]Descending fibres travelling in the opposite direction are also present. The two families are indis-

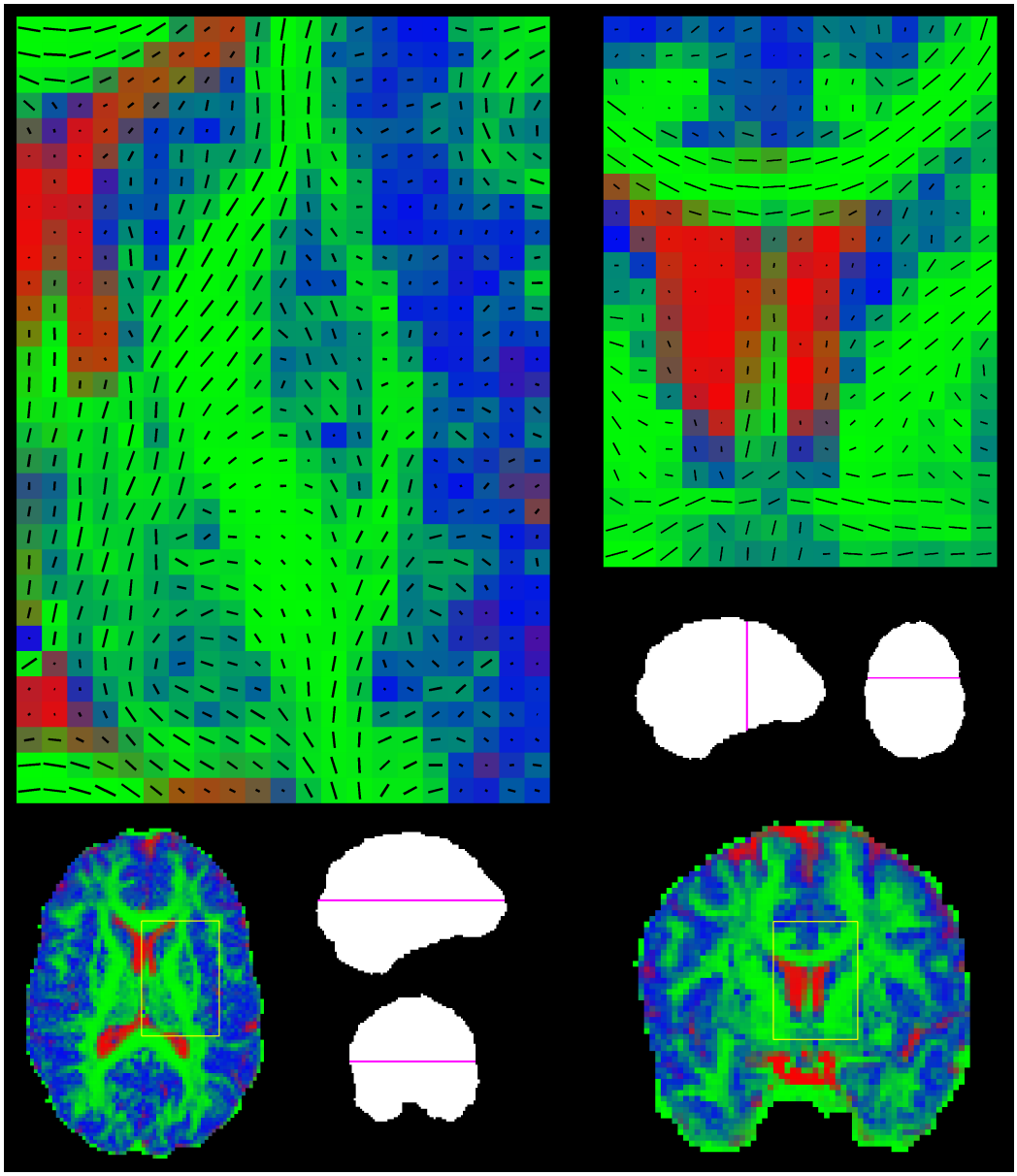

Figure 3.10: Left: Axial slice showing internal capsule (external capsule and corpus callosum also visible). Right: Coronal slice showing anterior commissure (also visible are portions of internal capsule, corpus callosum, cingulum bundles and column of fornix). Estimated fibre orientations are overlaid as black bars projected onto the image plane and scaled according to the white matter volume fraction. Both the tissue segmentation and the orientation of the fibres agree with known brain anatomy.

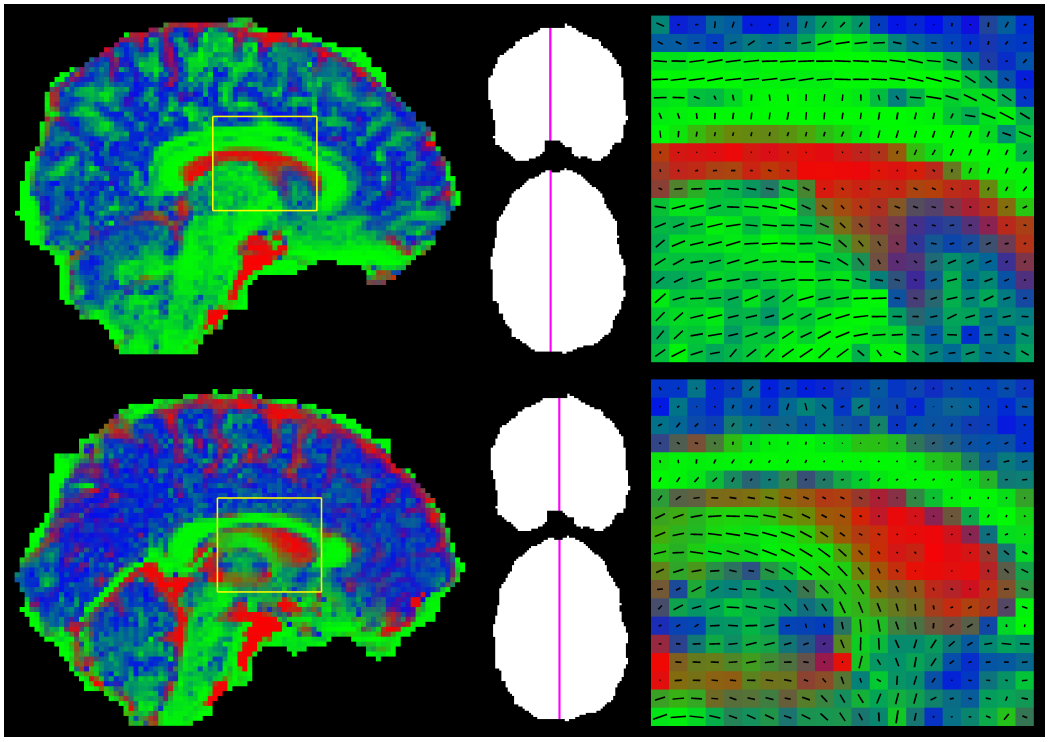

Figure 3.11: Top: Cingulum bundle and corpus callosum. Bottom: Corpus callosum and fornix. Estimated fibre orientations are overlaid as black bars projected onto the image plane and scaled according to the white matter volume fraction. Both the tissue segmentation and the orientation of the fibres agree with known brain anatomy.

to reach their cortical targets in the frontal, parietal and occipital lobes. In particular, the anterior limb and genu of the internal capsule contain fibres projecting anteriorly, while fibres projecting vertically up and posteriorly can be found in the posterior limb. This divergence can readily be seen in Figure 3.10 (left). In conclusion, we find that fibre orientations estimated with our method match those predicted by the anatomy as well as is possible within a single fibre paradigm. In fact, our results align well both with the principal orientations from the diffusion tensor model (Figure 3.12) and the orientations of the dominant component from the two-fibre ball-and-stick model (Figure 3.13, obtained with `bedpostx`).

The variance of the estimated posterior distribution over the fibre orientations can be visualised using the cones of uncertainty [61]. It is worth stressing that the posterior variance is influenced both by the uncertainty about the true mean orientation and by the true distribution of fibres within a given voxel, which need not be all parallel. In Figure 3.14 we present a variant of the cones of uncertainty such that they contain 95% of the fibre orientation samples, thus approximating 95th percentile of the posterior distribution. The cones are also scaled according to the volume fraction of the white matter. Examining Figure 3.14 we note that pure white matter voxels generally show low posterior variance, apart from the crossing fibre regions, where as expected it can be very high. The variance is apparently not greatly affected by the partial voluming from the cerebrospinal fluid or the grey matter (the latter only if a dominant orientation is present). In areas of complex grey-white matter architecture the posterior variance of the fibre orientation tends to be high.

3.4 Diffusion measures and noise

3.4.1 Measures of anisotropy and diffusivity

In this section we move away from the tract segmentation problem and consider parameters of interest other than white matter volume and fibre orientations necessary for tractography. When examining the health of the brain's white matter pathways it is often of interest to consider the shape of the diffusion profile (see discussion in Section 4.1.2). Specifically, it is useful to examine two coefficients: axial diffusivity (AD), along the fibre direction, and radial diffusivity (RD), in the transverse plane[2].

tinguishable with current imaging methods.

[2] In tissue dependent diffusion model RD is denoted as $d_\perp$ and AD can be expressed as $d_\perp + d_\Delta$.

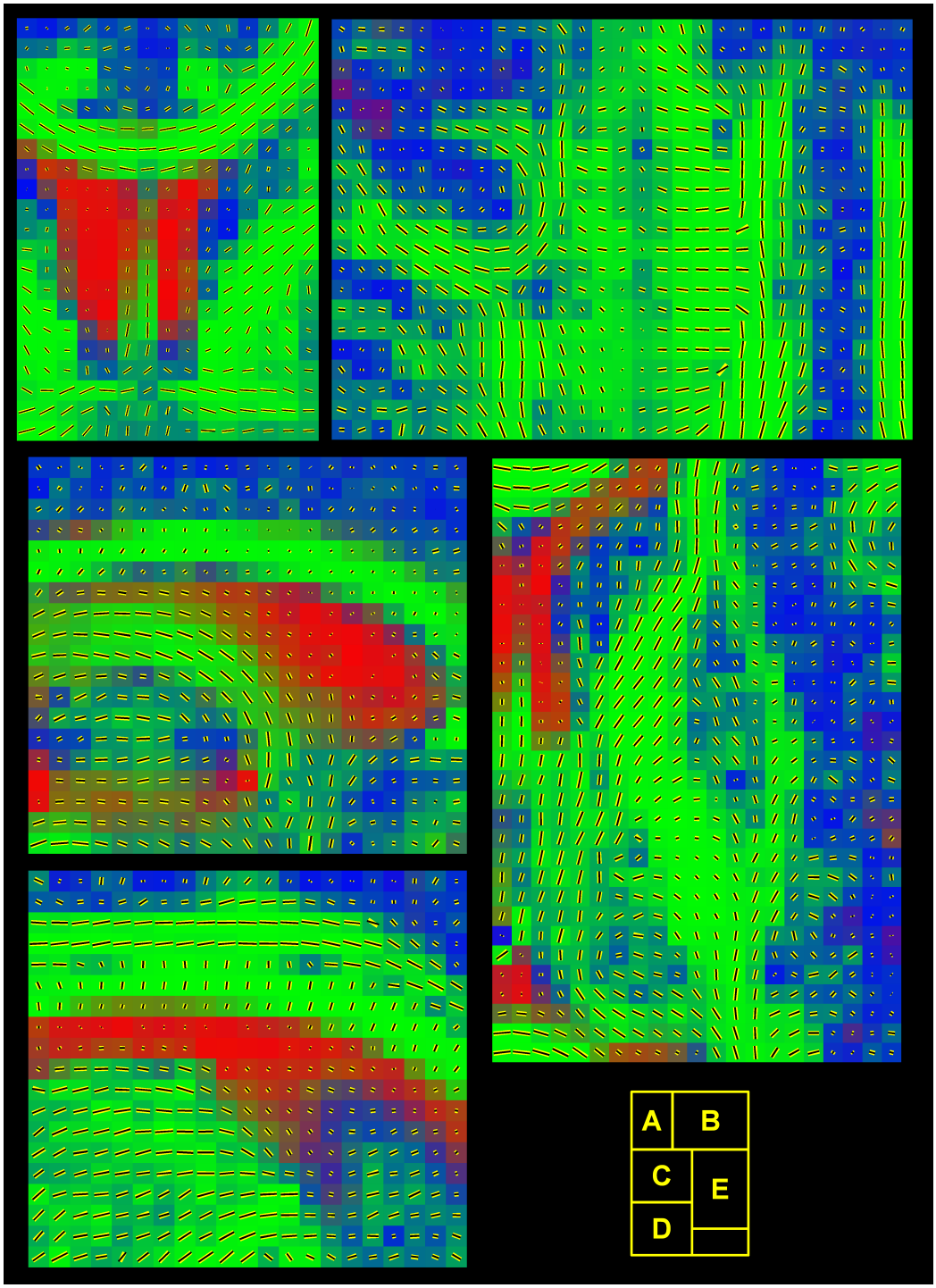

Figure 3.12: Comparison of the fibre orientations estimated with our method (black bars) with principal orientations of the diffusion tensor (thick yellow bars). Regions of interest are identical to those in previous figures: (A) anterior commissure presented in Fig. 3.10, (B) centrum semiovale from Fig. 3.9, (C) corpus callosum and fornix from Fig. 3.11, (D) cingulum bundle and corpus callosum from Fig. 3.11 and (D) internal capsule from Fig. 3.10.

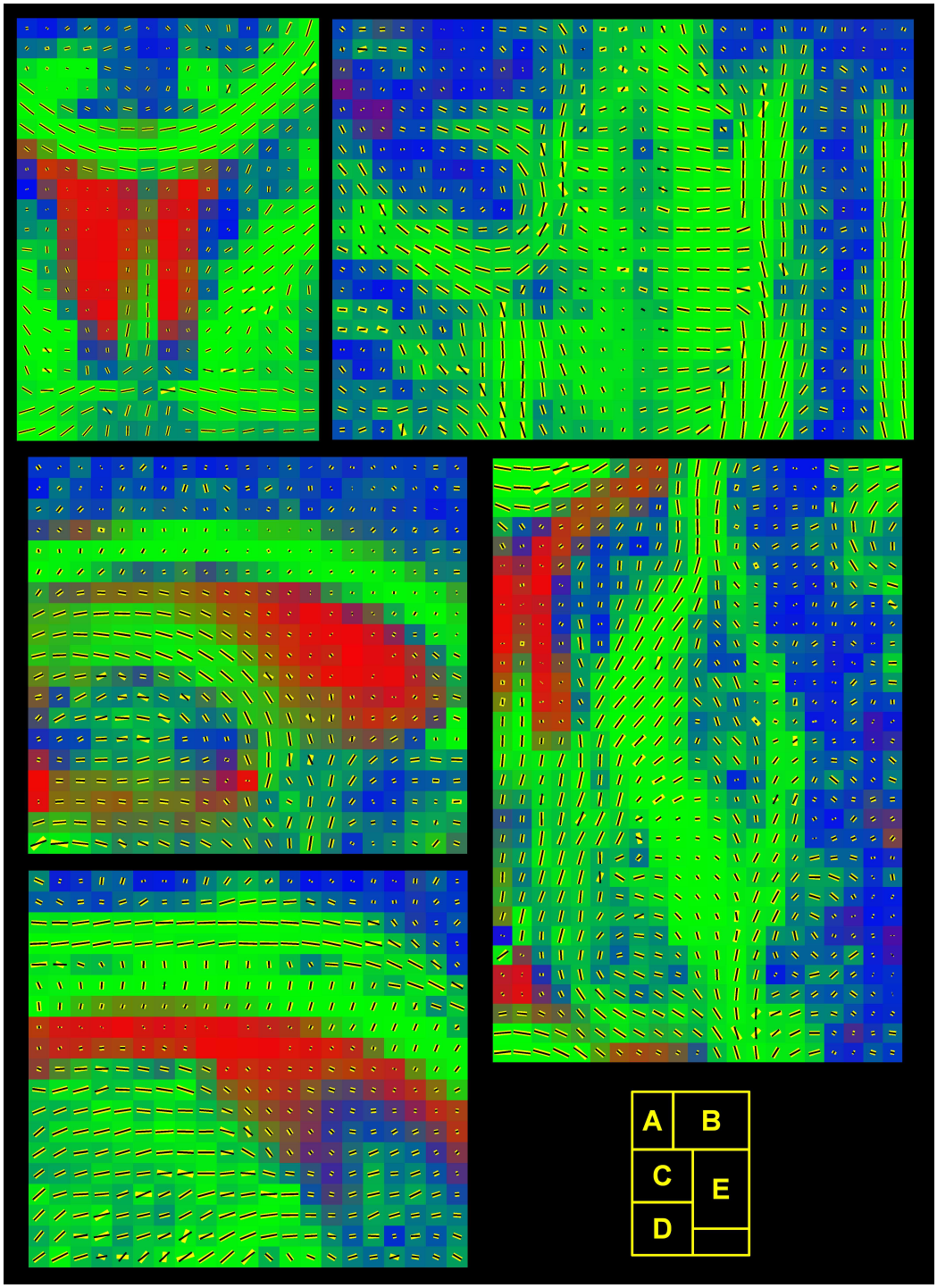

Figure 3.13: Comparison of the fibre orientations estimated with our method (black bars) with dominant fibre orientations of the ball-and-stick model (thick yellow bars). Regions of interest are identical to those in previous figures: (A) anterior commissure presented in Fig. 3.10, (B) centrum semiovale from Fig. 3.9, (C) corpus callosum and fornix from Fig. 3.11, (D) cingulum bundle and corpus callosum from Fig. 3.11 and (D) internal capsule from Fig. 3.10.

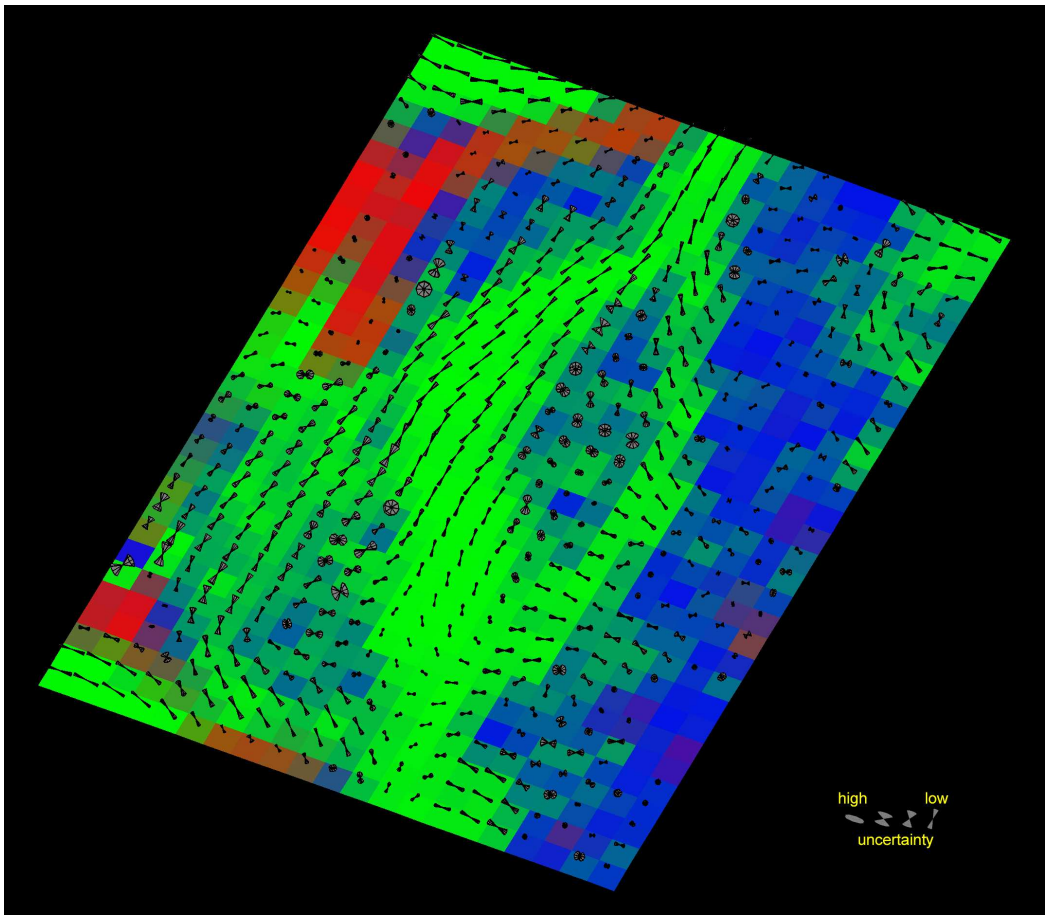

Figure 3.14: Cones of uncertainty of fibre orientation. The cones enclose 95% of the samples from the posterior distribution. Leftmost cone in the bottom right panel corresponds to the uniform distribution. ROI featuring internal capsule is identical to the one shown in Figure 3.10.

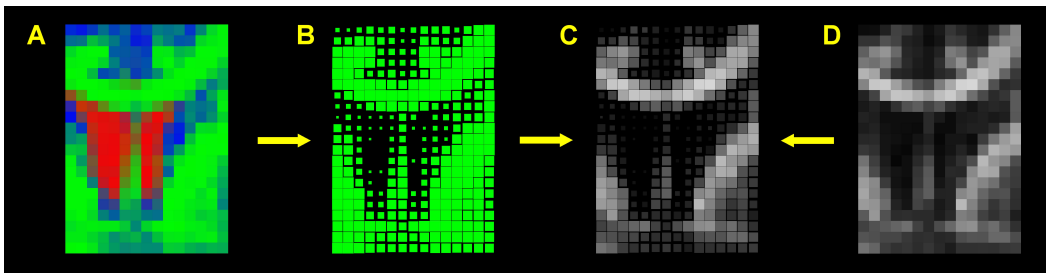

Figure 3.15: The creation of a volume-scaled map: FA map scaled according to the white matter volume (C). Steps: (A) RGB-coded segmentation map; (B) white matter volume fraction map, coded by square size instead of colour; (D) standard FA map.

Other notable measures describing water diffusion are its overall magnitude and the degree of anisotropy. As discussed in Chapter 1, these two tissue characteristics have most commonly been quantified using FA and MD (see page 16). All four of the above quantities, while providing informative description of pure tissue voxels, are negatively affected by partial voluming when computed using the traditional diffusion tensor model. Since in our work the isotropic partial volumes are modelled directly, we can look at the equivalents of FA as well as RD, AD and MD based specifically on the tensor describing the white matter compartment from the tissue dependent diffusion model we propose. We shall refer to these quantities using the suffix 'fibre', e.g. fibre FA.

We are now going to examine the relationship between the two sets of measures characterising water diffusion in white matter, particularly in the context of partial voluming. This kind of investigation requires that we consider both the values of the quantities being investigated and the amount of partial voluming. To this end, we propose the use of volume-scaled maps that augment intensity images with volume information thus enabling us to intuitively relate the two. The process of creating a volume-scaled map is illustrated in Figure 3.15. First of all, a single tissue volume fraction map is extracted from an RGB coded map (3.15/A) and the pixels of this 2D image are scaled according to the volume fraction (3.15/B). This way the volume information is coded by the pixel (square) size and the intensity can be used to show another quantity. In our example, colouring the scaled squares according to the values of FA (3.15/D) in the respective voxels yields the final result: a white matter volume-scaled map of FA (3.15/C). This type of map allows the examination of tissue type specific quantities where they are relevant, namely in voxels containing the tissue.

The reliability of the volume-scaled maps depends heavily on the underlying vol-

ume maps. In particular, in voxels where the volume estimates are spuriously very low, the intensity map will not be visible even if it is potentially of interest. In other words, an erroneous volume map could result in falsely negative observations. The examination of volume maps obtained with our method (see Section 3.2) shows that this is not the case here. It is also worth keeping in mind that the volume-scaled maps are not meant to create a dithering effect — we are not using variable size dots to create an impression of intensity changing over a region of the image. On the contrary, each and every square of the image is meaningful as regards both its size and colour.

Figures 3.16 and 3.17 present four white matter volume-scaled maps of the same axial slice. The quantities in the left column have been computed from the white matter tensor from the tissue dependent diffusion model, while the corresponding measures in the right column are based on the traditional diffusion tensor model. Figure 3.16 shows diffusivity coefficients: RD (top row) and AD (bottom row). Maps have been normalised in rows so that equal intensities correspond to equal values. They show similar intensity in pure white matter voxels forming major pathways, such as corpus callosum or internal capsule. At the same time, we observe elevated RD (top right map) in partial volumed voxels, particularly in the areas where white matter is bordering cerebrospinal fluid. This result is explained by the fact that the MD in both grey matter and cerebrospinal fluid is larger than the typical RD of healthy white matter (see Table 2.1 on page 45). Significant amount of partial voluming from any of these tissues (particularly from cerebrospinal fluid) will thus result in the overestimation of RD. This phenomenon is still visible, albeit greatly ameliorated, in the fibre RD map (top left). A more subtle effect can be observed in the AD map. Here, we expect partial voluming from cerebrospinal fluid to increase the diffusion tensor estimate of this quantity. In voxels where grey matter is present, however, AD should appear smaller than it otherwise would. This is because the typical AD of healthy white matter (see Table 2.1 on page 45) is greater than MD of grey matter, but lower than that of cerebrospinal fluid. Taking into account the partial volume effects described above, we expect the underlying, true AD of white matter to be similar to the fibre AD maps. In other words, we argue that fibre-specific quantities we estimate are closer to the underlying anatomy, because they are similar to the values we would arrive at by taking the diffusion tensor estimates and conceptually reversing the effects of partial voluming.

The differences between the estimates of diffusivity coefficients from the diffusion tensor and tissue dependent diffusion models are reflected in the metrics summarising the shape and size of the diffusion profile. The top row of Figure 3.17 features white

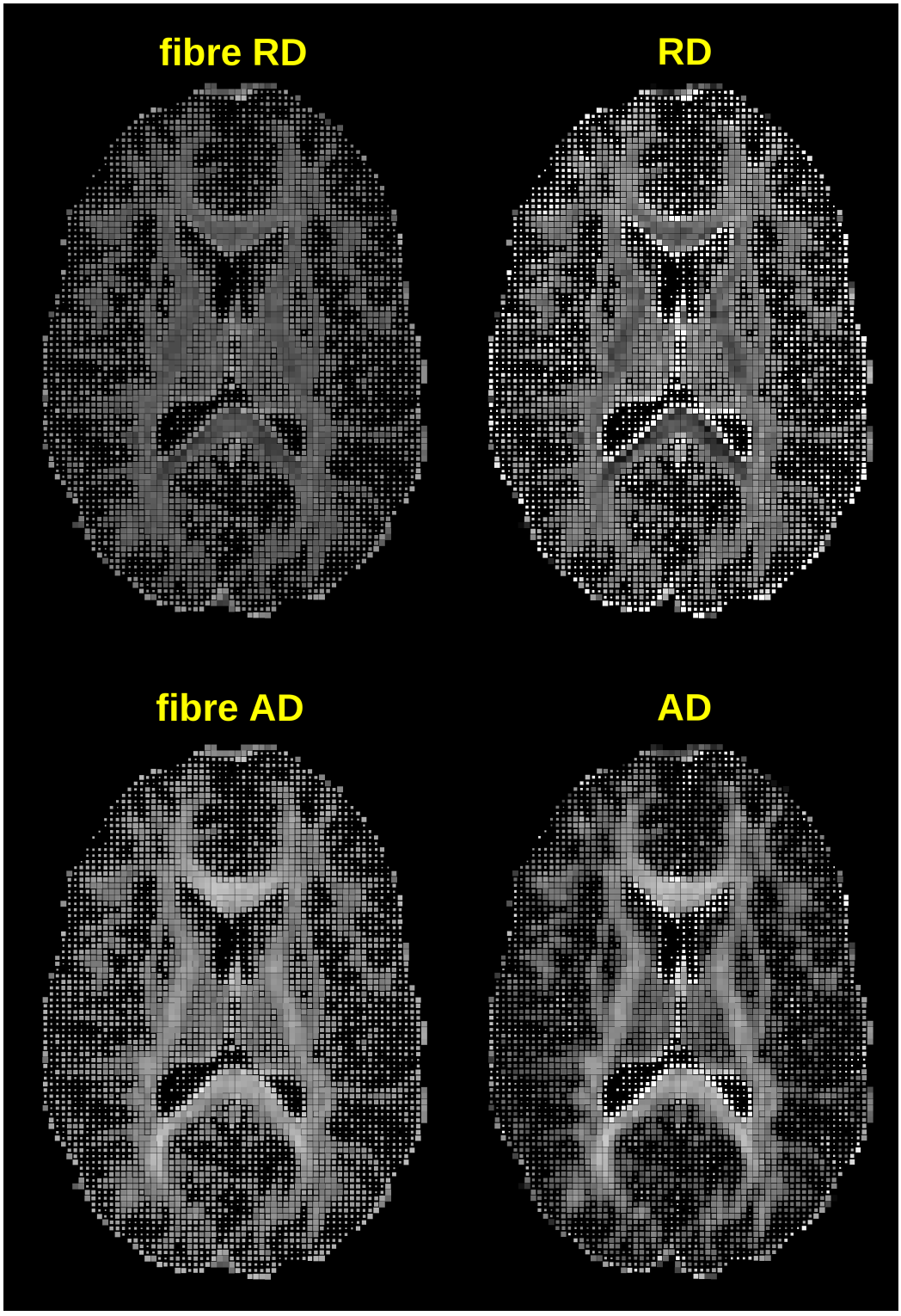

Figure 3.16: Radial (RD) and axial diffusivity (AD) computed on the basis of entire voxels using the diffusion tensor model (right column) compared to their analogues for the white matter compartment from the tissue dependent diffusion model (left column). The fibre-specific maps seem to show smaller corruption due to partial voluming, both from grey matter and from cerebrospinal fluid (see text).

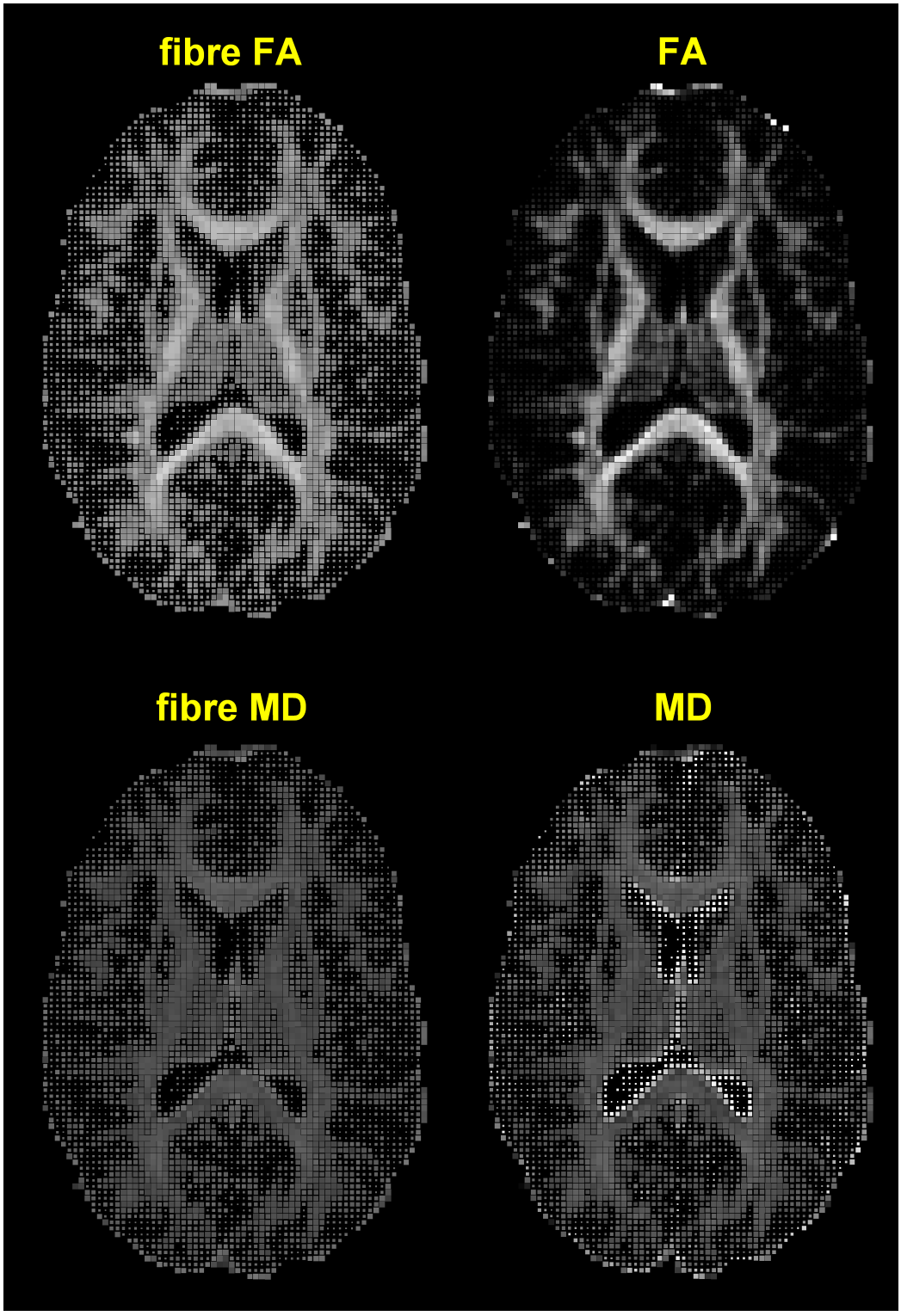

Figure 3.17: Fractional anisotropy (FA) and mean diffusivity (MD) computed on the basis of entire voxels using the diffusion tensor model (right column) compared to their analogues for the white matter compartment from the tissue dependent diffusion model (left column). The fibre-specific maps show smaller corruption due to partial voluming, which causes the FA to spuriously drop and MD to raise (on the right).

matter volume-scaled maps of FA computed from the anisotropic component of the tissue dependent diffusion model (left) and from the standard diffusion tensor model (right). The bottom row, analogously, presents MD. We observe that voxels with partial voluming show a significant drop in FA, but not in fibre FA (though some darkening is still visible around the edges of the fasciculi). Anisotropy within pure white matter voxels in major pathways has similar features in both maps (e.g. particularly high values for the splenium). We argue that fibre FA provides a smoother, more plausible distribution of anisotropy values regardless of the white matter volume fraction. Similar, if not more pronounced effects can be observed in the MD maps. The diffusion tensor-derived MD index appears dramatically elevated in voxels with partial volumes of cerebrospinal fluid. This effect is also visible, but greatly alleviated in the fibre MD maps. Partial volumes of grey matter do not appear to affect this metric as typically this tissue type has MD similar to that of the white matter.

These qualitative observations are confirmed when comparing the fibre-specific and diffusion tensor-based summary statistics directly. A scatter plot in Figure 3.18 presents a sample of voxels from one dataset coloured according to their white matter content. We observe that the values of FA vary across its entire legitimate range (0,1), dropping particularly low for partial volume voxels. By contrast, the values of fibre FA are concentrated around and above 0.5 and do not show a marked decrease as the fraction of white matter (and FA) goes down. In general, fibre FA values tend to be larger than FA, with approximately linear dependence in the high anisotropy region. As far as the magnitude of diffusion is concerned, MD and fibre MD show a very close, linear correspondence for pure white matter voxels (see Figure 3.19). With partial voluming, however, MD spans the range between the values typical for white (and grey) matter and those of cerebrospinal fluid, whereas fibre MD stays firmly within the typical white (and grey) matter range. To summarise, the fibre-specific quantities derived from the tissue dependent diffusion model (fibre FA and MD) seem to alleviate the effects of partial voluming, which makes FA spuriously low and MD spuriously high.

3.4.2 Estimated noise level

The final part of this chapter looks at the noise level for the Rice distribution, ς. Whole-brain histograms of the mean estimated ς are presented in Figure 3.20. This parameter's prior distribution is a Gamma *pdf* with mean at 200 and standard deviation of

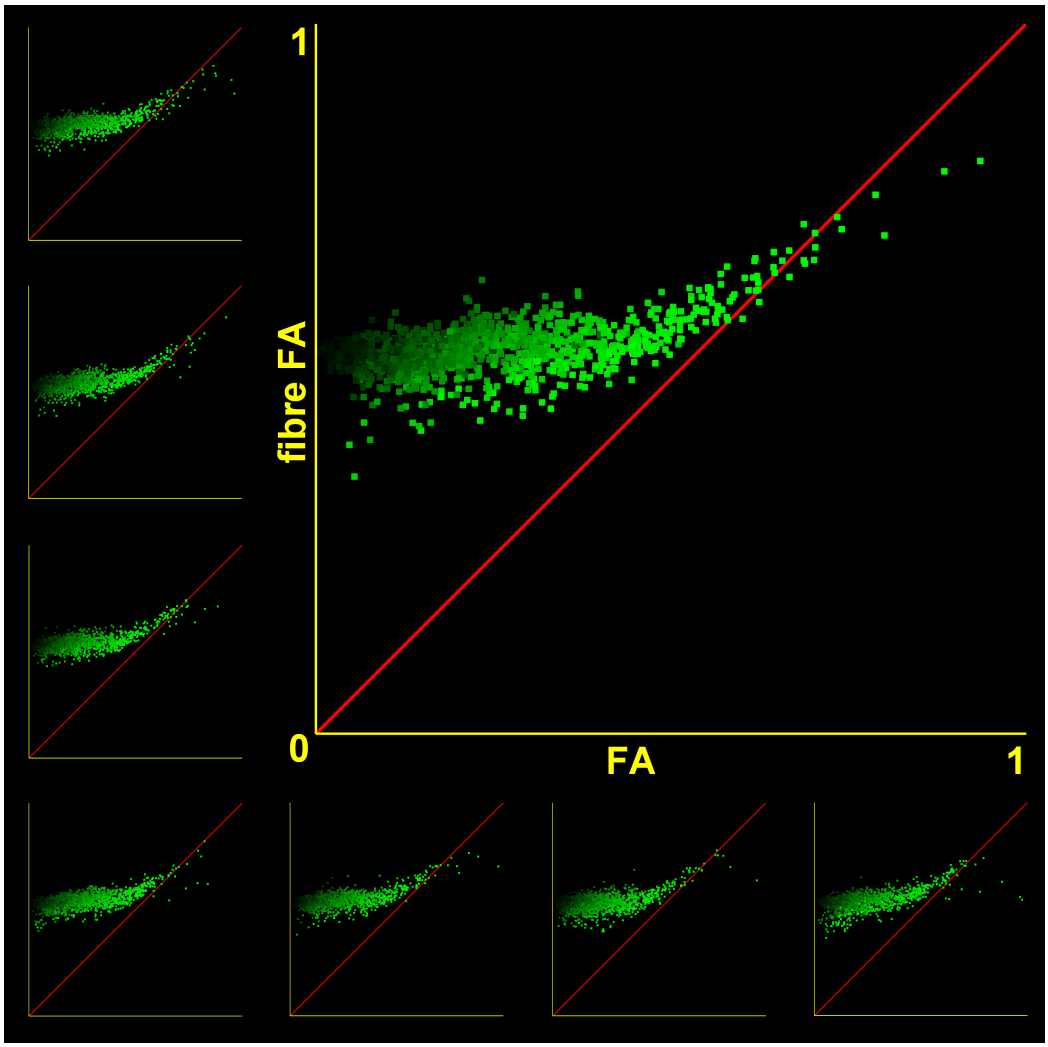

Figure 3.18: Fractional anisotropy (FA) compared to fibre FA. The squares are shaded according to the white matter volume fraction, where bright green corresponds to 1 and black to 0. Smaller scatter plots show the results for different subjects.

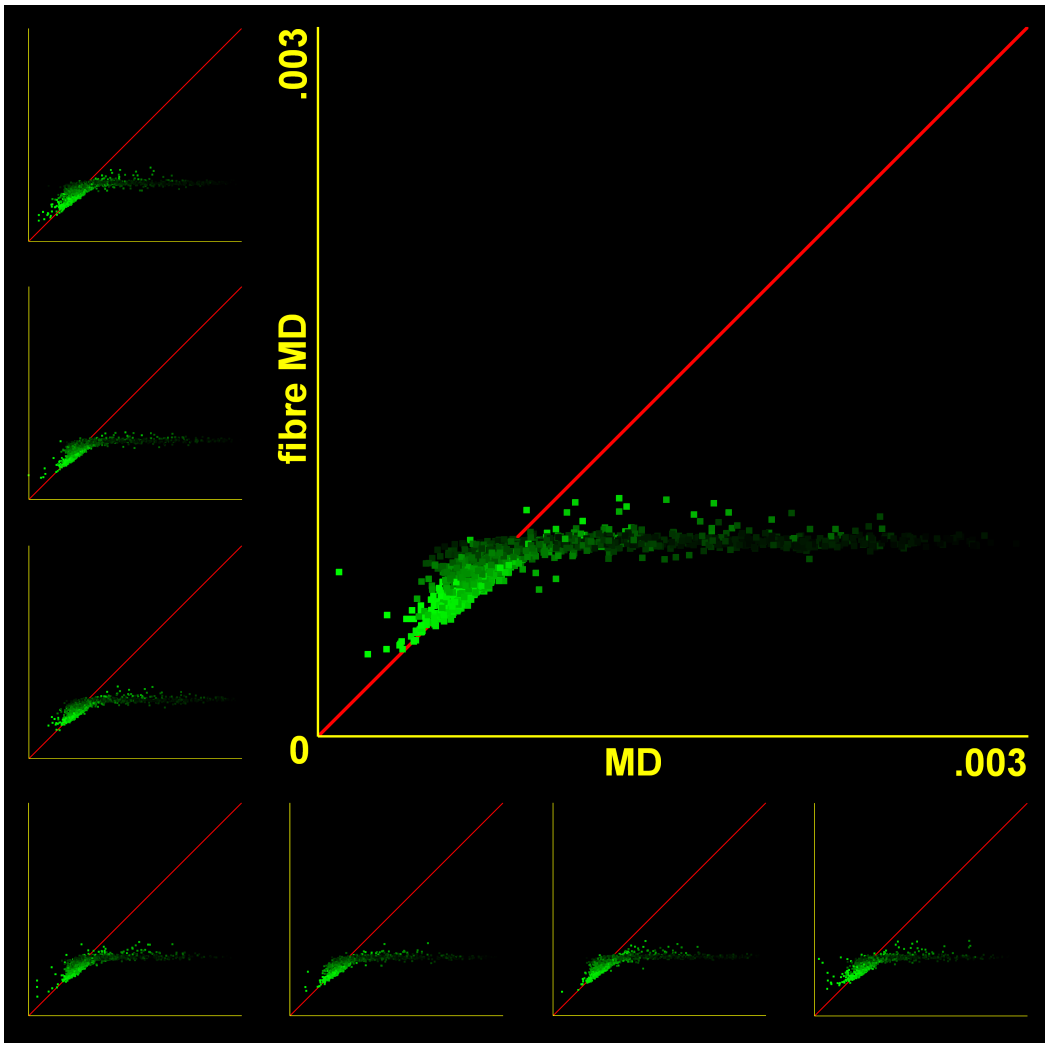

Figure 3.19: Mean diffusivity (MD) compared to fibre MD. Units are mm^2/s. The squares are shaded according to the white matter volume fraction. Smaller scatter plots show the results for different subjects.

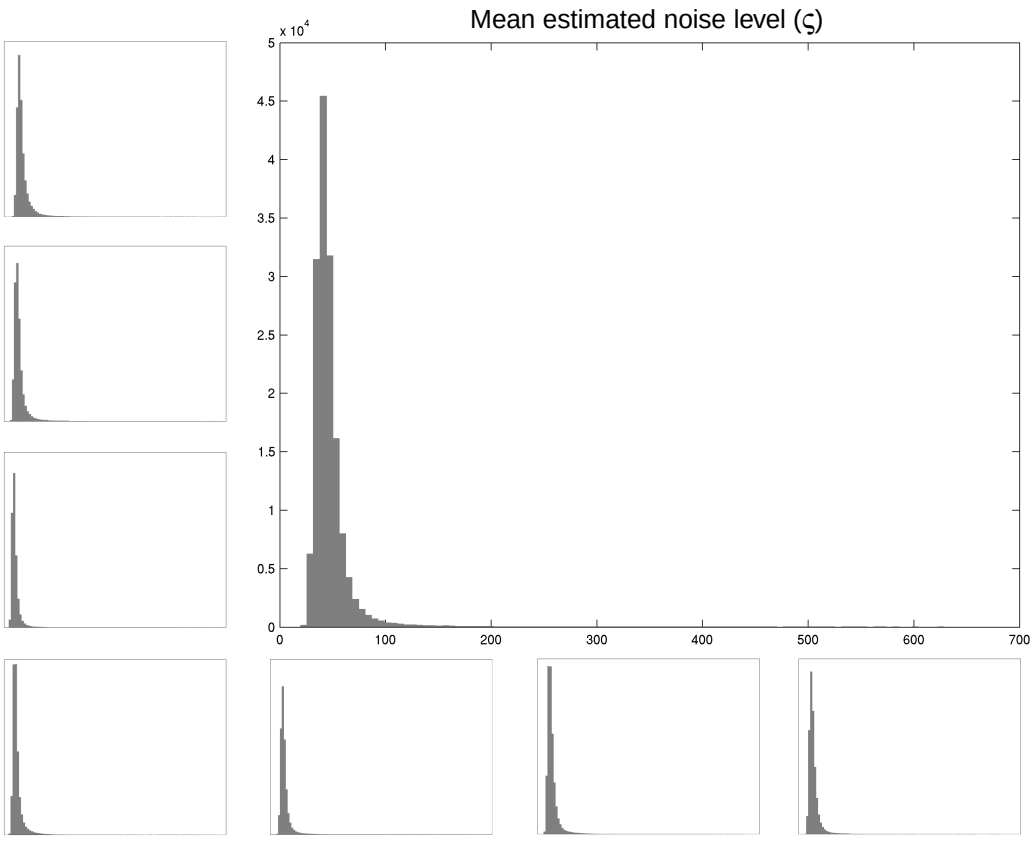

Figure 3.20: Whole brain histogram of the (mean posterior) noise level (ς) for the Rice distribution. Smaller histograms show the results for different subjects.

approximately 140. We observe that for the vast majority of the voxels the estimated noise level is in the low region of the prior, with the bulk of values below 100 and a peak around 50. This is equivalent to a signal-to-noise ratio ranging from 3 to 50 for pure cerebrospinal fluid voxels, from 8 to 24 for grey matter and from 6 to 13 for white matter (lower values are for the diffusion-weighted measurements where the signal is smaller, whereas higher values are for the T_2-weighted measurements). At the same time, the noise level histograms show a long, thin tail extending typically up to 700. High noise estimates are recorded in voxels prone to the magnetic susceptibility artefacts, mainly near sinuses and around the brainstem.

3.5 Conclusions

This chapter examined the results obtained with the tissue dependent diffusion model, developed in Chapter 2, on data obtained from a small number of human volunteers. We demonstrated that brain tissue segmentations feature a number of plausible white

and grey matter structures as well as cerebrospinal fluid-filled spaces. Fibre orientations seem to align well with the major axonal pathways, within the limits of the single fibre approximation. As always within the single-fibre framework, caution is needed when looking at areas of crossing fibres. We also examined the estimates of white matter diffusivity across and along the fibre direction, as well as summary measures of the magnitude and anisotropy of water diffusion. Compared to the fibre-specific analogues of these quantities, the estimates from the diffusion tensor model show systematic differences akin to the expected effects of partial voluming from grey matter and cerebrospinal fluid. This indicates that the measures based on the tissue dependent diffusion model provide a more accurate description of the true white matter characteristics.

Chapter 4

Studying the ageing brain

Chapter 2 investigated the reliability of the tissue dependent diffusion model on synthetic datasets. The results obtained by running the method on the human brain have been visualised as maps and examined in detail in Chapter 3. We now look at a group of healthy subjects spanning 40 years of age, from 25 to 65 years, to assess white matter volume and diffusivity properties at different stages of normal, healthy ageing, albeit before significant changes are thought to occur.

The notion that white matter degeneration, or lesions, can lead to the loss of function as severe as that caused by cortical dysfunction is often referred to as the *disconnection hypothesis* [30, 42]. Its origins can be traced back to the influential paper by Geschwind [48, 49], which presented a number of earlier findings about white matter lesions in animal and human subjects along with the associated symptoms, such as impediments affecting language ability (aphasias), voluntary learned movement (aphraxias), and interpretation and recognition of perceptual information, objects and people (agnosias). It is conceivable that the cognitive decline in normal, healthy ageing is also mediated by the gradual loss of connectivity. Indeed, several consistent patterns of age-related change in the white matter diffusion properties have been found [26, 17] and linked to possible changes in the underlying neural substrate. The connection between these patterns, measured with diffusion MRI, and cognitive performance is now under extensive study (see [74] for an exhaustive review).

4.1 White matter degeneration and diffusion

4.1.1 Mechanisms of microstructural degeneration

Age-related degeneration of neural tissue is not driven by a single underlying physiological process, nor is it spatially homogeneous. To the contrary, several different mechanisms are thought to be at play and there is some evidence that their occurrence and severity display a level of spatial specificity. In general, two distinct sources of pathology can be identified: degeneration of neurons and glia, particularly oligodendrocytes; vascular failure leading to ischæmic lesions that trigger secondary (Wallerian) degeneration of neurons.

Post-mortem stereologic studies of neural tissue from healthy young and ageing subjects indicate that a portion of axons, particularly those with small diameters, is lost with age [111, 77] while other neurons degenerate and swell. Oligodendrocytes increase in number and myelin degenerates by forming atypical structures not found in young individuals. Glial cells are also heavily affected, accumulating cellular debris and changing their morphology [91]. As a result of these processes, extracellular volume fraction grows and axonal spacing increases. This, together with lowered membrane density and extracellular tortuosity, means that fewer obstacles to water diffusion are present. It is worth noting that, while demyelination can be accompanied by axonal loss, it is not always the case.

In addition to the intrinsic and possibly co-occurring axonal and myelin degeneration, healthy ageing is also characterised by local ischæmic white matter lesions [40, 117]. These lesions can lead to the loss of neurons as well, but the associated physiological processes and symptoms (in terms of the diffusion properties) are different from those of other age-related changes. Affected cells break down and undergo secondary (Wallerian) degeneration. Axons distal from the lesion site are infiltrated by glia, which impede longitudinal diffusion. No myelin breakdown takes place until days after the ischæmia, hence overall diffusivity initially drops before a final increase following demyelination [101, 110, 109].

4.1.2 Diffusivity measures of white matter decline

Many studies in the diffusion tensor imaging (DTI) literature look at FA and MD as indices of white matter well-being, where a decrease of the former accompanied by an increase of the latter is treated as a sign of pathology. Indeed, this pattern of change

is consistent with the axonal and myelin pathology described above and has been reported repeatedly in healthy ageing population, for example in corpus callosum and centrum semiovale [93, 92, 105]. While the two summary metrics (FA and MD) are jointly sufficient to fully determine the diffusion profile, it has been suggested that examining AD[1], diffusivity along the fibre direction, and RD[2], diffusivity in the transverse plane can help differentially link the diffusion MRI data to the underlying biological processes. In particular, increases in RD have been linked to demyelination in mouse models [102], whereas AD is thought to be related to the abundance and health of the axons. A rise in AD would indicate axonal loss, where cellular debris is cleared by astrocytes forming glial scars, inter-axonal spacing increases and barriers to axial diffusion are removed. A drop in AD, on the other hand, has been connected to the secondary (Wallerian-like) degeneration following distal lesions to the neuron, and involving gilal infiltration of axons, which impedes diffusion to a greater degree [101, 110, 109]. RD and AD thus promise to act as markers specific to different microbiological mechanisms of degeneration.

It has to be noted that the interpretation of the diffusivity coefficients outlined above is not entirely uncontroversial. Recent work on multiple sclerosis, a disease characterised by chronic white matter lesions, suggests that myelin content and axonal count are correlated [96, 69]. The authors also suggest that RD (in *ex vivo* human spinal cord from multiple sclerosis sufferers) is related to both types of pathology (axons and myelin) and thus can be treated as a general marker of tissue integrity, not specific to demyelination [69].

Apart from the specificity issues the main challenge to using RD and AD is their correct estimation. For example, in areas of complex fibre architectures, such as crossing, bending or fanning fibres neither AD nor RD can be computed correctly due to the averaging of the signal coming from different fibre families or segments; this has been recently demonstrated by Wheeler-Kingshott et al. [120], who looked at crossing fibres in simulated datasets, as well as healthy subjects and multiple sclerosis sufferers. Similar problems are encountered in voxels where partial voluming from isotropic tissues occurs. A recent study using synthetic data with a range of phantom geometries has shown that both isotropic and anisotropic partial voluming affects the estimation of commonly used diffusivity parameters [118]. The authors also show that anisotropy and diffusivity measures in (segments of) corpus callosum and cingulum bundles cor-

[1] In the tissue dependent diffusion model AD can be expressed as $d_\perp + d_\Delta$.
[2] In the tissue dependent diffusion model RD is denoted as $d_\perp$.

relate with the volume[3] of these structures, thus suggesting that partial voluming plays a role in the estimation of these quantities. Because of that, they strongly recommend that white matter volume be used as a co-variate in future studies using these metrics. In another study, high resolution, *ex vivo* images from human subjects were blurred to obtain low resolution data. In the FA maps computed using the latter, white matter pathways appeared thinner compared to their high resolution versions as a result of partial voluming [79]. The tissue dependent diffusion model introduced in Chapter 2 aims to address the estimation issues caused by the isotropic (but not anisotropic) partial volumes by directly estimating the volume fractions of the three main tissue types, as well as their corresponding diffusion tensors. As discussed in Chapter 3, the results obtained with this model appear to describe the white matter properties more accurately compared to the traditional diffusion tensor-based analysis.

In Sections 4.3 and 4.4 we examine the values of FA as well as RD, AD and MD in a healthy cohort of varying age. The first set of four coefficients is calculated using the standard diffusion tensor model; the second set uses the white matter tensor from the tissue dependent diffusion model. As in Chapter 3, we precede the quantities from the second set with a suffix 'fibre' (fibre FA and so on) to stress their white matter specificity. Note that the four variables of each set are dependent, with only two degrees of freedom when using cylindrical tensors, and as a result not all combinations of change can occur. However, we find it useful to present all four coefficients in order to enable the comparison of our results with past and future studies that only use a subset of them.

4.1.3 Patterns of change

Two recent studies [26, 17] systematically examined the patterns of age-related change in the diffusion measures using TBSS (a selection of their findings compared to our results can be found in Table 4.2 on page 106). The most prominent pattern found by both studies was a drop in FA caused by an increase in RD (FA↓ RD↑ MD↑), consistent with the effects of demyelination. A fraction of the voxels where this pattern was present also showed signs of axonal pathology, evidenced by a rise in AD (FA↓ RD↑ AD↑ MD↑). When considering thin fasciculi running near the ventricles, such as fornix, it was hypothesised that the observed changes were exacerbated by volume loss leading to increased partial voluming from the neighbouring cerebrospinal

[3]The authors define tract volume as a number of voxels traversed by the tractography streamlines [118].

fluid [17]. A less common pattern of a rise in RD accompanied by a fall in AD (FA↓ RD↑ AD↓) was also consistently identified. This suggests some axons are undergoing secondary (Wallerian-like) degeneration; it has been hypothesised that distal, ischæmic white matter lesions could be responsible in this case. An even less common variation of this pattern, without the rise in RD (FA↓ AD↓ MD↓), has also been found. This change, peculiarly leading to a fall in MD, is thought to occur due to gliosis, early after axonal injury. An alternative hypothetical reason is less coherent organisation of fibres in a bundle [17].

As far as the global distribution of the voxels affected by age-related changes is concerned, earlier studies [93, 87, 105, 106] found that frontal white matter, such as genu of corpus callosum, was more affected by lowering FA and raising MD than parietal and occipital pathways, for example the splenium. The existence of such *anterior-posterior gradient* was confirmed by further research [25, 39, 75, 17, 26]. Interestingly, this spatial pattern is compatible with myelin pathology being the most common type of neurodegeneration. Demyelination according to *anterior-posterior gradient* would invert the order of myelination during brain development, which follows posterior-anterior course. This would provide a putative explanation for the existence of the pathology gradient: the areas that become fully myelinated last are most vulnerable to mylodegeneration in old age. This *anterior-posterior gradient* is not the only spatial regularity in neurodegeneration; recent studies of fibres traversing the internal capsule [108, 107] indicate a complementary pattern of change. The authors found greater age-related degradation in the superior portion of the examined fibres, thus suggesting a *superior-inferior gradient* of change.

It is worth noting that greater frontal degeneration is not necessarily compatible with the frontal ageing hypothesis, whereby cognitive ageing and loss of function is mediated by the decline of neural tissue located specifically in the frontal lobes [119, 51]. To the contrary, cingulum bundle and uncinate fasciculus have been reported to change gradually as they traverse frontal and parietal lobes, with no step change at the lobe boundary [39]. This suggests that age-related degeneration is not confined or specific to frontal lobes only.

4.2 Materials and methods

4.2.1 Subjects and imaging

Data analysed in this chapter were collected from 35 healthy, right-handed volunteers aged 25–65 years (mean 43.85). A subset of images were used in Chapter 3 to examine in detail the maps of estimated tissue type segmentations, white matter fibre orientations and various measures of diffusivity. Acquisition and pre-processing details can be found in Section 3.1.1 (page 57). It is worth stressing that the age range of this study is limited: the subjects are not very old and do not yet suffer from age-related cognitive decline. Accordingly, we do not expect to see major changes in brain structure and physiology. Rather, we are looking for symptoms of initial, mild change, which might lead to more significant degeneration in the future.

4.2.2 Tractography

In order to see which connections are negatively affected in early ageing and which pathological processes might be responsible, we investigate a range of major pathways (see Figure 4.1) using tract masks obtained with neighbourhood tractography [33, 35, 36] (implemented in TractoR [34], `http://www.tractor-mri.org.uk/`). As described in Chapter 1 (page 24), this approach utilises tract shape modelling to adaptively choose seed points that produce the streamlines best matching the course of each fasciculus, as given by the reference tract. Similarly to the original neighbourhood tractography formulation, we employ `probtrackx` and `bedpostx` (see [16, 15] and pages 18 and 21 in Chapter 1) from the FSL toolkit [100, 121, 60] as an underlying fibre tracking algorithm and a multiple fibre orientations' estimation tool, respectively. Reference tracts for neighbourhood tractography were generated from a tractography-based brain atlas [57] according to the procedure described by Muñoz-Maniega et al. [76].

Example segmented pathways from the same individual are shown in Figure 4.1. Similar images for all subjects were visually inspected in order to reject aberrant reconstructions, particularly those branching into neighbouring structures. The fact that such quality control is needed is evidenced by group tractography maps, featuring aggregated cohort-wide results, shown in Figure 4.2. While in general the segmented tracts tend to follow the course consistent with known anatomy, spurious branches are occasionally found, particularly for uncinate fasciculi, cingulum bundles and cor-

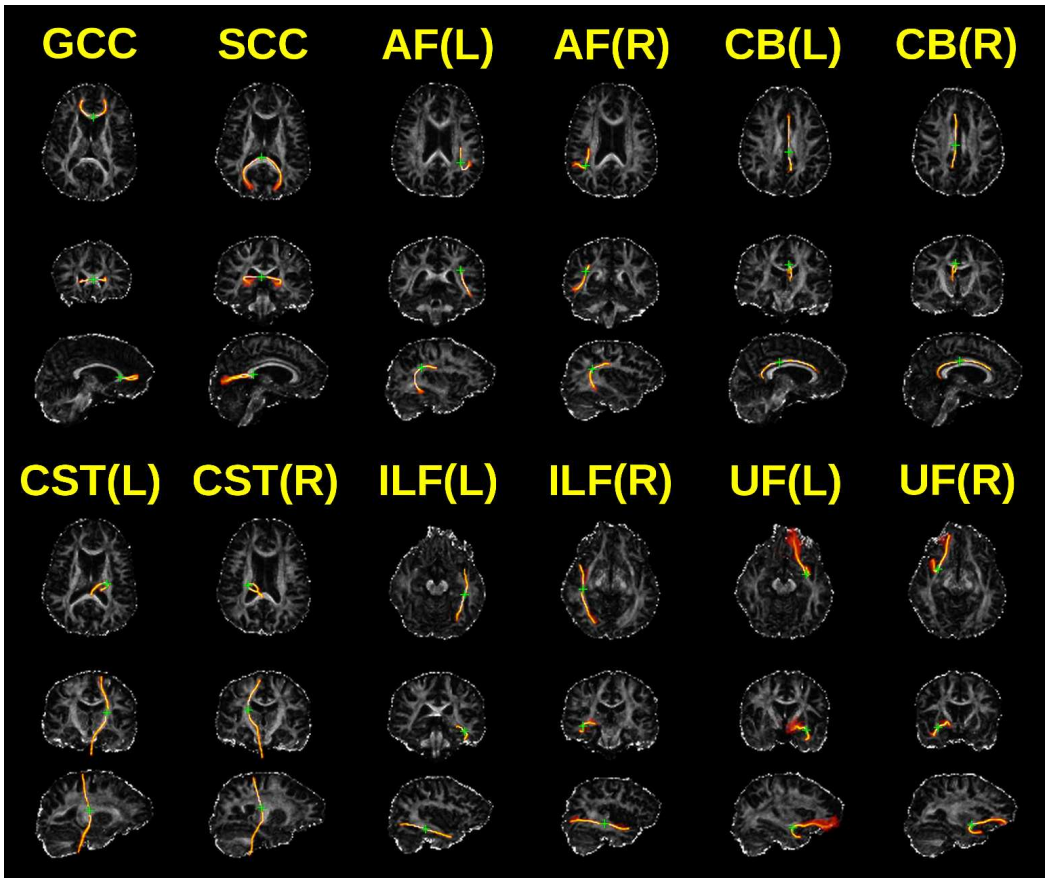

Figure 4.1: Example segmentations of all tracts analysed (from a single subject): genu (GCC) and splenium (SCC) of corpus callosum, arcuate fasciculi (AF), cingulum bundles (CB), corticospinal tracts (CST), inferior longitudinal (ILF) and uncinate (UF) fasciculi. Images show maximum values of the probability of connection to the seed, taken in the direction perpendicular to the image and projected onto the plane on which the seed point lies. Note that, in accordance with the radiological convention, subject's left is on the right-hand side of the image and their right is on the left.

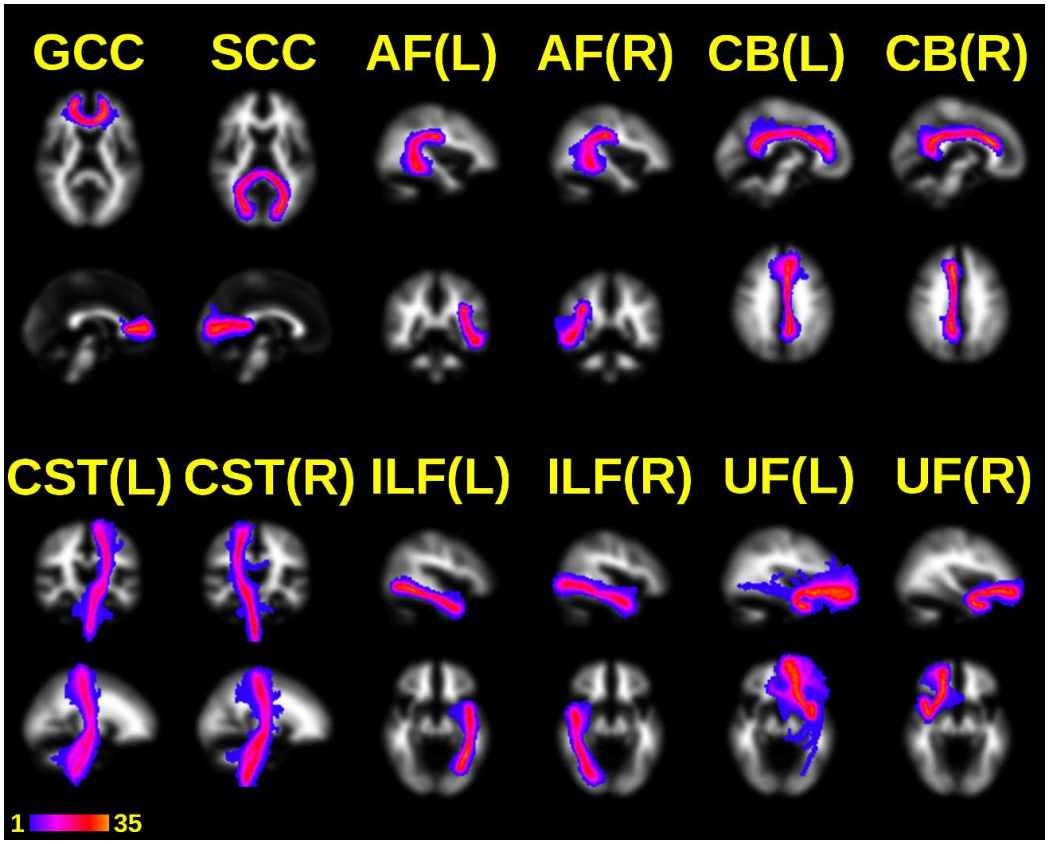

Figure 4.2: Group tractography maps in standard (MNI) space: colour indicates the number of subjects for which particular voxel was included in the tract mask. Pathways are: genu (GCC) and splenium (SCC) of corpus callosum, arcuate fasciculi (AF), cingulum bundles (CB), corticospinal tracts (CST), inferior longitudinal (ILF) and uncinate (UF) fasciculi. Note that, in accordance with the radiological convention, subject's left is on the right-hand side of the image and their right is on the left.

ticospinal tracts. Pathways deemed unacceptable were excluded from analysis and the final number of tracts we use can be found in Table A.1 (page 162).

Tract masks obtained from `probtrackx` encode the number of streamlines passing through each voxel. As discussed in Chapter 1, these counts can be normalised to obtain the probability of connection to the seed point. However, the probabilities obtained in this way tend to decline away from the seed. Moreover, the tissue dependent diffusion model describes partial voluming directly and thus there is no need for additional weighting of tract voxels. This is why we opted for a simpler approach, whereby tract masks are binarised i.e. all voxels traversed by at least one streamline contribute equally to the analysis.

4.2.3 Analysis

It is worth emphasising that this work is a cross-sectional study, rather than a longitudinal one. This means that we look at *changes with age* only indirectly, by examining the *age differences* across our cohort. We expect that the trends identified on the basis of these differences reflect the processes affecting the individual brain during the course of ageing. Throughout the chapter the term 'change' refers to these indirectly observed processes. All trends have been identified using ordinary least squares linear regression. We consider the results to be significant when $p < 0.05$ using two-tailed T-tests. This chapter often examines averages of white matter-specific measures of diffusion, such as RD, across a particular tract (or the whole brain). These weighted averages use the white matter volume fractions estimated by the tissue dependent diffusion model:

$$\text{weighted mean}(\text{RD}) = \frac{\sum \text{RD} \times v_{\text{WM}}}{\sum v_{\text{WM}}},$$

where both summations are across all the voxels belonging to the given structure. Intuitively, the contribution of each voxel is proportional to the amount of white matter it contains.

Apart from structural changes manifested in the differences in FA, MD, AD, RD and their fibre specific equivalents, it would be interesting to investigate white matter atrophy on a whole brain and pathway level. Unfortunately, careful examination of Figure 4.1 shows that the segmented tract masks, while following correctly the course of the white matter pathways, do not in general cover their entire width. This means that the masks are too thin to examine age-related white matter atrophy as the effects of uncertainty in fibre orientations can be expected to dominate over the volumetric changes.

4.3 Whole brain measures

4.3.1 Volume and atrophy

Figure 4.3 presents the distributions of whole-brain white matter, grey matter and cerebrospinal fluid volumes across our cohort. Total intracranial volume, here approximated as the sum of all three tissue type volumes, is also shown. The figure compares two different sets of results: the T_1-weighted volumes segmented using FAST [122] and the output of the tissue dependent diffusion model computed on the basis of the diffusion-weighted data. While the estimated white and grey matter volumes are similar using both modalities, cerebrospinal fluid volume and the total intracranial volume are systematically higher in T_1-weighted images. We expect these large differences to originate on the outside of the brain, in the space occupied by cerebrospinal fluid and cerebral meninges, and essentially to be a by-product of brain masking. As described in Section 3.1.1, all the images analysed in this work were automatically skull-stripped using BET [98]; the diffusion-weighted dataset brain mask was additionally shrunk by 2 voxels to avoid examining the regions where this modality is prone to acquisition artefacts, such as eddy current induced distortion or magnetic susceptibility artefacts. The average volume shed during this operation was 440cm^3, which is similar to the observed volumetric differences between the two modalities. In general, correct estimation of the intracranial volume is difficult since it requires an accurate delineation of the boundary between the cerebrospinal fluid that bathes the brain and the surrounding tissue such as the skull and the eyeballs [13]. Direct comparison of the intracranial volume between the two modalities is further complicated by the differences in their resolution, acquisition and contrast between brain and non-brain tissue.

Looking at the age differences, we observe some evidence of the atrophy of neural tissue (grey matter in particular) accompanied by the expansion of cerebrospinal-fluid-filled spaces. Figure 4.4 shows the whole-brain volumes of all three tissue types estimated with the tissue dependent diffusion model, plotted against the ages of the subjects, along with least-squares regression lines and relevant statistics. It is worth noting that the absolute volume of each tissue type (Figure 4.4, top row) is necessarily noisy as it depends both on the tissue composition of each individual's brain and on the brain size. Fortunately, it is easy to account for the variation in brain size by normalising the volume of all tissue types by the (approximated) total intracranial volume. This operation greatly reduces the inter-subject variation and therefore increases the sensitivity of our investigation. We refer to these normalised volumes as whole-brain

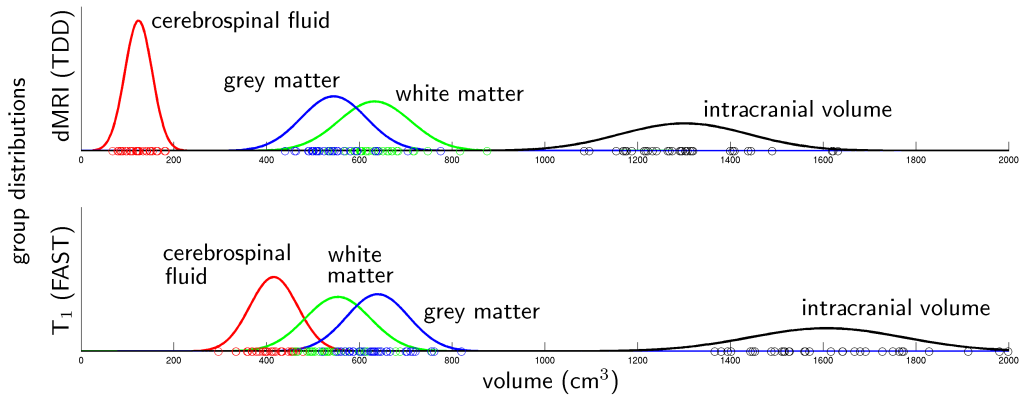

Figure 4.3: Intracranial volume for each subject (black rings), along with the constituent whole-brain volumes of the white matter, grey matter and cerebrospinal fluid. Top: results from the tissue dependent diffusion (TDD) model on the diffusion MRI data. Bottom: results of FAST segmentation of the T_1-weighted images. Normal distributions were fitted to each data group for visualisation purposes. As discussed in the text, the differences in the volume of cerebrospinal fluid and total intracranial volume can be explained by the additional shrinking applied to the diffusion dataset brain mask, after the automated brain extraction with BET. The average volume shed during this operation was 440cm^3.

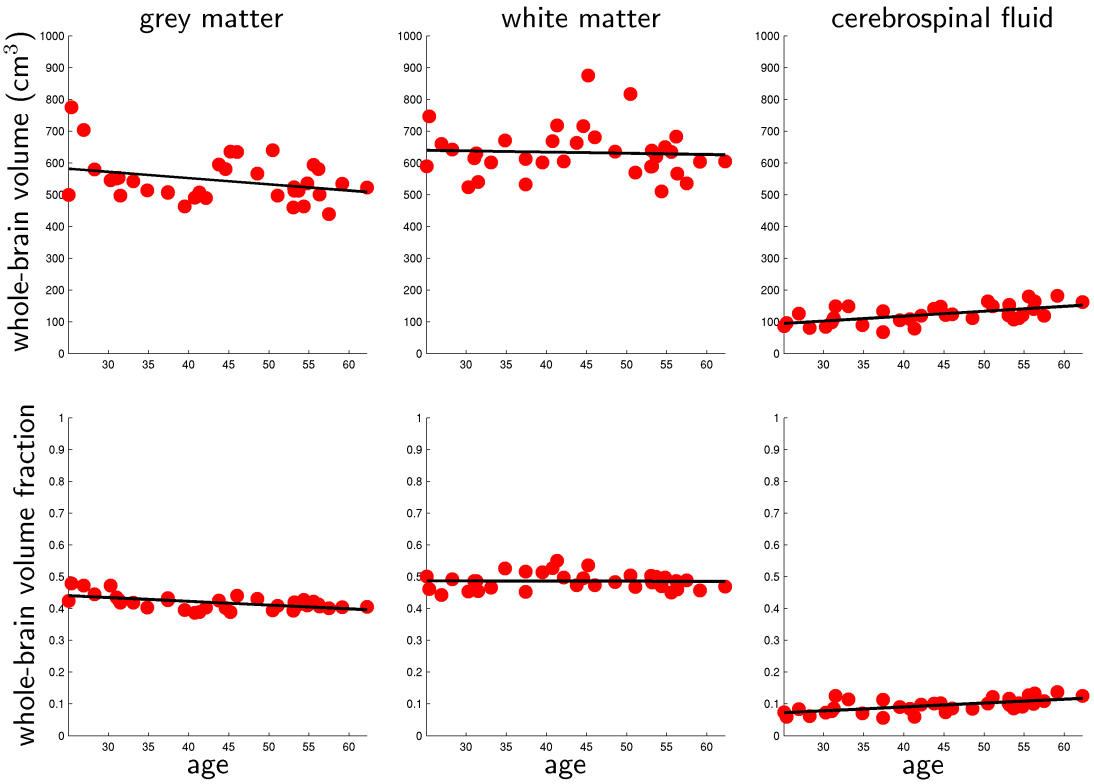

	grey matter		white matter		cerebrospinal fluid	
	absolute	fraction	absolute	fraction	absolute	fraction
p-value	0.072	**0.00049**	0.76	0.93	**0.00031**	**0.00011**
standard error	67.8	0.02	78.4	0.026	24.4	0.018
slope (per year)	-2cm^3	-1.2‰	-0.38cm^3	-0.039‰	1.5cm^3	1.2‰
trend	none	↘	none	none	↗	↗

Figure 4.4: Volumetric age differences based on segmentation obtained with the tissue dependent diffusion model. Plots: absolute whole-brain volumes (top) and whole-brain volume fractions (bottom) of grey matter, white matter and cerebrospinal fluid. Table: summary of regression measures (10‰=1%).

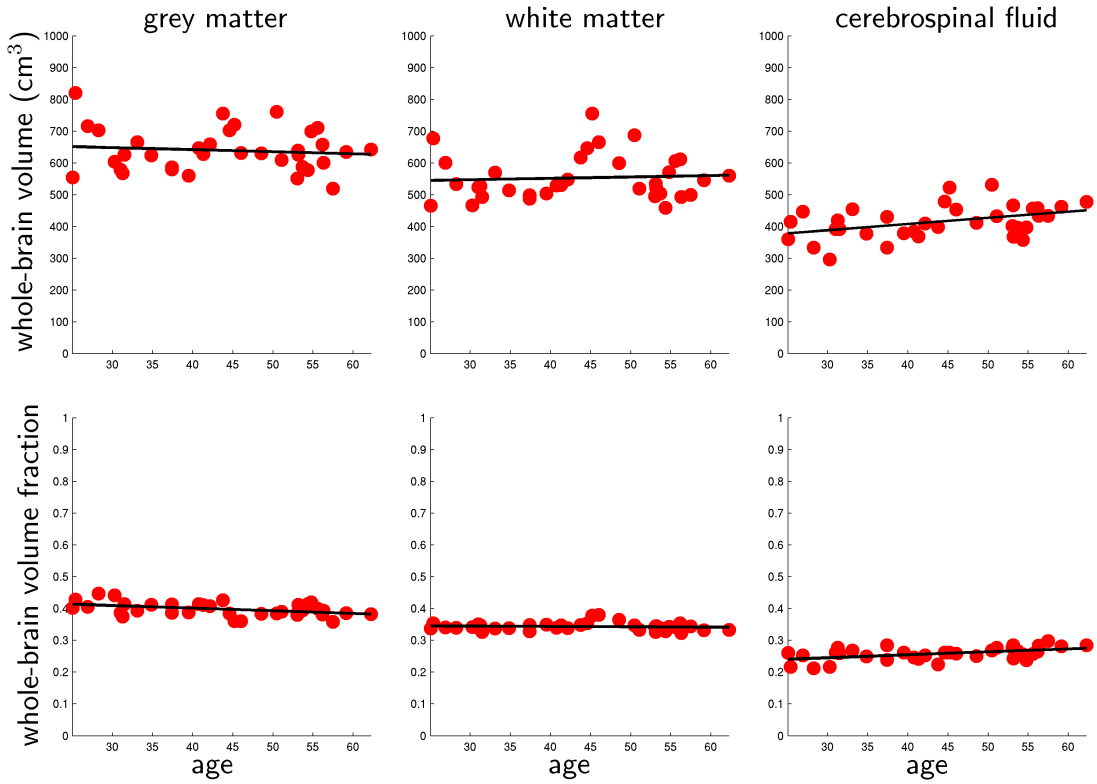

	grey matter		white matter		cerebrospinal fluid	
	absolute	fraction	absolute	fraction	absolute	fraction
p-value	0.54	**0.0099**	0.69	0.62	**0.013**	**0.0025**
standard error	67.7	0.019	71.3	0.013	47.6	0.018
slope (per year)	-0.65cm^3	-0.83‰	0.44cm^3	-0.1‰	2cm^3	0.93‰
trend	none	↘	none	none	↗	↗

Figure 4.5: Volumetric age differences based on T_1-weighted image segmentation obtained with FAST. Plots: absolute whole-brain volumes (top) and whole-brain volume fractions (bottom) of grey matter, white matter and cerebrospinal fluid. Table: summary of regression measures (10‰=1%).

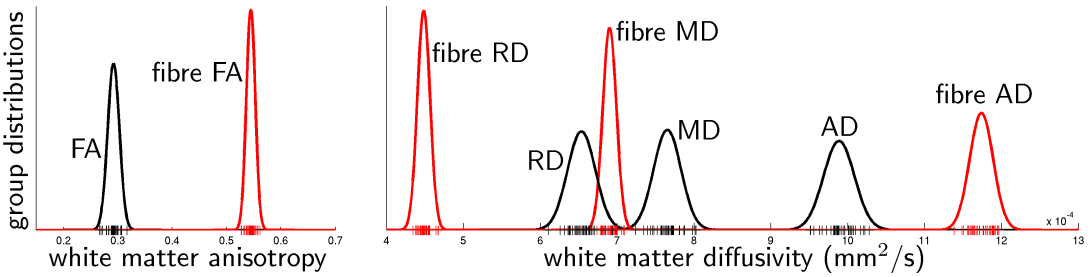

Figure 4.6: Whole-brain averages of anisotropy and diffusivity in white matter. Measures derived from the diffusion tensor model (FA, RD, AD and MD) are compared to analogous quantities computed for the white matter tensor from the tissue dependent diffusion model (labelled 'fibre FA' and so on). Datapoints correspond to single subjects and the distributions over the whole cohort are added to improve visualisation.

volume fractions (Figure 4.4, bottom row). Our results show a significant increase in the volume of cerebrospinal fluid, accompanied by a decrease in the volume of grey matter, while white matter atrophy is not significant. It is worth noting that although there is no evidence of white matter volume decreasing with age, the results point to a possible shift in partial voluming, whereby cerebrospinal fluid displaces grey matter. Figure 4.5 shows volumetric results analogous to those in Figure 4.4, but this time obtained by running FAST segmentation on the T_1-weighted volumes for the same subjects. We note good agreement between these results and the trends identified using the tissue dependent diffusion model.

4.3.2 Diffusion measures

The measures of water molecule diffusion anisotropy and water diffusivity averaged over the entire brain's white matter are presented in Figure 4.6 for all subjects and as distributions across the cohort. Fibre FA tends to produce higher values than the traditional FA, whereas fibre RD and fibre MD are lower than their counterparts from the diffusion tensor model (RD and MD), which is consistent with our observations in Chapter 3. In Section 3.4 (page 70), we demonstrated that AD can be over- or underestimated, depending on the type of partial voluming, because in healthy white matter this quantity is typically greater than grey matter MD, but smaller than MD of cerebrospinal fluid (see Table 2.1 on page 45). We have also argued that fibre AD is likely to be closer to the true value than the traditional AD. On the scale of the whole brain, the diffusion tensor estimate of AD is, on average, lower than fibre AD and

likely lower than the true value, which would suggest that the effects of grey matter partial volumes dominate. Increased fibre FA, with respect to the FA estimate from the diffusion tensor model, is thus accounted for by both lower fibre RD and higher fibre AD with the tissue dependent diffusion model. In all, whole-brain averages of fibre specific measures of diffusion show smaller inter-subject variability, while at the same time the cohort-wide mean values are further apart.

It is worth reminding that the differences in estimated RD and AD arise primarily in voxels with partial voluming (see Figure 3.16 on page 76) and can be explained in terms of averaging the signal from white matter together with the contributions from other tissue types. Similarly, an age-related shift in partial voluming, whereby cerebrospinal fluid partially displaces grey matter as a 'contaminating' isotropic tissue type, can explain the mismatch between the two models when it comes to the estimated trends of change in the diffusivity coefficients.

Age-related changes in FA, RD, AD and MD of white matter, averaged over the whole brain, are presented in Figure 4.7. Data regarding the tissue dependent diffusion model are shown with full markers and summarised in the bottom table, whereas diffusion tensor results are shown with hollow markers and in the top table. The latter set of results replicates the finding of the previous studies, namely that the increase in RD (and the resulting rise in MD, here not significant) tends to be more pronounced than changes in the AD [39, 123]. As discussed in Sections 4.1.2 and 4.1.3, this finding is usually held as evidence that demyelination is the predominant degenerative process in the ageing brain and a plausible major cause of cognitive decline. However, fibre RD does not show a significant change with age, whereas fibre AD significantly decreases. This seems to support an alternative hypothesis of age-related change, namely that the secondary (Wallerian-like) degeneration is the most prevalent type of pathology in healthy ageing.

Crucially, the diverging results and predictions of the two models are compatible with the fact that, in this population, the partial voluming of white matter voxels comes increasingly from cerebrospinal fluid as opposed to grey matter. The existence of this hypothetical shift is supported by our volumetric results (Figures 4.4 and 4.5) and its effects can produce spurious trends in diffusion tensor estimates of the diffusivity coefficients. To see how this happens, let us note that partial voluming from the cerebrospinal fluid causes greater overestimation of white matter's RD (and MD) than if grey matter were present. This is because

$$\tilde{d}_{\text{radial}} < \tilde{d}_{\text{GM}} < \tilde{d}_{\text{CSF}},$$

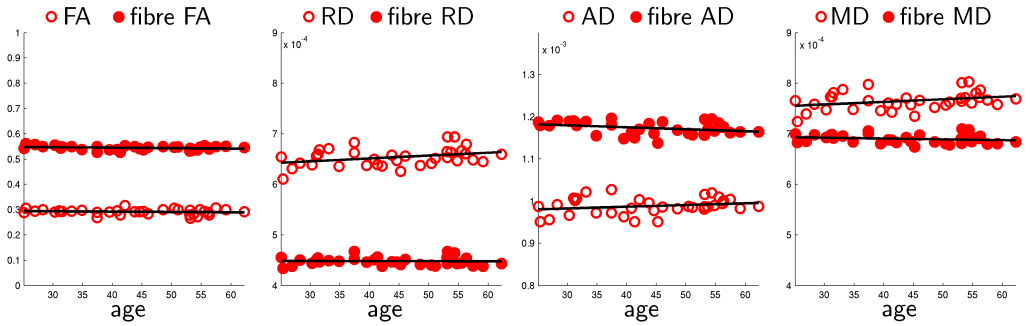

	FA	RD	AD	MD
p-value	0.45	**0.044**	0.2	0.064
standard error	0.0108	1.73×10^{-5}	1.98×10^{-5}	1.72×10^{-5}
slope (per year)	-0.00013	0.57×10^{-6}	0.41×10^{-6}	0.51×10^{-6}
trend	none	↗	none	none

	fibre FA	fibre RD	fibre AD	fibre MD
p-value	0.17	0.92	**0.048**	0.24
standard error	0.00798	0.823×10^{-5}	1.46×10^{-5}	0.876×10^{-5}
slope (per year)	-0.00018	-0.013×10^{-6}	-0.47×10^{-6}	-0.16×10^{-6}
trend	none	none	↘	none

Figure 4.7: Whole brain measures of water diffusion: age differences and trends across the cohort (plots); summary of regression measures (table). Discrepancy in the trends identified with the diffusion tensor and the tissue dependent diffusion model can be explained in terms of partial voluming, which adversely affects the former.

where $\tilde{d}$ denote typical values for healthy tissue (see Table 2.1 on page 45). This means that a shift in partial voluming alone can result in a spurious trend of raising RD where no change is actually present. As far as AD is concerned, we have

$$\tilde{d}_{\mathrm{GM}} < \tilde{d}_{\mathrm{axial}} < \tilde{d}_{\mathrm{CSF}},$$

which means that also in this case the overestimation grows if cerebrospinal fluid displaces grey matter. A genuine age-related decrease in AD could, under such conditions, be cancelled by the apparent growth of this coefficient due to the partial voluming shift.

4.4 Tract-specific measures

While our results on the whole-brain level seem to point to the secondary degeneration as the main factor contributing to the age-related pathology of neural connections, it is conceivable that some pathways undergo alternative degeneration processes, such as demyelination. Their symptoms might not be apparent when looking at the entire brain due to noise and the effects of different types of pathology partially cancelling out. We therefore investigate some of the major commisural (genu and splenium of corpus callosum), association (cingulum bundles; arcuate, uncinate and inferior longitudinal fasciculi) and projection (corticospinal tracts) pathways in order to examine this possibility. Example segmentations of these tracts in a single subject are presented in Figure 4.1. Our most interesting findings are presented below; full results for all examined pathways, including trend plots, numbers of segmentations accepted for analysis and cross-cohort tract averages of quantities of interest, can be found in Appendix A (Figures A.1–A.12 and Table A.1). Table 4.1 (page 105) provides a summary of tract-specific findings while comparison with the previous results can be found in Table 4.2 (page 106).

Age-related changes, consistent with existing literature, can be clearly identified in genu of corpus callosum (Figure 4.8). Both diffusion tensor and fibre-specific measures show a significant drop in FA and increase in all measures of diffusivity (**FA**$\downarrow$ **RD**$\uparrow$ **AD**$\uparrow$ **MD**$\uparrow$ and $\mathrm{FA_f}\downarrow$ $\mathbf{RD_f}\uparrow$ $\mathbf{AD_f}\uparrow$ $\mathbf{MD_f}\uparrow$), indicating demyelination accompanied by axonal loss. Such pattern of change for frontal commisural connections has previously been reported in [26] and [17]. An alternative explanation for the observed pattern would be an increase of partial voluming from cerebrospinal fluid. Unfortunately, this hypothesis is difficult to verify using available data since the

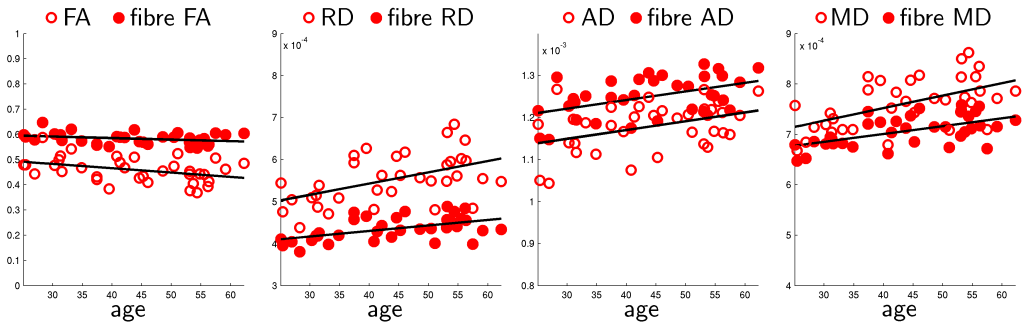

	FA	RD	AD	MD
p-value	**0.022**	**0.0022**	**0.017**	**0.0006**
trend	↘	↗	↗	↗
slope (per year)	-0.0017	2.7×10^{-6}	2.1×10^{-6}	2.5×10^{-6}

	fibre FA	fibre RD	fibre AD	fibre MD
p-value	0.083	**0.0017**	**0.0044**	**0.00038**
trend	none	↗	↗	↗
slope (per year)	-0.00062	1.3×10^{-6}	2.1×10^{-6}	1.6×10^{-6}

Figure 4.8: Measures of water diffusion in genu of corpus callosum show strong age-related trends, consistent with existing literature. Plots: age differences and trends across the cohort. Table: summary of regression measures.

tractography-based segmentations do not cover the entire tract volume and therefore make it impossible to assess changes in partial voluming on the tract level.

When it comes to corticospinal projection fibres (Figure 4.9) we detect falling fibre AD and fibre MD in the left hemisphere (**AD**$_f\downarrow$ **MD**$_f\downarrow$), indicative of gliosis. Our investigation thus seems to support the findings of Burzynska et al. [26] and Bennett et al. [17], who reported evidence of axonal injury in posterior limb of internal capsule and signs of secondary (Wallerian-like) degeneration in superior corona radiata. Results from the diffusion tensor model fail to detect significant changes in corticospinal tracts.

A partially significant, but consistent pattern of change can be observed for the uncinate fasciculi (Figure 4.10), where a drop in fibre FA can be attributed to an increase in fibre RD, but not fibre AD (**FA**$_f\downarrow$ left and FA$_f\downarrow$ RD$_f\uparrow$ right) points to demyelination as the major pathological process affecting these pathways (for diffusion tensor: FA$\downarrow$ RD$\uparrow$ right). Similar results have been reported for ventral medial frontal gyrus by Burzynska et al. [26] and for left frontal cluster by Bennett et al. [17]. These clusters

of voxels seem to partially overlap with the course of uncinate fasciculi.

The same authors found signs of demyelination in dorsal cingulum (anterior and posterior) and sagittal stratum [26, 17], areas which appear to coincide with cingulum bundles as well as inferior longitudinal and arcuate fasciculi. Looking at the entire pathways, however, we do not see any significant symptoms of myelin pathology. When it comes to splenium of corpus callosum, no signs of neurodegeneration are detectable in anisotropy or diffusivity measures. This result is in line with previous studies which have found that frontal, rather than occipital, commisural connectivity is affected in normal, healthy ageing [107].

When it comes to comparing the two diffusion modelling frameworks, pathway averages of fibre-specific metrics of water diffusion anisotropy and diffusivity in white matter tend to yield more significant trends than their equivalents from the diffusion tensor model (see Figures 4.8–4.10 and Table 4.1). A closer look at the results reveals that data from the tissue dependent diffusion model consistently show decreased inter-subject variability, reflected in reduced standard error of the trends (see Figure 4.11). Importantly, the trends themselves are usually preserved, suggesting that the removed source of variation is independent of age. We believe that partial voluming from isotropic tissue types (grey matter and cerebrospinal fluid), which itself could be dependent on differences in brain anatomy and size, is the source of this variability.

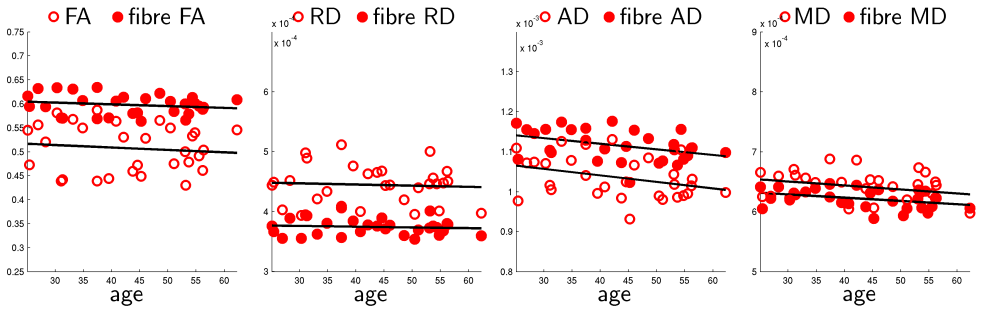

Left corticospinal tract

	FA	RD	AD	MD
p-value	0.55	0.74	0.065	0.13
trend	none	none	none	none
slope (per year)	-0.00051	-0.19×10^{-6}	-1.6×10^{-6}	-0.67×10^{-6}

	fibre FA	fibre RD	fibre AD	fibre MD
p-value	0.32	0.61	**0.031**	**0.036**
trend	none	none	↘	↘
slope (per year)	-0.00037	-0.12×10^{-6}	-1.4×10^{-6}	-0.55×10^{-6}

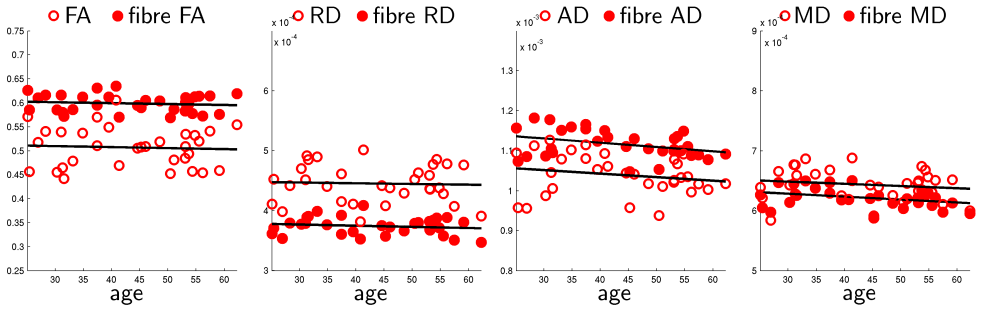

Right corticospinal tract

	FA	RD	AD	MD
p-value	0.76	0.82	0.28	0.39
trend	none	none	none	none
slope (per year)	-0.00021	-0.12×10^{-6}	-0.87×10^{-6}	-0.37×10^{-6}

	fibre FA	fibre RD	fibre AD	fibre MD
p-value	0.54	0.41	0.054	0.059
trend	none	none	none	none
slope (per year)	-0.00019	-0.2×10^{-6}	-1.1×10^{-6}	-0.49×10^{-6}

Figure 4.9: Measures of water diffusion in left (top) and right (bottom) corticospinal tract. Plots: age differences and trends across the cohort. Table: summary of regression measures.

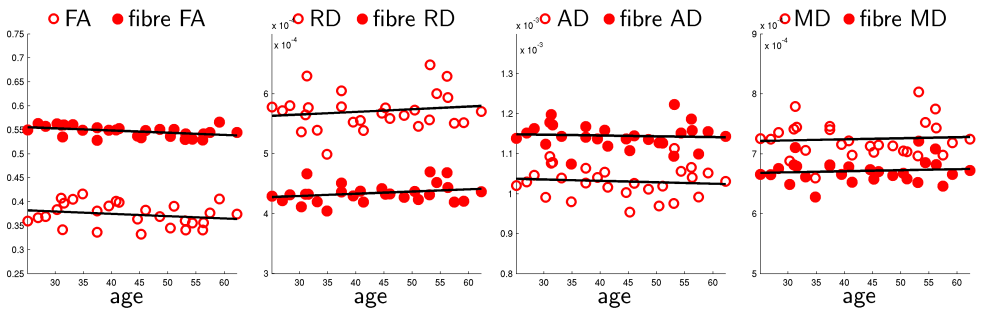

Left uncinate fasciculus

	FA	RD	AD	MD
p-value	0.26	0.43	0.6	0.74
trend	none	none	none	none
slope (per year)	-0.00048	0.44×10^{-6}	-0.36×10^{-6}	0.18×10^{-6}

	fibre FA	fibre RD	fibre AD	fibre MD
p-value	**0.018**	0.19	0.73	0.61
trend	↘	none	none	none
slope (per year)	-0.00045	0.37×10^{-6}	-0.2×10^{-6}	0.18×10^{-6}

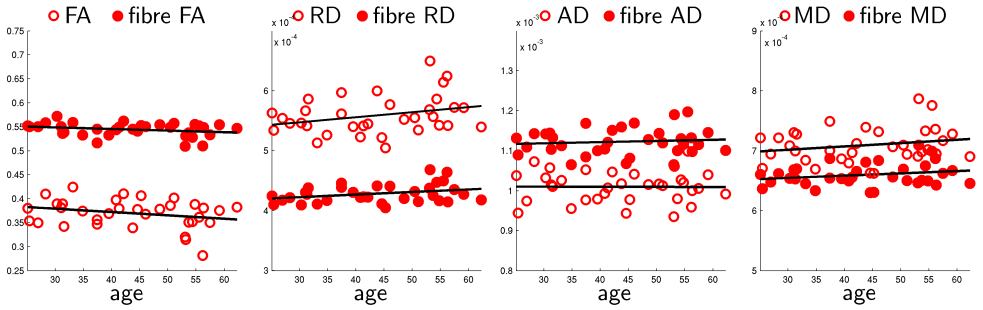

Right uncinate fasciculus

	FA	RD	AD	MD
p-value	0.14	0.093	0.97	0.23
trend	none	none	none	none
slope (per year)	-0.00069	0.84×10^{-6}	-0.023×10^{-6}	0.56×10^{-6}

	fibre FA	fibre RD	fibre AD	fibre MD
p-value	0.14	0.072	0.58	0.2
trend	none	none	none	none
slope (per year)	-0.00033	0.43×10^{-6}	0.29×10^{-6}	0.38×10^{-6}

Figure 4.10: Measures of water diffusion in left (top) and right (bottom) uncinate fasciculus. Plots: age differences and trends across the cohort. Table: summary of regression measures.

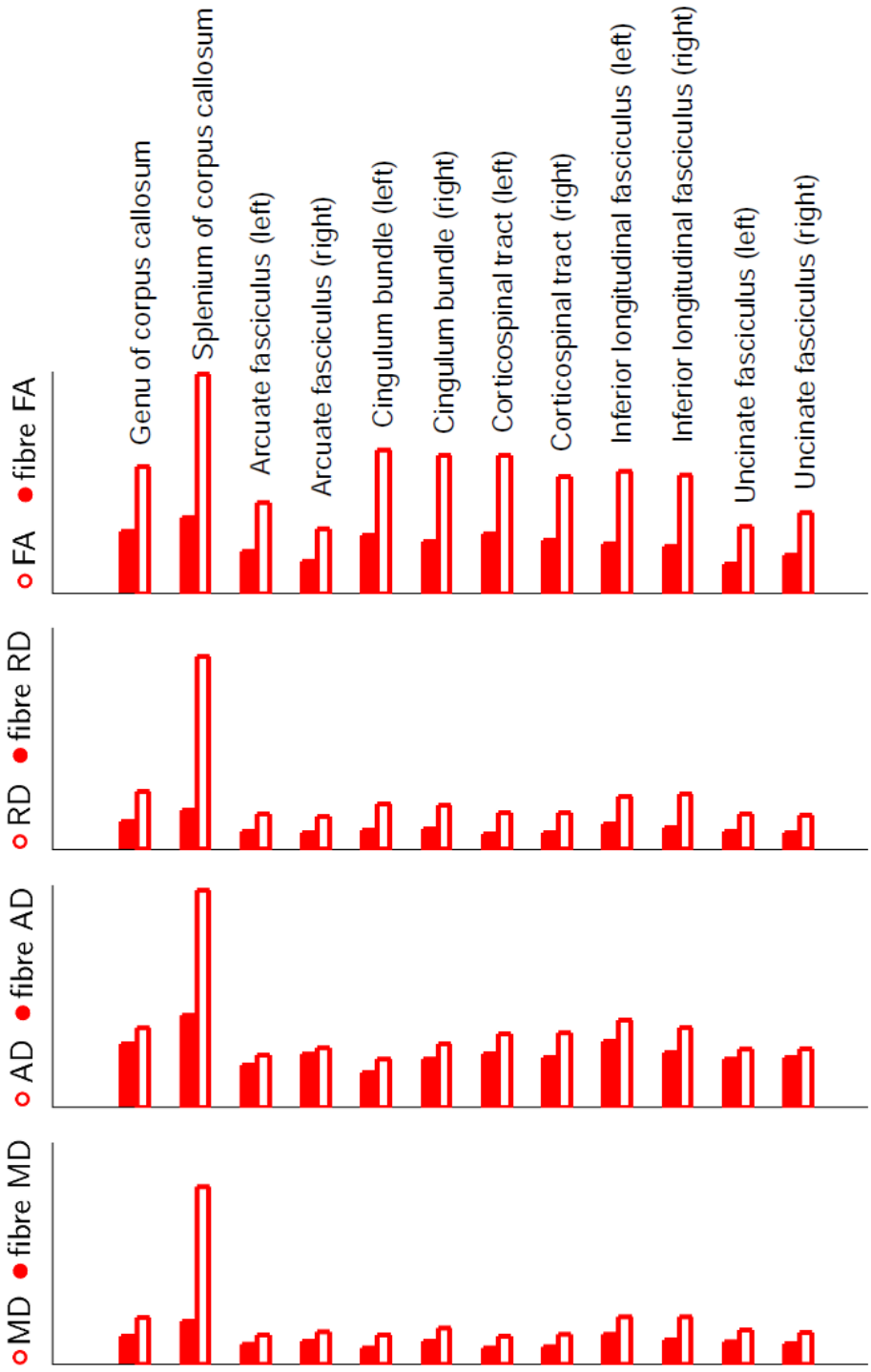

Figure 4.11: Standard errors for linear regression for all pathways and metrics examined in this study. Fibre-specific quantities (full bars) show reduction in standard error with respect to the metrics from the diffusion tensor model (hollow bars), suggesting reduced partial voluming-related variability and increased sensitivity.

diffusion tensor

Patterns of change: **significant** ($p < 0.05$), indicative ($p < 0.15$)		
Tract	Left hemisphere	Right hemisphere
Genu of corpus callosum	**FA↓ RD↑ AD↑ MD↑**	
Splenium of corpus callosum	(no change)	
Arcuate fasciculi	(no change)	(no change)
Cingulum bundles	(no change)	(no change)
Corticospinal tracts	AD↓ MD↓	(no change)
Inferior longitudinal fasciculi	(no change)	(no change)
Uncinate fasciculi	(no change)	FA↓ RD↑

tissue dependent diffusion

Tract	Left hemisphere	Right hemisphere
Genu of corpus callosum	$FA_f\downarrow$ $\mathbf{RD_f\uparrow}$ $\mathbf{AD_f\uparrow}$ $\mathbf{MD_f\uparrow}$	
Splenium of corpus callosum	(no change)	
Arcuate fasciculi	(no change)	(no change)
Cingulum bundles	(no change)	(no change)
Corticospinal tracts	$\mathbf{AD_f\downarrow}$ $\mathbf{MD_f\downarrow}$	$AD_f\downarrow$ $MD_f\downarrow$
Inferior longitudinal fasciculi	(no change)	(no change)
Uncinate fasciculi	$\mathbf{FA_f\downarrow}$	$FA_f\downarrow$ $RD_f\uparrow$

Table 4.1: Summary of the pathway-specific age-related differences in the measures of water diffusion in white matter, estimated with the diffusion tensor model (top) and the tissue dependent diffusion model (bottom). Fibre-specific quantities are marked with an 'f' subscript, e.g. FA_f.

4.5 Conclusions

This chapter examined age-related differences in the measures of water diffusion in the brain tissue across a cohort of healthy volunteers from 25 to 65 years of age; patterns of change in this age group are subtle and thus challenging to investigate. Apart from the traditional measures of diffusivity and anisotropy obtained with the diffusion tensor model, we have looked at analogous, fibre-specific quantities estimated from the tissue dependent diffusion model presented in this work. These quantities are computed on the basis of the white matter compartment only and promise to alleviate the effects of partial voluming from isotropic tissue types, grey matter and cerebrospinal fluid. It is worth noting that using the fibre-specific measures results in reduced standard error, and thus increased sensitivity, both on whole brain and tract level. This suggests that

Axonal and myelin degeneration	
Genu of corpus callosum ($FA_f\downarrow$ **$RD_f\uparrow$** **$AD_f\uparrow$** **$MD_f\uparrow$**)	Genu of corpus callosum (FA↓ RD↑ AD↑ *MD↑*) [17, 26]
Demyelination	
Uncinate fasciculi (**$FA_f\downarrow$**) left ($FA_f\downarrow$ $RD_f\uparrow$) right	Left frontal cluster (FA↓ RD↑) [17] Ventral medial frontal gyrus (FA↓ RD↑ MD↑) [26]
Axonal injury (ischæmic)	
Corticospinal tracts (**$AD_f\downarrow$** **$MD_f\downarrow$**) left ($AD_f\downarrow$ $MD_f\downarrow$) right	Posterior limb of internal capsule (FA↓ AD↓ MD↓) [26] Superior corona radiata* (FA↓ RD↑ AD↓ *MD↑*) [17, 26]

Table 4.2: Summary of **significant** ($p < 0.05$), indicative ($p < 0.15$) patterns from our work and those found in the literature, along with the putative underlying pathological mechanisms (*suggests secondary degeneration due to distal lesions). Note that the results from the TBSS studies [17, 26] report named clusters of voxels, whereas we examine the whole pathways. Also note that [17] do not analyse MD.

the measures computed from the tissue dependent diffusion model are less affected by the variability in partial voluming.

Tract-specific results confirm previous findings: we report significant age-related changes in genu of corpus callosum (indicative of both axonal and myelin degeneration) and corticospinal tracts (suggestive of axonal injury), as well as some evidence of demyelination in uncinate fasciculi and no change in splenium of corpus callosum. On a whole brain level, a drop in fibre AD provides some evidence that mild secondary degeneration, not demyelination, is the prevalent degenerative process at the early stages of ageing. Earlier studies generally considered RD, not AD a better marker of degenerative change [39, 75, 123]; it has to be noted, however, that the latter can raise or fall, depending on the type of pathology. What is more, we have shown that, with diffusion tensor model, a shift in partial voluming, whereby cerebrospinal fluid partially displaces grey matter as a ‘contaminating’ isotropic tissue type, can lead to spurious trends of growing RD, at the same time obscuring (cancelling out the effect of) falling AD.

Chapter 5

Spatial information pooling

The tissue dependent diffusion model presented in Chapter 2 is a framework for modelling diffusion of water molecules in brain tissue. The posterior distribution over the parameters of this model is estimated using a sampling method based on the Metropolis-Hastings MCMC with a custom burn-in schedule. The reliability of this estimation has been tested on synthetic data, as well as human brain images, leading to the conclusion that it yields plausible tissue type segmentations and white matter fibre orientations, as well as improved estimates of the diffusivity parameters. However, crossing fibre regions and isotropic partial voluming still present problems while fitting the model, even if the latter is greatly reduced in comparison to the standard diffusion tensor model. Further improvements in one-fibre parameter estimation could potentially be achieved if additional prior knowledge was harnessed to inform and constrain the learning.

While looking at single voxels offers significant benefits such as trivial distributed computation and ease of interpretation of the results, it fails to make use of all the available information. White matter fibre orientations, for example, are not independent in the neighbouring voxels; in general, we expect the brain tissue to exhibit some degree of spatial coherence. This crucial idea, whereby data measured in one voxel holds information relevant beyond its borders, leads us to consider spatial pooling of information with the aim of alleviating the effects of the measurement noise and further stabilising the estimation in the tissue dependent diffusion model. While modelling crossing fibres is beyond the scope of this work, we note that the capability of incorporating the sources of information other than single-voxel diffusion attenuation is the prerequisite to developing any such models without over-simplifying the diffusion description.

This chapter begins by reviewing the expected variability of the parameters de-

scribing the main cerebral tissue types and the means of modelling this variability, in particular by pooling information between the neighbouring acquisition voxels. We propose a simple parameter sharing model as an initial investigation into the effectiveness and potential issues surrounding such information pooling. The analysis of the results of this initial investigation leads us to identify the circumstances in which the shared parameter estimation in the tissue dependent diffusion model is unstable as well as the reasons of such behaviour. As a remedy, we propose introducing constraints on the joint variability of the T_2-weighted signal for different tissue types. The dependence between these variables can be justified in terms of spatial inhomogeneities in the net magnetisation and implementing it leads to a marked improvement in the estimated tissue type segmentations. Lastly, we investigate the impact of using alternative set of prior distributions over the diffusivity parameters.

5.1 Variability and sources of information in the brain

As noted in the introduction above, treating each imaging voxel independently fails to capture anatomical knowledge about the brain's functional structures, such as white matter pathways, and how the parameters describing each tissue type (specifically diffusivities and T_2-weighted intensities) vary across these structures and the brain at large. The diffusivity of the cerebrospinal fluid, for example, can be reasonably assumed to stay constant at normal brain temperature; similarly its characteristic T_2 time. T_2 of grey and white matter is potentially affected by tissue density. In general, the T_2-weighted signal for all tissue types also depends on the magnetic field inhomogeneity due to varying magnetic susceptibility, which could introduce additional, slow variation across the brain. Nonetheless, a significant degree of similarity between the neighbouring voxels can be expected. The diffusivity parameters of grey and, particularly, white matter can vary from one structure to another, or even between different sections of the same pathway [39]. However, a degree of local coherence can reasonably be expected also in this case; sharp transitions could conceivably arise only on the borders between different functional structures characterised by different microstructure and diffusion properties. White matter fibre orientations in the neighbouring voxels are not independent, but rather vary smoothly along the same fasciculus, a fact used to segment pathways with tractography. Finally, the acquisition noise level can be assumed to be locally smooth. It has to be noted, however, that the estimated Rician noise level in the tissue dependent diffusion model, ς, also depends on model residuals, i.e. the

signal components poorly explained by the forward model. For example, ς could be elevated in crossing fibres' voxels when using a single fibre forward model of diffusion. This makes the smoothness of the acquisition noise level impractical to use as a source of information.

The above assumptions of local similarity could serve as sources of information when estimating the parameters of diffusion models. The challenge lies in incorporating these assumptions into the model, while preserving genuine variability. Volume fractions are subject to a different kind of spatial coherence: the transitions between neighbouring voxels are not constrained in any way. For instance, on a ventricular boundary one tissue type abruptly finishes and gives way to another. The overall spatial distribution of tissue types, however, is far from random. White matter fibre volumes, for example, must add up to form consistent white matter tracts. This constraint is qualitatively different from local similarity and more challenging to exploit (see discussion in Chapter 6); in this work, we focus on exploiting the spatial similarity assumptions regarding diffusivity and T_2-weighted signal ($S_{\mathrm{CSF}}, S_{\mathrm{GM}}, S_{\mathrm{WM}}, d_{\mathrm{CSF}}, d_{\mathrm{GM}}, d_{\perp}, d_{\Delta}$), which we shall collectively refer to as tissue parameters.

5.2 Approaches to information sharing

5.2.1 Tensor field regularisation

When estimating the parameters of forward diffusion models from data by an optimisation procedure, local coherence can be imposed by adding terms that penalise sharp changes in the parameter values in neighbouring voxels. The use of such tensor field regularisation to spatially smooth the tensor eigenvalues, eigenvectors and volume fractions in a general multi-tensor diffusion model has been demonstrated by Pasternak et al [89]. The authors optimise a variational functional operator composed of the fidelity term, quantifying how well the predicted signal attenuation fit the data, and a smoothness term, which encourages spatial coherence of each parameter and vector. The same technique was later applied in their free water elimination method ([90], see page 18).

5.2.2 Probabilistic information sharing

In a Bayesian setting where generative models link the parameters to the measured signal, a natural alternative to deterministic optimisation with smoothing terms is to

use probabilistic (latent variable) models that allow information to be shared between neighbouring voxels. King et al [68] compared several such models applied to better resolve the orientations of crossing fibres in the pons and internal capsule. The diffusion process was modelled using the ball-and-stick model [16, 15] with a fixed number of three white matter fibre components. Using MCMC sampling, estimation from the independent voxels (without sharing) was compared to that of exchangeable random effects model, Markov random field (MRF) and Besag-York-Mollie model. The sharing of information in these models is facilitated by the use of spatial priors over the shared quantities, namely fibre orientations and T_2-weighted signal. An exchangeable random effects model, for example, involves putting Gaussian priors with unknown means and variances on the shared parameters. This encourages similarity of the estimates, as long as such similarity is not extremely unlikely given the data (in which case the estimated prior variance will be large). The exchangeability in this model means that it does not exploit spatial proximity between individual voxels (other than all voxels belonging to the same ROI). A contrasting approach is represented by the MRF approach, which directly models pairwise similarity between adjacent voxels, but not across the entire ROI (the variance of the pair-wise potential is shared). Besag-York-Mollie model uses a mixture of exchangeable and random field terms, accounting for both spatial (neighbourhood dependent) and exchangeable (neighbourhood independent) variability. All approaches were found to visually improve fibre angle estimates compared to independent voxel treatment by providing more peaked distributions and greater separation of different fibre families. Effectively, this was achieved by using information from the unambiguous voxels to ameliorate the estimation problems in the highly ambiguous partial volume voxels. The authors agree that none of the information-sharing models they have examined are suitable for whole-brain applications due to high computational load. Instead, they suggest that these models could be used adaptively e.g. during tractography. In such a setting, the initial orientation estimates from independent voxels would be augmented by running one of the parameter-sharing algorithms locally, in crossing fibre regions.

5.2.3 Shared parameters and information pooling

The focus of the work by King et al [68] is clearly different from ours: we are interested in realistic diffusion modelling across the entire brain volume. As far as information sharing is concerned, models based on the random field methodology could

conceivably be used to put spatial priors over some of the parameters of the Tissue Dependent Tissue model as they are intrinsically well suited to modelling situations in which quantities of interest change gradually in space. Similarly, using exchangeable priors makes sense where a degree of similarity, but also occasional step changes, need to be accommodated. The crucial weakness that makes it difficult to apply both random field and exchangeable methods on a whole brain basis remains the computational load of learning their parameters in the joint space. As we have noted above, King et al [68] acknowledge this difficulty and suggest that the probabilistic information sharing models could be used locally, where necessary.

Local sharing of some parameters, within a small neighbourhood, remains a computationally feasible modelling option as the smaller number of voxels involved leads to reduced estimation times in the joint space. Whole brain estimation can be achieved by dividing the entire brain volume into small ROIs and running local estimation independently in each of them. This 'tiling' approach would enable trivially distributed computation by allowing the estimation in each sharing region to be performed independently. As for the choice of the sharing model, we believe it is instructive to start from the most basic form of information pooling, whereby some parameters are shared across each ROI. In other words, the same set of shared parameters is used globally in forward models of all voxels and therefore affected by their likelihood contributions. Independently estimated parameters, such as volume fractions, continue to depend only on one voxel's data (although they are affected by the data distribution in the entire ROI via the values of the shared parameters). This set-up can be viewed as a limiting case of both exchangeable and random field models, benefiting from a reduced number of parameters. Examining the results obtained with this simple approach should help answer the question of how much spatial parameter variability is actually necessary to explain the data and should thus verify the need for more flexible models.

Choosing the optimal size of sharing regions remains a difficult issue. Larger regions pool together more information by allowing the data from larger number of voxels to affect the values of the shared parameters. They are more suited for quantities that could in principle be replaced by global point estimates, such as cerebrospinal fluid diffusivity (d_{CSF}). For some quantities, such as white matter diffusivities $d_{\perp}$ and d_{Δ}, this might be overly restrictive. It also limits the spatial resolution of any subsequent analysis of these parameters. These slowly varying parameters should be better modelled by smaller sharing ROIs, which hold the potential for fast distributed com-

putation, but raise the questions of whether enough is gained in terms of information pooling. Admittedly, slow spatial variation of some parameters can conceivably cause estimation problems with shared parameters: even overlapping regions might end up with slightly different posterior estimates. If this is compensated for by manipulating volume fractions, resulting segmentations will, as a consequence, not be consistent between different grid (tile) placements. Practical experiments are needed to decide if this is really an issue.

5.3 Investigation of genu of corpus callosum

5.3.1 Materials and methods

This section examines the estimation of the parameters of the tissue dependent diffusion model with local sharing regions, in an ROI containing genu of corpus callosum placed manually in one of the datasets used in Chapter 3. Relevant data acquisition details can be found on page 57. Since performing a systematic investigation of anterior callosal fibres was not the aim of this section, we did not aim to ensure that the genu fitted in the ROI in its entirety. For the purposes of the shared parameter estimation the main ROI was subdivided into smaller, $4\times4\times4$ voxels sub-ROIs. Two such sub-divisions were used, with the same sub-ROI size, but shifted with respect to one another in the axial plane. This allowed the assessment of the consistency of estimation in the same voxels with different sub-ROI placements. Both sub-ROI grids are presented in Figure 5.1 (right-most column). In each sub-region, the shared estimation was performed in the joint space:

$$\left(S_{\mathrm{CSF}}, S_{\mathrm{GM}}, S_{\mathrm{WM}}, d_{\mathrm{CSF}}, d_{\mathrm{GM}}, d_{\perp}, d_{\Delta}, \{v_1^j, v_2^j, \theta^j, \phi^j, \varsigma^j\}_{j\in\mathrm{voxels}}\right),$$

where the tissue specific parameters $(S_{\mathrm{CSF}}, S_{\mathrm{GM}}, S_{\mathrm{WM}}, d_{\mathrm{CSF}}, d_{\mathrm{GM}}, d_{\perp}, d_{\Delta})$ are shared between all voxels, whereas volume fractions, fibre orientation angles and noise level $(v_1^j, v_2^j, \theta^j, \phi^j, \varsigma^j)$ are estimated independently for each voxel j. The usual sampling procedure was used, including initialisation described in Section 3.1.3 and the three-phased burn-in (see Section 2.3.2). Baseline results were provided by running the estimation independently in all voxels, according to the procedure detailed in Sections 3.1.2 and 3.1.3.

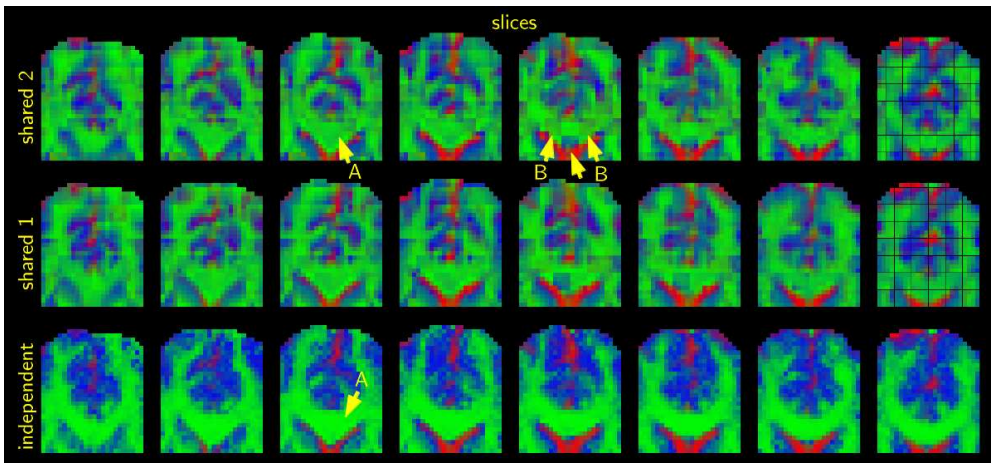

Figure 5.1: RGB-coded tissue type segmentations of the ROI containing genu of corpus callosum: independent estimation in single voxels (bottom row) compared to the shared estimation with different grid placements (middle and top rows). Sub-ROI division is revealed in the right-most column. Labels point to the features described in the text: low, inconsistent white matter volume fraction in the body of genu (A) and the border effects across neighbouring sharing sub-ROIs (B).

5.3.2 Tissue type segmentation

Figure 5.1 compares tissue type segmentations obtained with independent estimation to those with the sharing imposed using two different grid (sub-ROI) placements. We note that the sharing images show markedly lower quality; they appear noisy compared to the independently estimated maps. While white matter volume in the body of the genu (Figure 5.1/A) is consistently high with the single-voxel approach, the same cannot be said about either of the sharing experiments. In general, we observe more mixing of tissue types with the sharing method and fewer pure tissue voxels. A careful examination of the sharing grid reveals that the degraded quality of the sharing segmentation maps is partially due to the border effects between the sub-ROIs (5.1/B). Neighbouring voxels show a step change in the volume composition which seems to be explained by the general bias, within their respective sub-ROIs, towards particular tissue types: three example sub-ROIs highlighted in Figure 5.1/B have consistently higher grey matter volume fraction, at the expense of white matter. This bias affects whole sub-ROIs and as a consequence results from different grid placements are not consistent with one another.

The estimated volume fractions, separately for all three major tissue types, are presented in Figure 5.2. Sub-ROIs with low white matter content are clearly visible

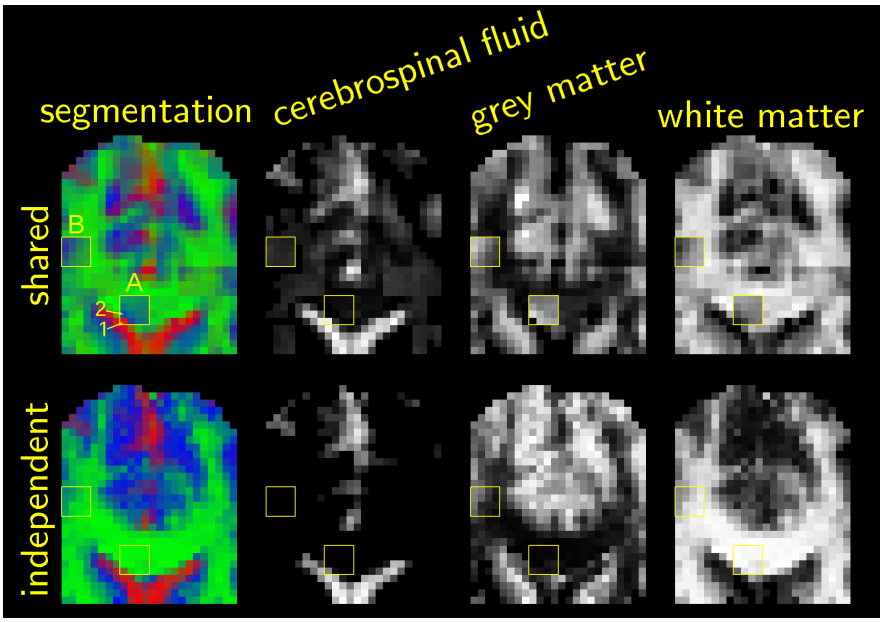

Figure 5.2: Tissue type segmentation estimated for all voxels independently and with parameter sharing in sub-ROIs. Two sub-ROIs outlined in yellow (A and B) show corrupt estimation when sharing of tissue parameters is imposed: underestimated white matter volume and spurious grey matter and (in sub-ROI B) cerebrospinal fluid.

in the maps obtained using the shared estimation, compared to the independent case. Two of these regions have been highlighted: in sub-ROI A, body of the genu of corpus callosum clearly contains a spurious grey matter compartment, whereas in sub-ROI B both grey matter and cerebrospinal fluid levels are elevated (though not equally). In general, it seems that anomalous cerebrospinal fluid volume can be found in the sub-ROIs where this tissue type is not present. On the contrary, in areas containing ventricles or sulci cerebrospinal fluid is strictly limited to these anatomically plausible spaces. Conceivably, the bias towards grey matter in some sub-ROIs as well as the presence of spurious cerebrospinal fluid can be explained by examining their tissue specific parameter values.

5.3.3 Tissue specific parameters

In order to discover the reason behind the corrupted volume estimation when sharing the tissue specific parameters in the sub-ROIs, we now examine mean posterior values of these parameters in selected sub-ROIs. T_2-weighted signal and diffusivity profiles of cerebrospinal fluid, grey matter and white matter are together parametrised by 7

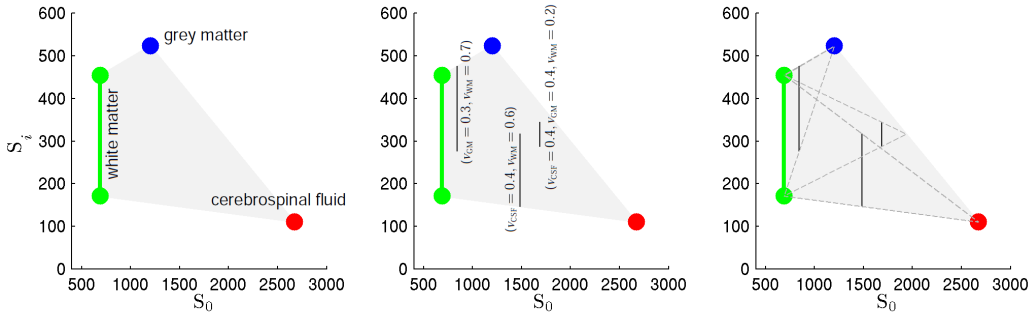

Figure 5.3: Signal-space plots: T_2-weighted signal on the horizontal axis, diffusion-weighted signal on the vertical axis. Markers corresponding to typical parameter values for different tissue types (see Table 2.1) are labelled in the left plot; grey area contains all possible signal values predicted by the model, before adding the effects of noise. Note that white matter produces a range of diffusion-weighted values: their exact positions along the vertical line depend on the relationship between the fibre direction and the spatial distribution of gradient orientations. Middle plot features noiseless signal from example voxels with partial voluming. Right plot presents the same data, adding the interpolation lines between the pure-tissue and partial volumed voxels.

quantities $(S_{\mathrm{CSF}}, S_{\mathrm{GM}}, S_{\mathrm{WM}}, d_{\mathrm{CSF}}, d_{\mathrm{GM}}, d_{\perp}, d_{\Delta})$; visualising and analysing their influence on the volume fractions is a non-trivial task. We therefore find it useful to plot the volumetric and non-volumetric parameters as well as the measured data directly in signal space.

Figure 5.3 shows examples of such plots, with T_2-weighted signal on the x-axis and diffusion-weighted signal on the y-axis. The key idea is to represent the parameter values by T_2- and diffusion-weighted signals predicted by the model for pure tissue voxels. For example, the values of parameters characterising cerebrospinal fluid can be visualised in this space as a point $(x = S_{\mathrm{CSF}}, y = S_{\mathrm{CSF}} e^{-b d_{\mathrm{CSF}}})$, corresponding to (noiseless) measurements from a pure cerebrospinal fluid voxel (a red dot in Figure 5.3). Similarly, grey matter parameters can be visualised by plotting the appropriate signal values predicted by the model for the voxel containing only this tissue type (a blue dot in Figure 5.3). A white matter voxel produces a single value of the non-diffusion-weighted signal, but many different values when diffusion weighting is applied. It can thus be represented by a vertical line segment in the signal space, from $(S_{\mathrm{WM}}, S_{\mathrm{WM}} e^{-b d_{\perp}})$ to $(S_{\mathrm{WM}}, S_{\mathrm{WM}} e^{-b(d_{\perp}+d_{\Delta})})$. Actual positions of the predicted measurements along this line depend on the angles between the true fibre directions and the set of diffusion-

sensitising gradient orientations. Given the values of the tissue specific parameters, we can also visualise predicted signal values for voxels with partial voluming (see examples in Figure 5.3, middle plot). Essentially, the noiseless signal values correspond to line segments in the signal space and are produced by interpolating between the values for the pure-tissue voxels (see Figure 5.3, right plot).

When plotting the measured data in relation to a set of parameter values (represented by predicted signal for pure tissue voxels) we can predict the tissue composition estimated by the tissue dependent diffusion model by (mentally) inverting this interpolation. Plotting and interpretation of the measured signal is more challenging than plotting predictions; it is worth remembering that data points measured in an actual MRI experiment differ from the predicted values because they are corrupted by Rician noise, and potentially imaging artefacts, and additionally because any model is only an approximate description of the diffusion in the brain tissue. Moreover, the T_2-weighted and diffusion-weighted data are measured independently and the number of volumes is typically different. For this reason it is inappropriate to represent the measurements as points in the signal space. What we can do instead is to draw a bounding box containing all the acquired data, which stretches from lowest to highest values of both T_2- and diffusion-weighted signal, thus representing the region of space from which all measurements originate. Such representation is used in Figure 5.4, which features data from two voxels from sub-ROI A (see Figure 5.2 for definition). The figure also shows estimated tissue specific parameters (in 'pure voxel' representation), marked by full circles, compared to typical values, represented by star symbols. We note that the two sets of parameters are strikingly different. Grey matter, in particular, shows dramatically decreased signal (both types), consistent with a drop in S_{GM} and perhaps a slight raise in d_{GM}. Corresponding values for cerebrospinal fluid are also changed, with reduced T_2-weighted signal (S_{CSF}) and diffusivity (d_{CSF}), evident through a decreased amount of diffusion-related attenuation. These changes in the tissue specific parameters and, consequently, signal predicted for different tissue type compartments lead to different interpretation of the data from the two example voxels. While using the typical parameter values voxel 1 can be classified as containing a mixture of white matter and cerebrospinal fluid, the values estimated jointly for the whole sub-ROI make it appear pure cerebrospinal fluid. Voxel 2, on the other hand, now appears to be composed predominantly of grey matter, whereas using typical signal values would put it firmly into white matter category. These interpretations are indeed confirmed by comparing independent and shared segmentations in Figure 5.2: in the second case (i.e. joint es-

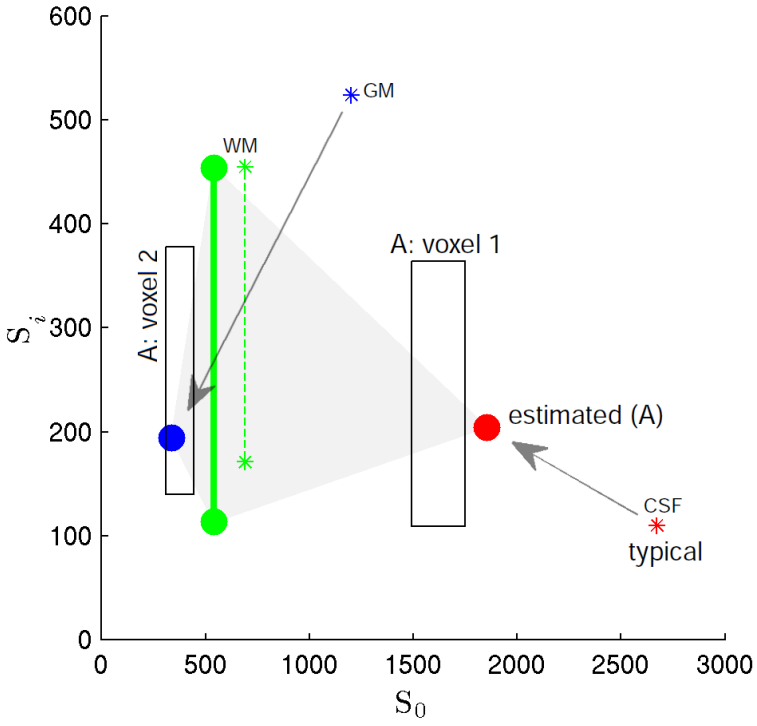

Figure 5.4: Signal-space plot featuring tissue specific parameters estimated for the sub-ROI A (see Figure 5.2) shown with full, coloured markers compared to typical values (from Table 2.1) marked with star symbols. Bounding boxes contain all measured values for voxels 1 and 2 from sub-ROI A; note that T_2- and diffusion-weighted signal is measured independently, so it is inappropriate to plot any single points that would suggest correspondence between the two. While under typical signal values voxel 1 could be classified as a white matter–cerebrospinal fluid mixture and voxel 2 as pure white matter, the values estimated on the basis of the whole sub-ROI impose a different interpretation, whereby voxel 1 contains almost exclusively cerebrospinal fluid and voxel 2 grey matter.

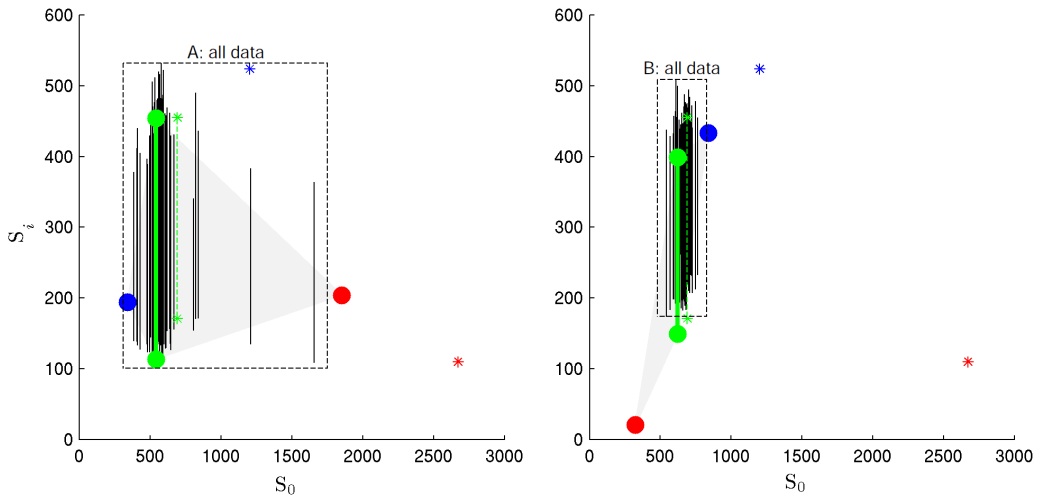

Figure 5.5: Signal-space plots of sub-ROIs A (left, see Figure 5.2 for definition) and B (right) showing data from all voxels (represented as bars). Dashed frames enclose all measured values for these sub-ROIs, indicating no outliers. Estimated parameter values are distant from their typical ranges, but provide strikingly good coverage of the observed data. The plots explain a shift away from white matter volume fraction in both sub-ROIs and the origin of the spurious grey matter (A and B) and cerebrospinal fluid (B) volumes.

timation) voxel 1 contains near-pure cerebrospinal fluid and voxel 2 a large spurious grey matter compartment.

The above examples show how changes in parameter values can explain systematic shifts in tissue-type segmentation obtained with a shared estimation procedure. Conceivably, different parameter values are arrived at in the neighbouring sub-ROIs, which explains the border effects seen in the segmentation maps in Figure 5.1. In order to investigate why shared estimation yields parameter values so distant from the regions of high prior probability and from values typically seen in brain tissue, the distribution of all relevant data must be examined. Specifically, this means all voxels comprising a given sharing region. In order to avoid clutter in the signal-space plots, we now represent data from each voxel by a vertical bar centred on the mean of its T_2-weighted signal ($x = \overline{S_0}$). Admittedly, this representation hides the non-diffusion variability, which might potentially be of interest. In order to ensure that there are no outliers that could affect the estimation process, we plot a (dashed) bounding box, similar to those from Figure 5.4, but now containing all measurements from all the sub-ROI's voxels. Figure 5.5 shows data from sub-ROIs A and B in this new representation, along with

typical and estimated parameter values.

We note that Figure 5.5 (similarly to Figure 5.4) correctly predicts a general shift in the estimated tissue volume in both sub-ROIs. In sub-ROI A (left plot), containing white matter from the body of the genu of corpus callosum and a small amount of ventrical cerebrospinal fluid in a handful of voxels, parameters obtained with the shared estimation lead to the appearance of spurious grey matter compartment and, in some cases, an enlarged cerebrospinal fluid compartment. In sub-ROI B, the variability in signal values that would typically be attributed to pure white matter voxels is partially explained by spurious grey matter and (to a smaller degree) cerebrospinal fluid compartments. This last observation is particularly striking and leads us to believe that the parameters for the redundant components (here grey matter and cerebrospinal fluid) can be moved to exotic regions of signal space in order to partially and erroneously explain the variability in the white matter signal intensities. Indeed, the regions of possible predicted signal values, coloured in grey, show remarkably good coverage of the observed data in both sub-ROIs, with little redundant space (empty grey areas, without bars) corresponding to possible, but unseen data.

This last observation hints at the reason why we observe parameter values that differ drastically from their typical values: the corrupted sub-ROIs contain no examples of pure grey matter or cerebrospinal fluid. Any such voxels would need to be explained by the model using the appropriate compartments, thus preventing them from degenerating and taking ownership of voxels in other regions of signal space. Additionally, the estimated parameter values can move far away from the region of high prior probability because the posterior distribution is dominated by the likelihood term. While a single voxel estimation is based on 71 datapoints (comprising 7 T_2- and 64 diffusion-weighted measurements), sharing the tissue specific parameters means that the likelihood becomes a product of contributions from all the voxels of a given sub-ROI. If no voxels are excluded by the brain mask, this means $71 \times 64 = 4544$ datapoints for a $4\times4\times4$ sharing sub-ROI. The likelihood argument suggests why shared estimation is affected more than the independent one. It also explains why the parameters defining tissue specific signal intensities dominate over the volume fractions: the former contribute more significantly to the likelihood and thus finding the region of high posterior requires that they are well aligned with the data, while the volumes play a role of the interpolating coefficients that can always be adjusted to the new signal values.

The notion that the presence of voxels containing near-pure grey matter and cerebrospinal fluid is necessary and sufficient for correct estimation of the shared tissue

specific parameters leads to the idea of using larger sharing regions. However, it is practically difficult to ensure that the required data would be present in such sub-ROIs before running the estimation. Excessively increasing the size of the sub-ROIs comes at a price, both in terms of computation time and the strength and extent of spatial parameter smoothing. For this reason, we shall investigate an alternative approach, which is to introduce additional constraints on the values of the shared parameters that would prevent the predicted signal from different tissue type compartments from becoming overly similar.

5.4 Constrained T_2-weighted signal priors

5.4.1 Variability of T_2-weighted signal in the brain

So far in this work the T_2-weighted signal variables $(S_{\mathrm{CSF}}, S_{\mathrm{GM}}, S_{\mathrm{WM}})$ were modelled using independent Gamma priors (see Figure 3.1). There are reasons to suspect, however, that they co-vary. The static B_0 field of the scanner is inhomogeneous due to the differences in magnetic susceptibility; the same is true for B_1 field, after adding the position-encoding spatial gradients. This *bias field* causes the amount of net magnetisation, M_0, to vary across the brain. While the T_2 time constant that governs the spin-spin relaxation depends on the tissue properties rather than location, the differences in net magnetisation might mean that the expected T_2-weighted signal for all tissue types varies from one location to another. At the same time, typical tissue specific T_2 values ensure that the relationship between the signal from different tissue compartments remains the same.

This co-variability could explain the low contrast between the different tissue types when considering large populations of voxels, without ruling out clear separability in each voxel. If correctly exploited, it could also aid the estimation by allowing simultaneous scaling of the T_2-weighted signal variables while preserving their separation. To this end, we shall now consider a joint prior distribution for all signal variables $(S_{\mathrm{CSF}}, S_{\mathrm{GM}}, S_{\mathrm{WM}})$, that takes into account their joint variability. We start from a simple set-up, whereby constraints on the allowed values of the signal are introduced in the form of the following inequalities:

$$S_{\mathrm{CSF}} \times 0.6 > S_{\mathrm{GM}} \quad \text{and} \quad S_{\mathrm{GM}} \times 0.7 > S_{\mathrm{WM}}.$$

Note that this implies that $S_{\mathrm{CSF}} \times 0.42 > S_{\mathrm{WM}}$. The resulting prior distribution is a product of truncated Gamma distributions, where the truncation is dependent on the values

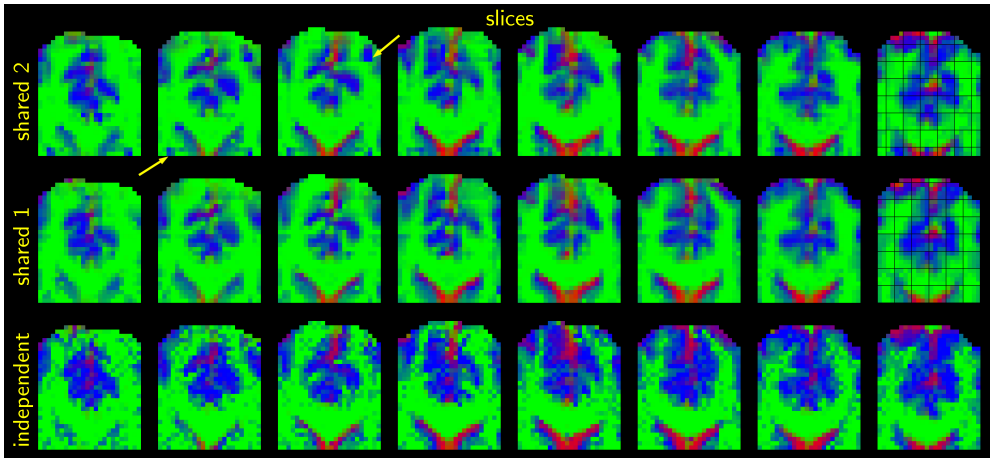

Figure 5.6: RGB-coded tissue-type segmentations of the ROI containing genu of corpus callosum: independent estimation in single voxels (bottom row) compared to the shared estimation with different grid placements (middle and top rows). Sub-ROI division is revealed in the right-most column. Shared estimation results compare favourably with those of 'free' estimation in Figure 5.1, even if unexpected, and possibly spurious, artefacts can still be spotted (see arrows).

of other variables, thus introducing dependence. Although some care was taken to adjust the scaling factors to our data (see Figure 5.8), their choice at present is entirely subjective. We review its impact and compare the constrained and unconstrained estimated signal values in Figure 5.8, below. In practice, the constraints are implemented by rejecting the Metropolis-Hastings jumps to the forbidden regions of space.

5.4.2 Tissue type segmentation

Parameter estimation in the ROI containing genu of corpus callosum was performed once again, this time using the new, constrained prior distributions over the T_2-weighted signal variables. Figures 5.6 and 5.7 present the resulting tissue type segmentations obtained with and without sharing the tissue specific parameters in sub-ROIs, as in previous sections. In stark contrast with results in Section 5.3, sharing parameters in the sub-ROIs (top and middle rows in Figure 5.6) results in spatially coherent segmentations, whereas independent voxel estimation (bottom row) produces markedly more noisy assignments, with seemingly random changes of the dominant tissue type in some voxels.

In comparison with the unconstrained, or 'free' estimation (see Figures 5.1 and 5.2), the new segmentations show less mixing of different tissue types. Functional

brain structures, such as white matter pathways and the cortex, now appear more homogeneous and coherent, particularly with parameter sharing; partial voluming is largely confined to the borders between these structures. We note a reduction in spurious grey matter volume on the edges of genu of corpus callosum, bordering cerebrospinal fluid filled ventricles. Examining the greyscale maps of the individual tissue type volume fractions in Figure 5.7 confirms the crispness of the new segmentation, the absence of spurious cerebrospinal fluid and a reduction in "suspicious" grey matter volume. As far as white matter is concerned, we observe fewer voxels with unexpectedly low volume of this tissue type. Such voxels can still be found in the crossing fibre regions, but their number and the severity of the white matter volume underestimation seems to be reduced with respect to the previous results.

Comparing the segmentations obtained by independent estimation and those with parameter sharing in Figure 5.6, the latter seem to contain more white matter overall, at the expense of grey matter. This shift does not seem excessive: the affected areas include spurious grey matter (volumes) in the crossing fibre areas, as well as the tissue belonging to minor white matter pathways and branches. These voxels contain white matter characterised by low anisotropy due to complex fibre architecture as well as partial voluming. They can be adequately explained by either grey or white matter component, even with T2-weighted signal constrains that limit the amount of excessive tissue mixing and encourage single component membership by ensuring the signal-space separation as explained in Section 5.4.3. This ambiguity is resolved by spatial information sharing in the sub-ROIs, which means that the two components must be able to account for data from a number of voxels, including pure white and grey matter voxels. As a result, the tissue specific parameters are less likely to overfit the data from any particular voxel of the sub-ROI. In such scenario the ambiguous white matter voxels are better described by the white matter parameters.

The number of sub-ROIs with visibly spurious, biased estimation in Figure 5.6 is greatly reduced compared with previous results. The segmentations obtained with different sub-ROI placements are now strikingly similar and in general the sub-ROI grid is not apparent. At the same time, some features of the maps, such as those marked by arrows in Figure 5.6, have to be treated with caution and the possibility that they are caused by the parameter estimation issues cannot be excluded. Additionally, some differences between the two sub-ROI placements can still be noticed and, as a consequence, we expect that the observed structure edges might in some cases be shifted with respect to their true position.

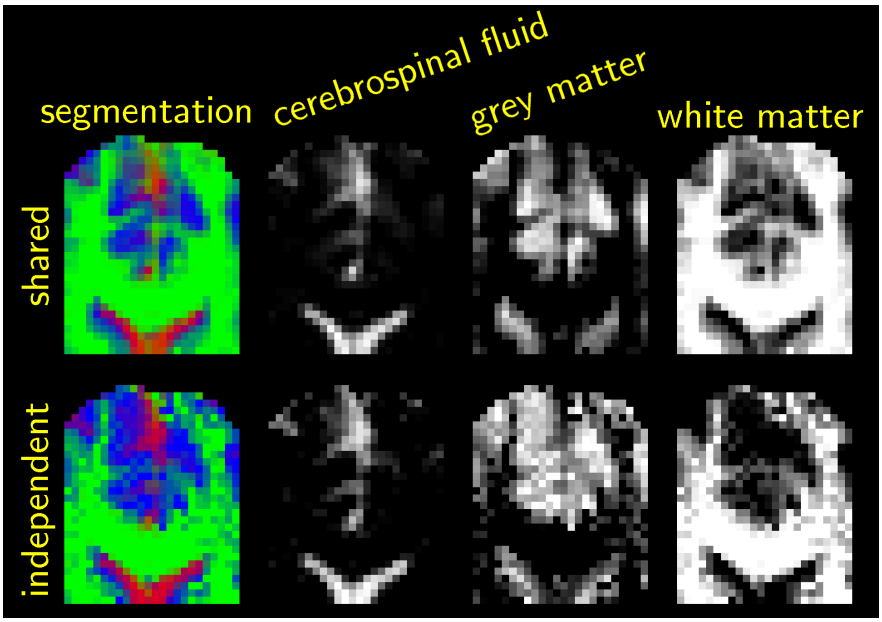

Figure 5.7: Tissue type segmentation estimated with constraints on the signal variables, for all voxels independently and with parameter sharing in sub-ROIs. Comparison with 'free' estimation in Figure 5.2 reveals a marked reduction in spurious volume of cerebrospinal fluid and grey matter.

5.4.3 Tissue specific parameters

What is the impact of the constraints on the estimated tissue type specific T_2-weighted signal parameters? Figure 5.8 presents the estimated values of these parameters plotted against one another in all possible pairs. We note that the constrained parameters occupy the same regions of space and do not appear to be overly restricted compared to the 'free' estimation. The variability away from the boundary of the acceptable region seems to be preserved, even if the boundaries appear to repulse the estimated parameter values. This gap is the effect of averaging over the posterior variability: the constraints apply to the individual samples and we present the mean posterior values. Overall, the effects of the constraints seem rather subtle, but even so they are sufficient to produce dramatic improvement in the segmentation results as seen in Figures 5.6 and 5.7.

In signal space (see Figure 5.9), the parameters for grey and white matter estimated with the constrained priors show slightly increased separation between the two tissue types. Considering the whole genu ROI, they are contiguously distributed (without a gap) and thus preserve the low contrast seen in the T_2-weighted images. On a voxel-by-voxel basis, however, single-component ownership of data is encouraged

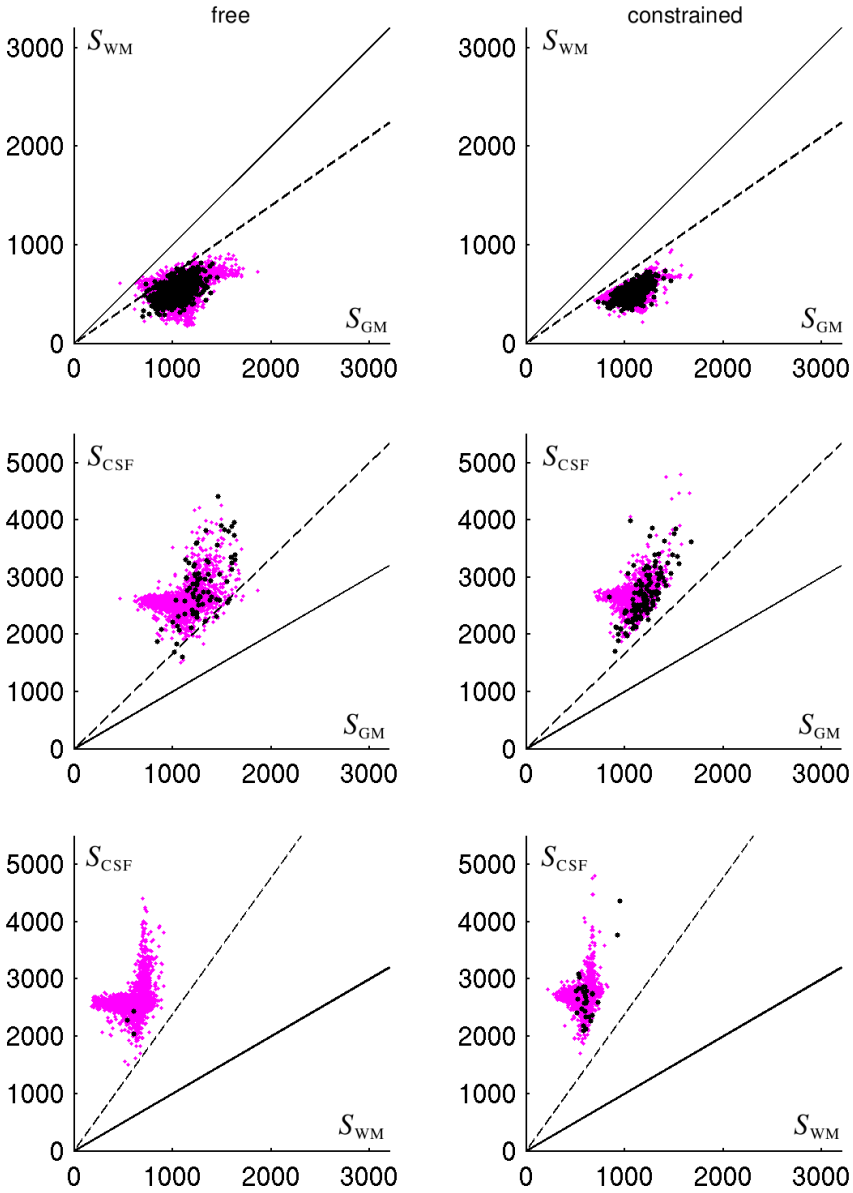

Figure 5.8: Tissue-specific T_2-weighted signal variables with independent prior distributions (left column) and with constraints on the relationship between the variables (right). Dashed lines mark the constraints applied, whereas solid lines correspond to identity. The results were obtained with independent estimation and each marker corresponds to one voxel. Black markers represent voxels containing at least 40% of each of the two tissue types plotted (e.g. $v_{WM} \geq 0.4$ and $v_{GM} \geq 0.4$ in the top row); other voxels are represented by magenta markers. Note that while the total number of voxels is the same for both estimation techniques, differences in the estimated volume fractions mean that more black markers appear when using constrained signal priors.

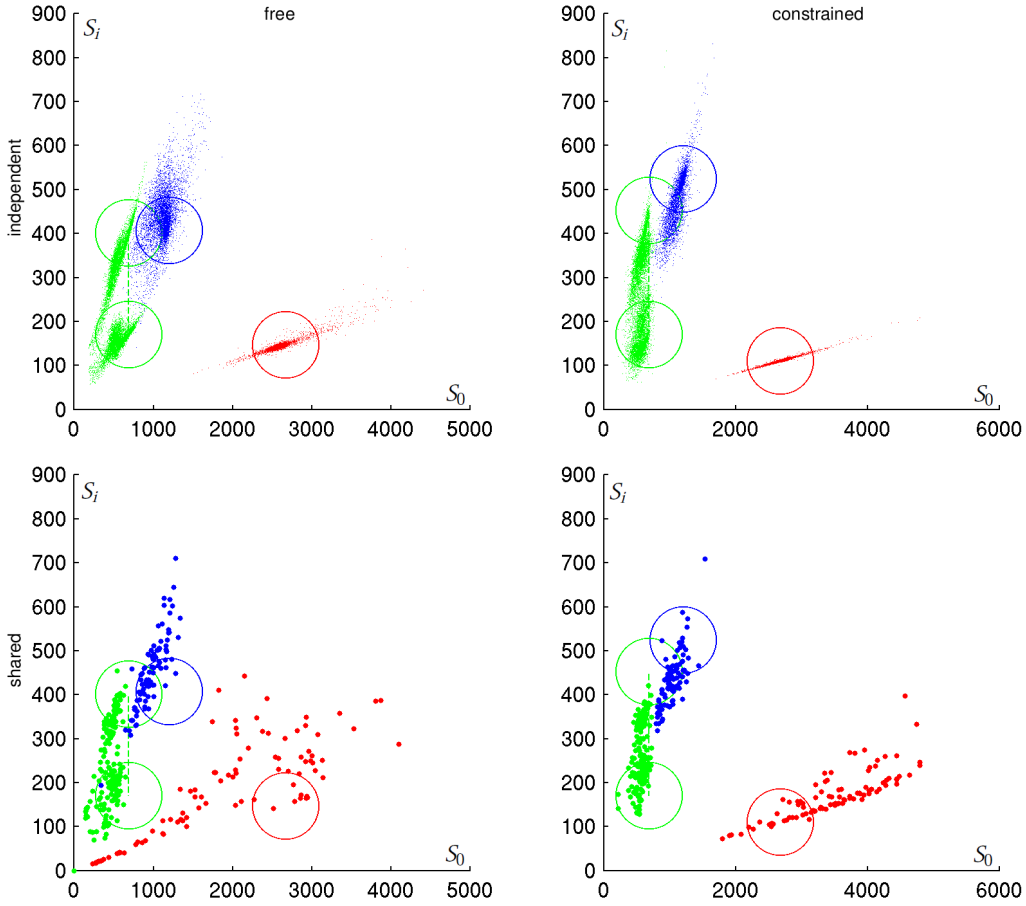

Figure 5.9: Signal space plots of the estimated tissue specific parameters in the pure voxel representation. 'Free' estimation with independent priors over the T_2-weighted signal is shown in the left column and with constraints in the form of inequalities described in Section 5.4.1 on the right. The top row presents the results from independent voxels' estimation, with each voxel represented by four dots (one red, two green and one blue). The bottom row presents the results obtained when sharing the signal and diffusivity parameters in the sub-ROIs; each set of markers corresponds to parameters values in one such sub-region. Coloured circles are centred on the values corresponding to the prior means, but do not represent the contours of these distributions (they also do not take into account the constraints on the signal variables).

and mixing is discouraged by enforcing the separation of the different compartments in signal space. Unconstrained signal parameters (see left column in Figure 5.9), on the other hand, seem to gravitate towards data and away from the prior distributions. This effect is particularly pronounced for cerebrospinal fluid, in sub-ROIs where no data from this tissue type is present to guide the estimation. In such circumstances, incorrectly low T_2-weighted signal and sometimes low diffusivity tend to be attributed to this component.

Comparing the typical and estimated values of T_2-weighted signal, particularly for grey and white matter, we come to the conclusion that the latter are consistently smaller. In other words, the 'typical' values appear to be underestimated. Conceivably, the procedure for estimating the priors over the T_2-weighted signal variables $(S_{\mathrm{CSF}}, S_{\mathrm{GM}}, S_{\mathrm{WM}})$ from data, described in Section 3.1.2 might introduce this type of bias in the presence of partial voluming effects. For example, the presence of voxels containing grey matter among the set used visually classified as white matter could lead to the overestimation of S_{WM}; similarly, S_{CSF} could be underestimated. In the case of grey matter, we cannot predict the direction of the shift, as it depends on which effects prevail — those of grey matter or those of cerebrospinal fluid (data from Figure 5.9 points to the latter). Since we typically observe very few pure grey matter and cerebrospinal fluid voxels, the hypothetical bias in these cases is potentially significant.

5.5 Diffusivity priors and their impact

The reader's attention is drawn to the fact that the circles corresponding to the expected values of the prior distributions in Figure 5.9 are not identically placed in the two columns. The vertical shift for the constrained, as opposed to 'free' estimation stems from the different diffusivity priors used. The 'free' estimation, and the work presented in the previous chapters, uses the distributions described in Chapter 2 (based on the values from page 37), whereas the priors for the constrained estimation are based on the values drawn from the literature and presented in Table 2.1 (page 45). We shall refer to the two sets of distributions as 'default priors' and 'literature priors'; the corresponding expected values of diffusivity shall be referred to as 'default' values and 'typical' values. Figure 5.9 makes it evident that in general the estimated parameter values are dependent on the placement of the prior distributions; the reminder of this section attempts to characterise the impact of the choice of the prior distributions over the diffusivity parameters.

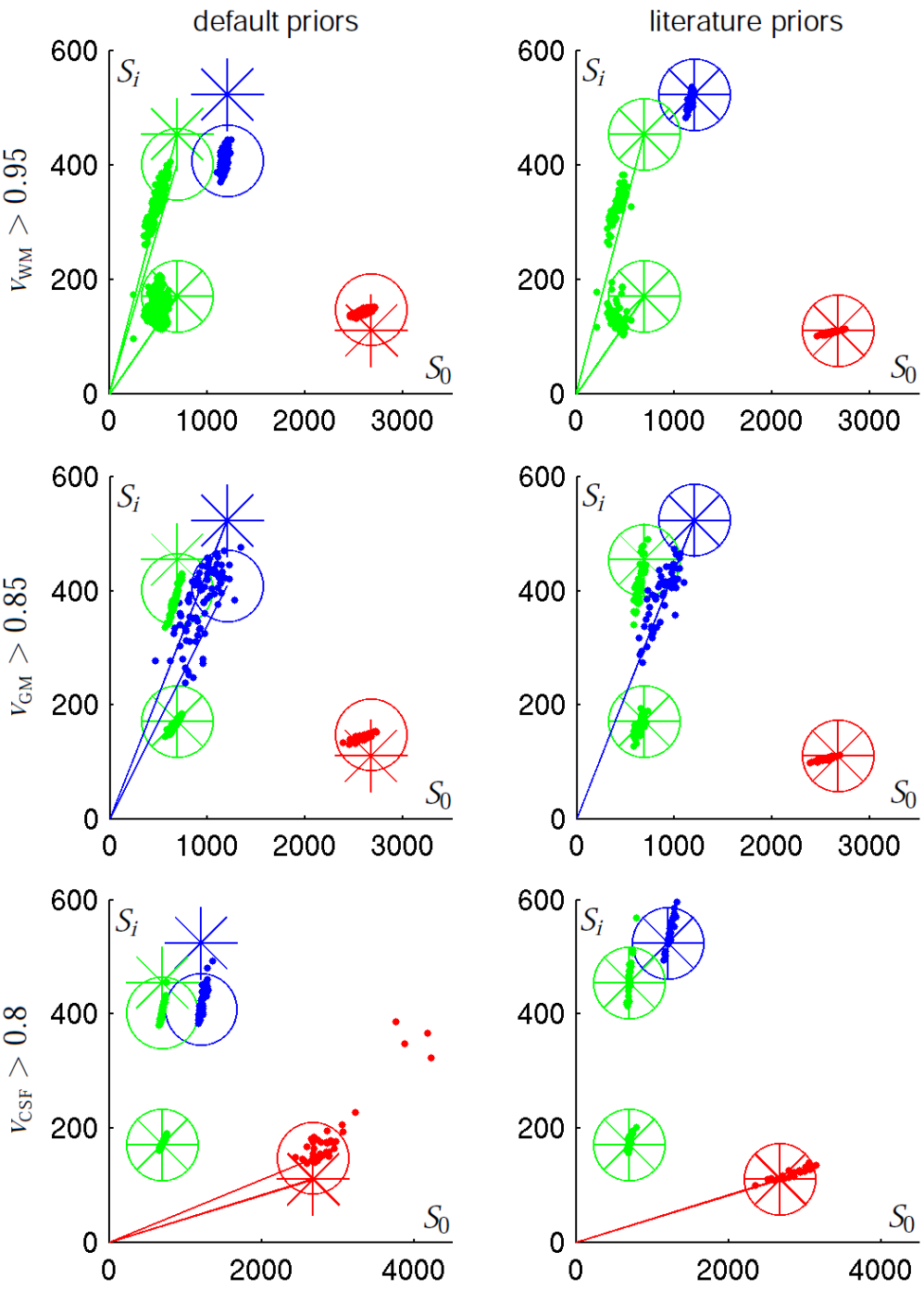

Figure 5.10: Signal space plots of the independently estimated tissue specific parameters in pure voxel representation: results in the left column were obtained using the priors utilised in Chapters 2, 3 and 4, while those in the right column were obtained using the priors based on the typical values from Table 2.1 (marked by star symbols in all plots). The rows feature results from voxels with high white matter (top), grey matter (middle) and cerebrospinal fluid (bottom) content. Each set of 4 markers corresponds to one voxel, as in Figure 5.9. Also similarly to that figure, coloured circles are centred on the values corresponding to the prior means. Lines radiating from the origin correspond to constant diffusivity values. Estimation appears data-driven for components supported by the data (see discussion in the text).

The top row of Figure 5.10 presents the estimated tissue specific parameters in a signal space representation, similarly to Figure 5.9, but this time only for voxels with high white matter content. We note that parameters characterising grey matter and cerebrospinal fluid, tissue types not supported by the data, are entirely defined by the placement of the respective prior distributions. Parameters specific to white matter, on the other hand, appear heavily dependent on the measured data. A similar situation can be recognised in the middle and bottom rows of Figure 5.10, featuring parameters estimated from voxels with high grey matter and cerebrospinal fluid content, respectively. The estimation appears data-driven in voxels where particular components are actually used, but dependent on the prior distribution where the corresponding volume fractions are low. That said, typical values (marked by star symbols in Figure 5.10) seem to better align with the estimated posterior means than the default values we use.

The evidence presented in Figure 5.10 suggests that the estimation of tissue specific parameters is not significantly biased by the placement of the prior distributions, in voxels where the relevant components are supported by the data. On the contrary, the model appears reasonably robust to the variation in the prior means. Unfortunately, the possibility that in some cases the estimated parameters are affected by a particular choice of priors cannot be excluded. Let us now consider how using priors based on the typical values from Table 2.1 instead of the default ones could potentially affect the results presented in Chapters 3 and 4 should such influence indeed occur. First of all, we note that the inequalities presented in Table 2.1, in particular $d_{\mathrm{CSF}} > d_{\parallel} > d_{\mathrm{GM}} > d_{\perp}$ hold for both sets of priors. Therefore any reasoning examining the hypothetical impact of partial voluming from the isotropic tissue types (grey matter and cerebrospinal fluid) on the AD or RD of white matter also holds regardless of which set of priors we consider as more reliable.

In Chapters 3 and 4 we have observed that the relationships between the diffusivity measures obtained with the diffusion tensor model and the analogous, fibre-specific quantities estimated with the tissue dependent diffusion model seem to be preserved at the level of the whole brain as well as particular pathways. An example result is provided by Figure 4.6, featuring group distributions of the whole brain, white matter specific averages of the relevant measures of diffusivity and anisotropy. Figure 5.11 reproduces these results, additionally marking the ‘typical’ and ‘default’ prior values or derivatives thereof (fibre FA, $\mathrm{FA_f}$ and fibre MD, $\mathrm{MD_f}$). The fibre-specific quantities of interest can be divided into two groups. In the first group, the gap between $\mathrm{FA_f}$ and fibre AD ($\mathrm{AD_f}$) and their diffusion tensor equivalents seems consistent with the

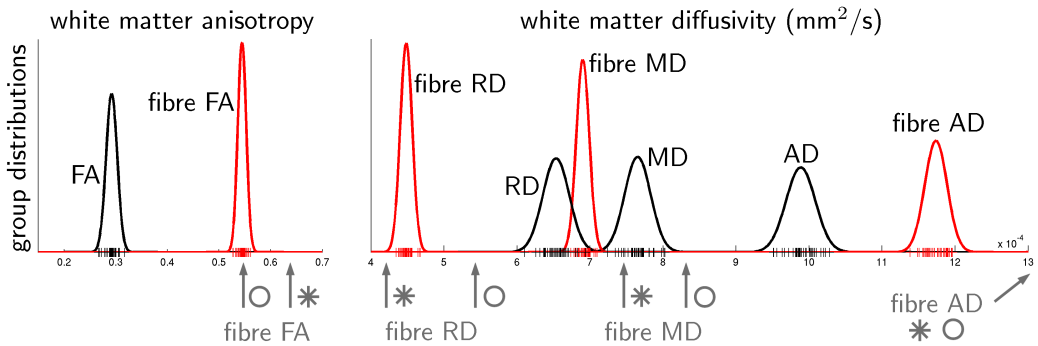

Figure 5.11: Whole-brain averages of anisotropy and diffusivity in white matter, based on Figure 4.6, page 96. Arrows below the plots indicate the typical values of fibre RD and fibre AD) found in the literature (marked by stars) along with means of priors used in Chapters 2, 3 and 4 (marked by circles). Fibre MD and fibre FA are derived using these values. Both 'typical' and 'default' values of fibre AD are equal to 1.4×10^{-3}mm^2/s.

estimates from the two models being (hypothetically) 'pulled apart' when using default priors, because

$$\text{FA} < \text{estimated FA}_\text{f} \approx \text{default FA}_\text{f} \quad \text{and}$$
$$\text{AD} < \text{estimated AD}_\text{f} < \text{default AD}_\text{f}.$$

If typical rather than default prior distributions were used, however, this effect would be either exactly the same (for AD_f) or even stronger (FA_f). Variables from the second group, fibre RD (RD_f) and MD_f, are both smaller than their diffusion tensor counterparts. This, however, cannot possibly be the effect of the prior distributions we use, since they favour more similar, not more distant values. In other words, the estimates obtained with the tissue dependent diffusion model are more extreme, more separated from the diffusion tensor quantities than the priors would suggest:

$$\text{estimated RD}_\text{f} < \text{default RD}_\text{f} < \text{RD} \quad \text{and}$$
$$\text{estimated MD}_\text{f} < \text{MD} < \text{default MD}_\text{f}.$$

Again, using the literature priors instead of the default prior distributions could potentially cause the divergence to be stronger, not weaker than observed. The above arguments suggest that the results presented in earlier chapters are reliable and that they are unlikely to be negatively affected by using literature priors instead of the default ones.

5.6 Conclusions

In this chapter we have considered the variability of the tissue specific T_2-weighted signal and diffusivity in the brain and how this knowledge can be harnessed to further improve and stabilise the estimation of the tissue dependent diffusion model. In particular, we have looked at the possibility of locally pooling the information about the quantities of interest. To this end, we have implemented a simple parameter sharing model in small regions that can be scaled to larger ROI estimation, such as the whole brain, by tiling the necessary volume with these small sub-ROIs.

Our simple sharing model was tested on an ROI containing genu of corpus callosum. The obtained tissue-type segmentations were found to be highly variable and generally low quality. The reasons for this poor performance were examined, in particular by plotting the estimated parameter values and data together in the signal space. This allowed us to hypothesise that the main reason behind the segmentation failure was the lack of representative examples from all tissue types in some sub-ROIs and the tendency of the unused components to be moved towards the data (in signal space) in order to better explain the residual variability. For example, it was found that the grey matter component can be moved close to the typical white matter region, resulting in a mixed (estimated) volume composition of some voxels that are clearly white matter. We believe that the above observations also shed light on the deficiencies of the original, independent estimation.

In order to prevent the different tissue terms from becoming overly similar, we have decided to introduce non-independent prior distributions over T_2-weighted signal. Such distributions can conceivably be justified in practice by considering the variations in the available net magnetisation due to the inhomogeneous magnetic susceptibility. Estimation with the new, constrained priors showed marked improvements with respect to the previous results, providing crisp, plausible tissue type segmentations, particularly with the sharing of the tissue parameters. The sharing results are still not ideal in that they occasionally show unexpected, possibly spurious features, but they nevertheless appear to be a step in the right direction.

Lastly, we have examined the influence of the choice of the priors distributions over the diffusivity parameters and concluded that this choice mainly affects the estimation in voxels where the corresponding volume fractions are low and thus the components are not supported by the data. We have also revisited the reasoning and results of Chapters 3 and 4 in order to evaluate the hypothetical impact of using an alternative set of

priors, based on the values found in the literature and presented in Table 2.1. It seems that using these priors, rather than the default ones (based on values from page 37) could make the results slightly stronger, in some cases increasing the separation between the quantities obtained with the diffusion tensor model and their white matter specific equivalents from the tissue dependent diffusion model.

Chapter 6

Discussion and future work

Diffusion MRI holds the potential to probe aspects of the human brain unattainable with other MRI modalities, but it also suffers from a unique set of issues. In particular, its spatial resolution is lower than that of many other methods which causes many acquisition voxels to contain more than one tissue type, a situation known as partial voluming. The lack of explicit representation of partial volume effects corrupts the results of the currently used methods reviewed in Chapter 1, most prominently the diffusion tensor model, adding unwanted noise to the commonly used diffusion parameters, such as FA and MD. At the same time, the volumetric information is only indirectly estimated through tractography. Addressing the above issues is the main motivation for this work: the tissue dependent diffusion model we have proposed directly describes the three main tissue types using Gaussian diffusion compartments parametrised by appropriate tensors. Our method was tested on a range of synthetic and human datasets in Chapters 2–3, leading to the conclusion that it reliably produces anatomically plausible tissue type segmentations and provides more accurate measures of water diffusion in brain tissue compared with the diffusion tensor model. We also applied it to a study of brain changes in adulthood and early ageing in Chapter 4. In Chapter 5, we have shown that the accuracy and reliability of the model's estimates can be further improved by applying reasonable (if somewhat arbitrary at present) constraints on the co-variability of the T_2-weighted signal for different tissue types and by sharing the tissue specific parameters between the neighbouring voxels.

While the effects of partial voluming on the parameters describing tissue properties are greatly alleviated with our method, there is definitely room for further improvement. The model's expressive power would be greatly increased by adding one or more white matter compartments, thus allowing the modelling of crossing fibres. Better spa-

tial integration of the estimated parameters, on the other hand, could facilitate more accurate and meaningful comparative analysis of white matter. Lastly, approximate parameter estimation methods could reduce the computational cost of the parameter estimation and seem necessary when extending the current model, particularly if spatial dependencies are introduced. In the remaining sections we explore how the above issues could be approached; we start, however, by putting the tissue dependent diffusion model in a broader context of related work, some of which we have already mentioned in the preceding chapters.

6.1 Alternative approaches to segmentation

To our knowledge, the tissue dependent diffusion model is the only method to date that segments the volume fractions of all three major tissue types, based on an explicit forward model of diffusion, and supplies diffusion metrics that improve on their diffusion tensor equivalents by filtering out the isotropic partial volume effects. However, a number of methods have attempted to segment diffusion MRI data into different tissue types; they can be roughly divided into three groups.

The first category of segmentation methods attempt to classify all voxels based on the diffusion tensor eigenvalues, MD, FA and sometimes other measures of anisotropy. These quantities, rather than the raw diffusion-weighted data, become the input of the segmentation algorithms. An early example is provided by the work of Cercignani et al [31], who fit a mixture of isotropic Normal distributions to a joint, whole brain FA/MD histogram. The estimated mixing proportions then serve as probabilities of the three main tissue types and the classification is performed by picking the most probable class independently in each voxel. All acquisition voxels are thus exchangeable under this model. More sophisticated approaches also account for the fact that the neighbouring voxels often belong to the same tissue type given the scale of the brain's main functional structures. This spatial dependence is usually implemented using MRF methods. For example, Liu et al [73] perform seven separate segmentations using different quantities: ADC and diffusion tensor eigenvalues to separate cerebrospinal fluid based on its high diffusivity; and various measures of anisotropy (including FA) to single out white matter. In each case segmentation is performed using a hidden MRF in conjunction with an EM procedure which updates the tissue specific values of each segmented quantity in an unsupervised manner. All the obtained maps are then fused together in a two-step process to yield the final three-tissue segmentation. Recent work of Ku-

mazawa et al [71] presents a more advanced approach, which is particularly relevant from the point of view of our own work. The authors manage to estimate the volume fractions of the three main tissue types, rather than providing a crisp, categorical tissue type classification like the previous methods do. The segmentation is based on MD, FA and diffusion tensor eigenvalues and uses a spatial MRF as a prior distribution over the volume fractions.

The above methods produce plausible tissue type segmentations, confirming our belief that the necessary tissue contrast is indeed present in the diffusion MRI data. It is unclear whether substantial amount of information is lost by performing the segmentation using the diffusion tensor eigenvalues and various derived metrics, rather than the raw data. The methods lack an explicit model of diffusion and the authors do not show the tissue specific diffusivity and anisotropy parameters they obtain, although it seems that such parameters could be easily retrieved. It would be interesting to compare these quantities, along with the volume fractions estimated by Kumazawa et al, with the results from the tissue dependent diffusion model. An unquestionable advantage of the above methods over the framework presented in this work is the fact that they use optimisation techniques to produce their segmentations, thus making them much faster compared to the sampling procedure we use.

An alternative category of segmentation methods are based on forward models of diffusion and aim to alleviate cerebrospinal fluid “contamination”. This group is represented by the free water elimination approach by Pasternak et al [90], who use two Gaussian diffusion compartments in order to obtain rectified FA values in the presence of cerebrospinal fluid. The lack of prior information about the typical diffusivity values of white matter means that their model suffers from parameter indeterminacy similar to that outlined in Section 2.1.2. In order to stabilise the parameter estimation the authors use spatial smoothing of the tensor eigenvalues, eigenvectors and volume fractions. Although the authors claim that the smoothing process preserves the spatial variability between the tensors from neighbouring, but different structures, we find that the bias introduced by their approach is potentially stronger and more unpredictable than using simple prior distributions over the model’s parameters. Unfortunately, partial voluming of between white and grey matter is not modelled with the free water elimination framework and continues to corrupt the estimated tensor metrics.

The third category of segmentation methods use streamline tractography to indirectly estimate the volume of the white matter pathways. For example Vos et al [118] approximate the volume of (sections of) tracts by a number of voxels traversed by the

tractography streamlines and suggest using this estimated volume as a co-variate in any analysis based on the diffusion tensor model. A rather more precise approach has been proposed by Calamante et al [28, 27, 29], who use track-density to obtain super-resolved maps of white matter. Here, the whole-brain tractography serves to create an alternative, approximately continuous representation of the brain's white matter that can then be discretised at a superior resolution. The authors suggest that track-density maps are unaffected by some of the issues encountered by the tractography methods, such as spurious branches and difficulty in following non-dominant pathways, because the ability to exploit local, rather than global connectivity is utilised by this method. They do, however, seem prone to premature pathway truncation: it has to be remembered that the tractography itself is limited by the accuracy of the FA, which serves as a stopping criterion and can strongly influence the final results. While the authors are able to obtain plausible-looking images at a resolution unattainable with other methods using diffusion MRI data (0.125mm isotropic resolution compared to the original 2.3mm), they admit that their results are only indirectly related to actual white matter volume and cannot be used in its place. At the moment, it seems that the track-density mapping offers a new and potentially useful visualisation tool, complementary to the volume estimation techniques.

In comparison with the diffusion tensor based segmentation methods described above, the contribution of our work is to approach the three tissue segmentation problem using a realistic forward model of diffusion explicitly incorporating the partial volume effects, the tissue dependent diffusion model. This allows us to obtain the fibre specific measures of diffusion alternative to those produced with the diffusion tensor model, and less affected by partial voluming. The free water elimination framework seems to follow a line of work convergent with ours, but only goes half-way as it fails to account for the partial voluming from grey matter. Other multi-tensor approaches, perhaps most prominently the ball-and-stick model and its extensions [16, 15], feature as superficially similar form of the diffusion equation, but it is unclear how the diffusion terms they use (particularly those with the "stick" tensors) relate to different physical compartments of a voxel. Often, these models also compromise the realistic description of the diffusion process by introducing arbitrary constraints and sharing the parameters between the different compartments, something we have strived to avoid.

As mentioned in Section 3.2.3, an alternative to segmenting diffusion-weighted volumes directly is to make use of structural MRI modalities, such as T_1-weighted images, that benefit from higher spatial resolution compared to the diffusion data and

sometimes from improved contrast between certain tissue types. Much work has been done to segment such intensity images, either separately or combining the information from different volumes in a multi-modal segmentation. One example is FAST ([122], see also Section 3.2.3, Figure 3.8); another popular tool is the Statistic Parametric Mapping [4], which estimates the probabilities of the different tissue types in every voxel by combining a mixture model for the measured signal intensity with an anatomical plausibility prior. The segmentations obtained on the basis of the structural (intensity) MRI images are typically used as white matter masks after registeration to the diffusion space. This thesis follows a different approach, allowing to estimate the partial volumes of the major tissue types directly from the diffusion data.

It would be potentially useful to combine the high-resolution segmentation results for other modalities with the tissue type volumes estimated on the basis of the diffusion-weighted data. Unfortunately, such combination is not straightforward. Some methods provide tissue type probabilities for each voxel, which are related, but not directly convertible to volume fractions. Even if a method does supply the partial volume estimates of different tissue types, it remains unclear what weighting they should be given compared to the diffusion-based volume fractions. A simple way in which a segmentation performed on a high resolution intensity images and registered to the diffusion space could be used to guide the volume estimation with the tissue dependent diffusion model proposed in this thesis is by computing an informative prior distribution over the volume fractions (as opposed to uninformative priors used at the moment). A more principled approach would be to propose a joint framework where the intensity of the high resolution MRI volumes, such as T_1-weighted volumes, would be directly related to the partial volumes estimated for the diffusion-weighted image through additional likelihood terms. Such solution would then enable the parameter estimation to be informed by the data from all available modalities, at the cost of added computation time due to the increase in the number of parameters.

6.2 Modelling multiple white matter fibres

The tissue dependent diffusion model only incorporates one white matter compartment and thus crossing fibre regions present a major challenge to its accuracy (causing white matter volume fraction to be spuriously low) and limit its applicability (alternative methods need to be used to obtain the fibre orientations for tractography). While many approaches to estimating multiple white matter fibre orientations have success-

fully been applied to diffusion MRI data (see Sections 1.2.2 and 1.2.3), they usually fall short when it comes to realistic, quantitative description of the diffusion process: the parameters that control the signal fit of these models are typically not useful characteristics of the water diffusion in white matter. While modelling multiple fibre directions is one of the priorities for the further development of our method, it presents significant and so far unresolved difficulties.

It is conceptually easy to extend the diffusion model formulated in Section 2.1 by adding one or more terms described by cylindrical tensors to Equation 2.2. It has to be kept in mind, however, that two crossing pathways might in general have different diffusion characteristics, a feature we would like to account for in our model. As a consequence, each additional term would be parametrised by a volume fraction v as well as up to 3 tissue specific parameters and would thus greatly aggravate the indeterminacy issues described in Section 2.1.2. Another, perhaps slightly easier, issue to be addressed is the identifiability of different white matter components. Usually, care needs be taken to prevent two (or more) white matter components from modelling the same white matter fibre; the number of white matter fibres vary from voxel to voxel and redundant components should be eliminated, perhaps by using the reversible jump methodology. Additionally, in voxels where two or more fibre families are present, the white matter components might swap during the sampling. As a result, the samples representing the crossing white matter pathways would be mixed between the components of the model. In our case this problem would be exacerbated because each such component would possess its own set of tissue parameters and care would need to be taken to obtain sample sets consistent with different real fibre orientations.

In the light of the above considerations, particularly to ensure the determinacy of the extended model, it seems unavoidable that adding more white matter compartments would require more information than is contained in data from single voxels. Simple spatial pooling of information, albeit helpful in stabilising the estimation in the one-fibre model as shown in Chapter 5, is in this case not sufficient. The reason is that the sharing of the white matter specific parameters would need to be performed along the pathways, necessitating a more comprehensive approach that would use the orientation information to guide the sharing. A conceivable, simple set-up might involve identifying and keeping track of sets of voxels (and their specific white matter components) for which the parameters would be shared, based on the least curvature between the estimated fibre orientations.

6.3 Spatial integration

Comparative analysis of the magnitude and anisotropy of water diffusion requires that the corresponding voxels or clusters of voxels are identified. A simple registration of MRI volumes into the same space is, in this case, insufficient because of the individual variability in the topology of the brain. TBSS addresses this issue by finding the white matter skeleton which establishes voxel-level correspondence [99]. Another powerful approach is to identify equivalent neural structures, such as entire white matter pathways, whose properties can readily be compared directly. Examining larger, anatomically meaningful regions also aids understanding and interpretation of the results, unlike in TBSS, where the automatically identified clusters need to be labelled manually when presenting the results, as is the case in the studies cited in Chapter 4 [17, 26]. Potentially problematic interpretation aside, fine-grained investigation promises high spatial precision, but it is prone to noise effects and requires rigorous treatment of the inevitable multiple comparisons (as for example in TBSS [99]). The analysis of gross anatomical structures, on the other hand, is potentially more statistically robust (because it uses more data), but runs the risk of averaging over genuine local variability and hence not detecting focal changes inside a given ROI.

Theoretically speaking, detecting structural changes should be easiest with methods that integrate the results over the affected area as precisely as possible, because they use the greatest amount of relevant, informative data without introducing irrelevant, noisy observations. However, it is not clear which spatial scale is optimal for performing this kind of integration, given that different segments of the same pathway may experience varying degrees of degeneration [39], or even show different patterns of change [26], thus hinting at different prevailing mechanisms of pathology. The existence of spatial gradients of change (see Section 4.1.3) suggests that, in some cases if not universally, age-related change might be region- rather than pathway-specific. At the same time, investigating specific pathways remains attractive as it can easily be linked to the function played by the grey matter areas they connect. This functional view raises a question of what is the best indication of the health of a particular connection. It seems that for some types of pathology, such as demyelination, the cumulative effects averaged over the pathway's entire volume need to be taken into account, whereas for others (e.g. acute injury) finding the most severe damage at some point along the tract is relevant.

Since the appropriate spatial scale of investigation is rarely known a priori, it seems

sensible to adopt a mixed approach where a number of different spatial scales are examined in an exploratory manner. One example of such an exploration can be found in Chapter 4, where the brain is examined as a whole before looking in greater detail at selected major white matter pathways to discover how they are affected by early ageing. Complementary low-level results obtained with TBSS can be found in the studies cited in the same chapter [17, 26]. Other types of investigation are also conceivable, for example explicitly examining global patterns of diffusion change that connect the brain changes to the underlying physiology, such as the anterior-posterior gradient [25, 39, 75, 17, 26]. Such an investigation would involve considering the estimated diffusion metrics from all white matter voxels, regardless of which tract they belong to, and performing a regression analysis with respect to their position along the anterior-posterior direction. A similar approach could be used to examine other global hypotheses; for example, it is known that the brain torque (and other asymmetries) affects the geometry of parenchyma, but it remains unclear whether it also influences its diffusion properties. These simple, but potentially interesting approaches could complement the standard methods, such as automatic cluster detection in TBSS and the use of pathway masks obtained with tractography.

Further improvements of the tractography-based method are also conceivable. In our work, binary tract masks are produced by thresholding the probability of connection to the seed point and serve to select the sets of voxels used in further analysis. Currently, liberal tractography masks are preferred to conservative ones as far as the isotropic partial volumes are concerned, because our method explicitly models their effects. The reverse situation, where some voxels containing white matter are excluded due to low anisotropy (thus meeting the stopping criteria), is not desired. On the other hand, in the case of crossing fibres we rely entirely on the tractography algorithm to select only the voxels belonging to the fasciculus of interest and not to other pathways; we have no tools to discard the incorrectly segmented white matter voxels, which is why at present we consider the estimation of tract volume as unreliable. Crucially, tractography only uses the white matter fibre orientations; our model, on the other hand, estimates the volume of the three major tissue types in each voxel, but makes no use of the orientations beyond the voxel level.

It seems that joint estimation of the volume fractions of white matter along with the fibre orientations, beyond a single-voxel level, might hold the key to segmenting the whole pathways, including the segments crossing with other tracts. Conceivably, tractography and local estimation of the parameters of a diffusion model could be

run jointly, as demonstrated by Jbabdi et al [59]. Alternatively, white matter volume fractions in the crossing fibres regions could be obtained using a multi-fibre diffusion model with selective sharing of white matter parameters guided by the local orientation and curvature of the fibres, outlined in Section 6.2. Segmentation of the entire pathways could potentially be performed after or during the parameter estimation. It has to be acknowledged the development of such a framework is a difficult task. In particular, it seems that standard random field methods are less than ideal when it comes to modelling volume fractions in the presence of partial voluming or diffusivities, which potentially undergo both gradual (within the same structure) and abrupt (across different structures) changes. A more promising direction of research might use a combination of the statistical shape models (see [53] for review) for volume fractions and local similarity models (such as MRFs) within the limits of the structures segmented in this way.

6.4 Approximate parameter estimation

An important factor limiting the use of the tissue dependent diffusion model is the time needed to run the parameter estimation. The high computational load is caused by a relatively large number of parameters needed for the realistic description of partial volume effects: 12 parameters per voxel or approximately 2,000,000 for an entire brain volume. Fortunately, single voxel estimation is trivially amenable to distributed computation. The same is true for the simple sharing method in sub-ROIs presented in Chapter 5, but not for more sophisticated approaches based on random field methodology that prevent distributed computation by introducing dependencies across the entire brain volume. A prerequisite to deploying any such sharing methods is thus the development of approximate parameter estimation methods as an alternative to sampling. With this regard, variational methods present a promising avenue of future research.

6.5 Conclusion

In this work, we have shown that reliable estimation of both volumetric and tissue specific parameters is possible in a framework that directly models partial volume effects: the tissue dependent diffusion model. Fibre specific diffusivity indices obtained with our method promise a much needed improvement over the diffusion tensor derived metrics, such as FA and MD. More work is needed to utilise in a meaningful way the

volume fractions of the different tissue types we estimate (through improved spatial integration). Extending the diffusion model to enable the modelling of crossing fibres is going to involve significant effort to ensure that the parameter estimation is robust in the face of the model's indeterminacy. It will also require the development of more efficient estimation methods in order to overcome the potentially prohibitive computational cost. Even in its current form, however, our method is a useful tool to study white matter.

List of Abbreviations

Abbreviation	Meaning
AD	axial diffusivity
ADC	apparent diffusion coefficient
CSF	cerebrospinal fluid
EM	expectation-maximisation
EPI	echo planar imaging
FA	fractional anisotropy
FAST	FMRIB's automated segmentation tool
FMRIB	The Oxford Centre for Functional MRI of the Brain
FSL	FMRIB software library
GM	grey matter
MCMC	Markov chain Monte Carlo
MD	mean diffusivity
MRF	Markov random field
MRI	magnetic resonance imaging
pdf	probability density function
RD	radial diffusivity
RF	radio frequency
RGB	red-green-blue
ROI	region-of-interest
TBSS	tract-based spatial statistics
VBM	voxel-based morphometry
WM	white matter

List of Publications

Peer-reviewed conference posters

- Jakub P. Piątkowski, Mark E. Bastin, Amos J. Storkey, “Estimating white matter tract volume in partial volume voxels with diffusion MRI” at the *International Society for Magnetic Resonance in Medicine* (ISMRM) 17th International Meeting and Exhibition, 2009.

- Jakub P. Piątkowski, Mark E. Bastin, Amos J. Storkey, “Discovering white matter structure beyond anisotropy mapswith diffusion MRI” at the *International Society for Magnetic Resonance in Medicine* (ISMRM) and *European Society for Magnetic Resonance in Medicine and Biology* (ESMRMB) Joint Annual Meeting, 2010.

Other papers and posters

- Jakub P. Piątkowski, Mark E. Bastin, Amos J. Storkey, “Probing the Brain‘s White Matter with Tissue Dependent Diffusion Model” at the *Scottish Imaging Network: A Platform for Scientific Excellence* (SINAPSE) Annual Scientific Meeting, 2012.

- Jakub P. Piątkowski, Amos J. Storkey, Mark E. Bastin, “Segmenting white matter structure from diffusion MRI” at the *International Conference on Machine Learning* (ICML) workshop on Statistics, Machine Learning and Neuroscience, 2012.

Appendix A

Full tract specific results

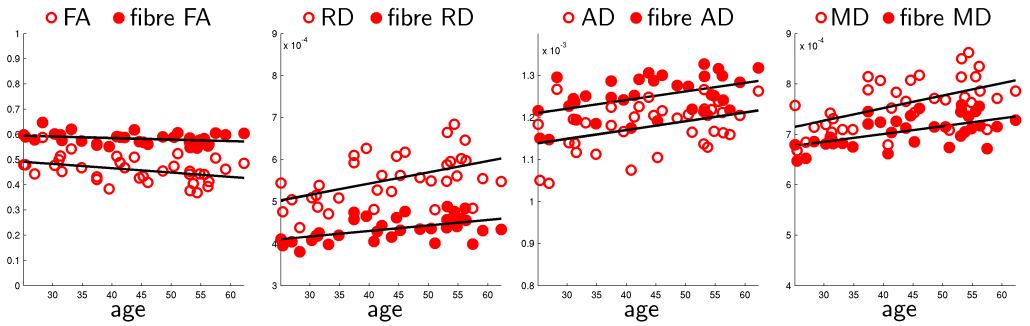

	FA	RD	AD	MD
p-value	**0.022**	**0.0022**	**0.017**	**0.0006**
standard error	0.0455	5.18×10^{-5}	5.34×10^{-5}	4.19×10^{-5}
slope (per year)	-0.0017	2.7×10^{-6}	2.1×10^{-6}	2.5×10^{-6}
trend	↘	↗	↗	↗

	fibre FA	fibre RD	fibre AD	fibre MD
p-value	0.083	**0.0017**	**0.0044**	**0.00038**
standard error	0.0223	2.47×10^{-5}	4.3×10^{-5}	2.53×10^{-5}
slope (per year)	-0.00062	1.3×10^{-6}	2.1×10^{-6}	1.6×10^{-6}
trend	none	↗	↗	↗

Figure A.1: Measures of water diffusion in genu of corpus callosum. Plots: age differences and trends the across the cohort. Table: summary of regression measures.

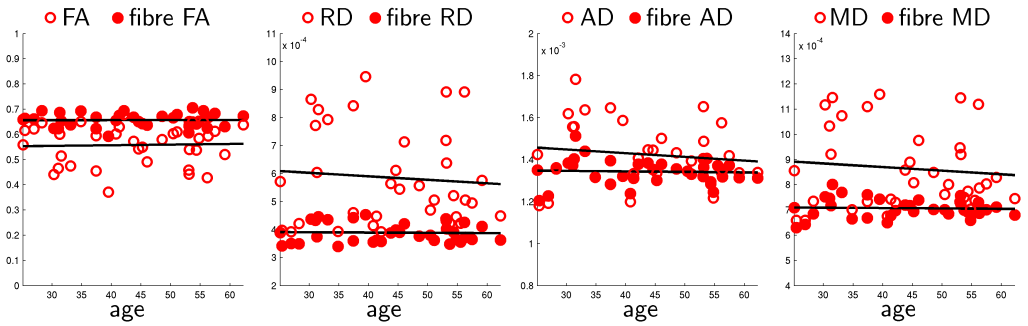

	FA	RD	AD	MD
p-value	0.84	0.65	0.44	0.57
standard error	0.0789	17.4×10^{-5}	14.6×10^{-5}	16×10^{-5}
slope (per year)	0.00026	-1.3×10^{-6}	-1.8×10^{-6}	-1.4×10^{-6}
trend	none	none	none	none

	fibre FA	fibre RD	fibre AD	fibre MD
p-value	0.95	0.86	0.8	0.81
standard error	0.0275	3.55×10^{-5}	6.21×10^{-5}	3.84×10^{-5}
slope (per year)	2.6e-05	-0.098×10^{-6}	-0.24×10^{-6}	-0.15×10^{-6}
trend	none	none	none	none

Figure A.2: Measures of water diffusion in splenium of corpus callosum. Plots: age differences and trends the across the cohort. Table: summary of regression measures.

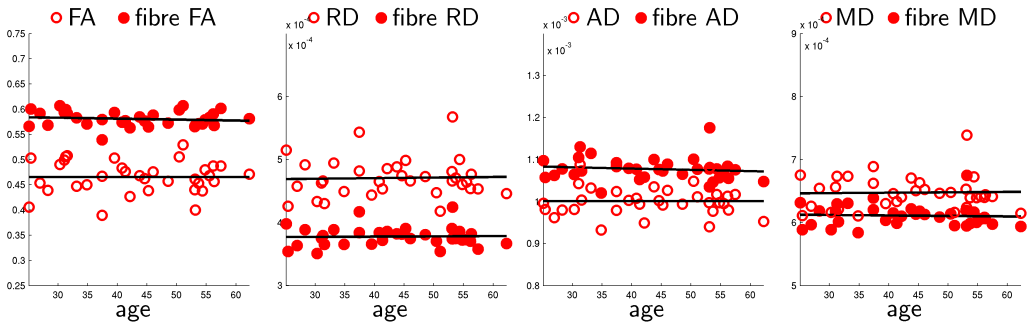

	FA	RD	AD	MD
p-value	0.99	0.85	0.99	0.88
standard error	0.0328	3.14×10^{-5}	3.54×10^{-5}	2.64×10^{-5}
slope (per year)	-3.9e-06	0.095×10^{-6}	-0.004×10^{-6}	0.062×10^{-6}
trend	none	none	none	none

	fibre FA	fibre RD	fibre AD	fibre MD
p-value	0.46	0.88	0.51	0.79
standard error	0.0151	1.61×10^{-5}	2.85×10^{-5}	1.78×10^{-5}
slope (per year)	-0.00018	0.039×10^{-6}	-0.31×10^{-6}	-0.077×10^{-6}
trend	none	none	none	none

Figure A.3: Measures of water diffusion in left arcuate fasciculus. Plots: age differences and trends the across the cohort. Table: summary of regression measures.

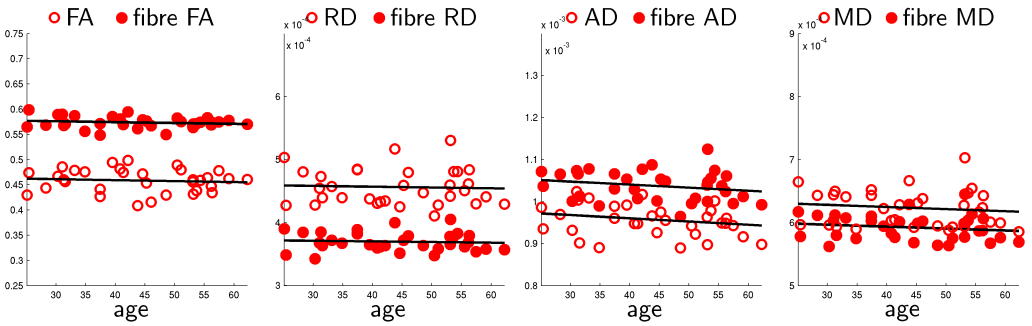

	FA	RD	AD	MD
p-value	0.61	0.79	0.25	0.49
standard error	0.0232	2.92×10^{-5}	4.01×10^{-5}	2.92×10^{-5}
slope (per year)	-0.0002	-0.13×10^{-6}	-0.77×10^{-6}	-0.34×10^{-6}
trend	none	none	none	none

	fibre FA	fibre RD	fibre AD	fibre MD
p-value	0.37	0.7	0.23	0.37
standard error	0.0116	1.51×10^{-5}	3.58×10^{-5}	2.06×10^{-5}
slope (per year)	-0.00017	-0.098×10^{-6}	-0.72×10^{-6}	-0.31×10^{-6}
trend	none	none	none	none

Figure A.4: Measures of water diffusion in right arcuate fasciculus. Plots: age differences and trends the across the cohort. Table: summary of regression measures.

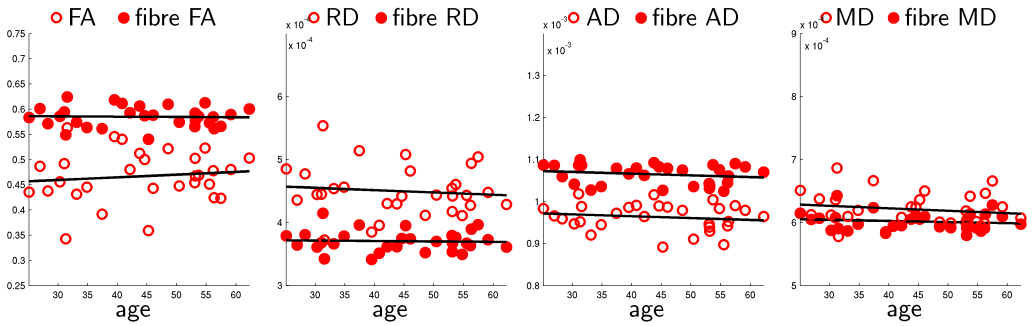

	FA	RD	AD	MD
p-value	0.54	0.59	0.43	0.39
standard error	0.0516	4.02×10^{-5}	3.25×10^{-5}	2.65×10^{-5}
slope (per year)	0.00053	-0.37×10^{-6}	-0.43×10^{-6}	-0.39×10^{-6}
trend	none	none	none	none

	fibre FA	fibre RD	fibre AD	fibre MD
p-value	0.87	0.81	0.31	0.46
standard error	0.0208	1.71×10^{-5}	2.35×10^{-5}	1.44×10^{-5}
slope (per year)	-5.8e-05	-0.068×10^{-6}	-0.41×10^{-6}	-0.18×10^{-6}
trend	none	none	none	none

Figure A.5: Measures of water diffusion in left cingulum bundle. Plots: age differences and trends the across the cohort. Table: summary of regression measures.

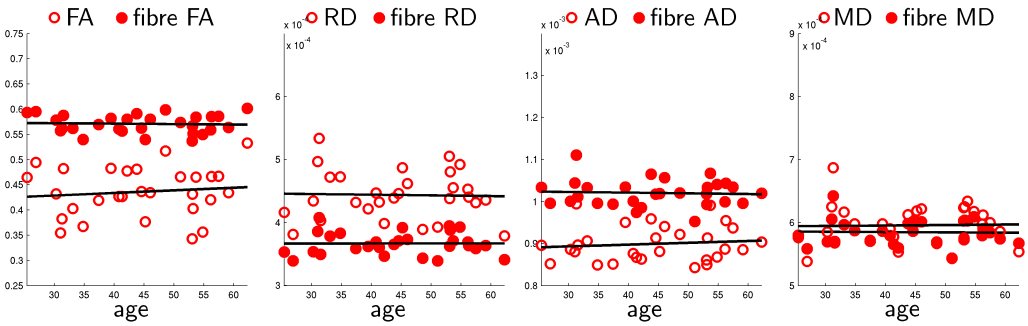

	FA	RD	AD	MD
p-value	0.56	0.88	0.57	0.9
standard error	0.0498	3.93×10^{-5}	4.28×10^{-5}	3.24×10^{-5}
slope (per year)	0.00052	-0.11×10^{-6}	0.43×10^{-6}	0.071×10^{-6}
trend	none	none	none	none

	fibre FA	fibre RD	fibre AD	fibre MD
p-value	0.8	0.98	0.78	0.89
standard error	0.0186	1.84×10^{-5}	3.25×10^{-5}	2.03×10^{-5}
slope (per year)	-8.3e-05	0.0092×10^{-6}	-0.17×10^{-6}	-0.049×10^{-6}
trend	none	none	none	none

Figure A.6: Measures of water diffusion in right cingulum bundle. Plots: age differences and trends the across the cohort. Table: summary of regression measures.

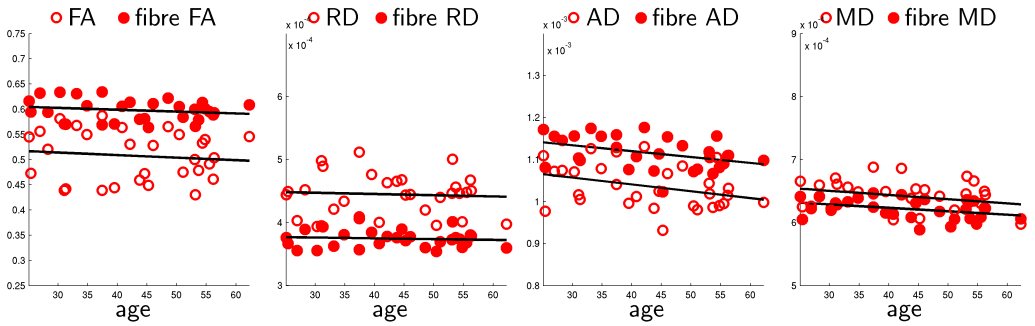

	FA	RD	AD	MD
p-value	0.55	0.74	0.065	0.13
standard error	0.0496	3.31×10^{-5}	4.96×10^{-5}	2.5×10^{-5}
slope (per year)	-0.00051	-0.19×10^{-6}	-1.6×10^{-6}	-0.67×10^{-6}
trend	none	none	none	none

	fibre FA	fibre RD	fibre AD	fibre MD
p-value	0.32	0.61	**0.031**	**0.036**
standard error	0.0214	1.41×10^{-5}	3.62×10^{-5}	1.46×10^{-5}
slope (per year)	-0.00037	-0.12×10^{-6}	-1.4×10^{-6}	-0.55×10^{-6}
trend	none	none	↘	↘

Figure A.7: Measures of water diffusion in left corticospinal tract. Plots: age differences and trends the across the cohort. Table: summary of regression measures.

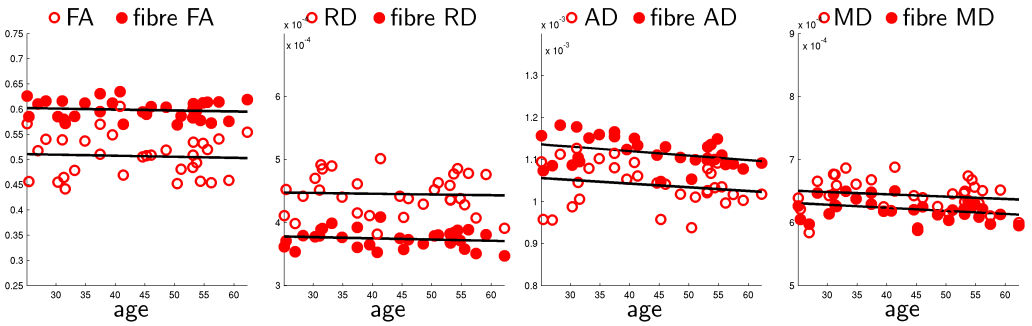

	FA	RD	AD	MD
p-value	0.76	0.82	0.28	0.39
standard error	0.0421	3.22×10^{-5}	5×10^{-5}	2.65×10^{-5}
slope (per year)	-0.00021	-0.12×10^{-6}	-0.87×10^{-6}	-0.37×10^{-6}
trend	none	none	none	none

	fibre FA	fibre RD	fibre AD	fibre MD
p-value	0.54	0.41	0.054	0.059
standard error	0.019	1.47×10^{-5}	3.34×10^{-5}	1.55×10^{-5}
slope (per year)	-0.00019	-0.2×10^{-6}	-1.1×10^{-6}	-0.49×10^{-6}
trend	none	none	none	none

Figure A.8: Measures of water diffusion in right corticospinal tract. Plots: age differences and trends the across the cohort. Table: summary of regression measures.

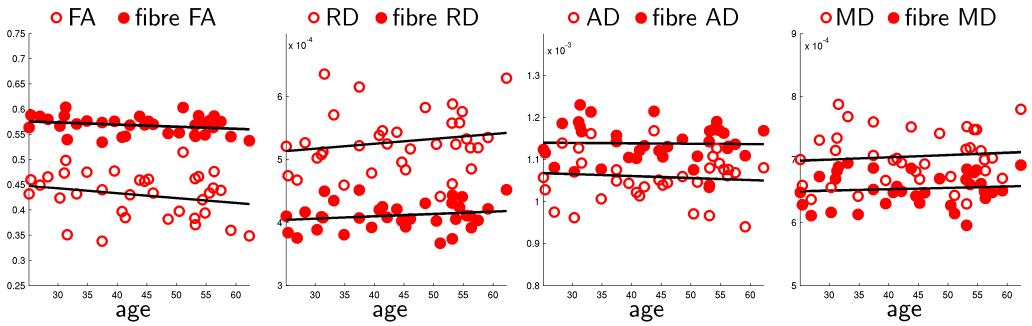

	FA	RD	AD	MD
p-value	0.17	0.29	0.61	0.59
standard error	0.044	4.69×10^{-5}	5.89×10^{-5}	4.24×10^{-5}
slope (per year)	-0.00096	0.78×10^{-6}	-0.47×10^{-6}	0.36×10^{-6}
trend	none	none	none	none

	fibre FA	fibre RD	fibre AD	fibre MD
p-value	0.15	0.29	0.9	0.6
standard error	0.0179	2.21×10^{-5}	4.45×10^{-5}	2.67×10^{-5}
slope (per year)	-0.00041	0.37×10^{-6}	-0.089×10^{-6}	0.22×10^{-6}
trend	none	none	none	none

Figure A.9: Measures of water diffusion in left inferior longitudinal fasciculus. Plots: age differences and trends the across the cohort. Table: summary of regression measures.

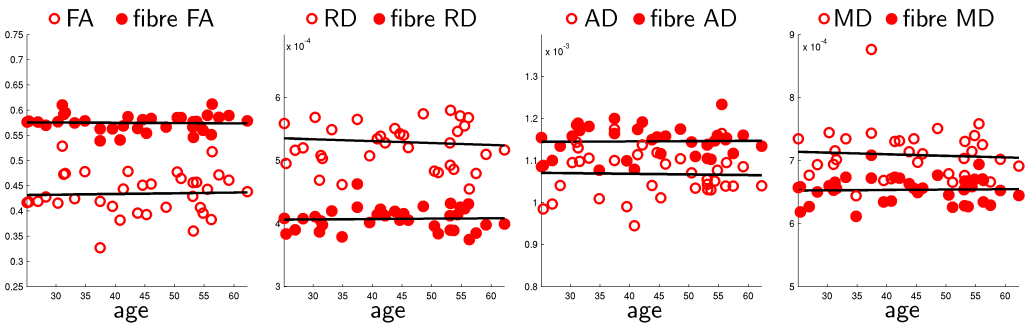

	FA	RD	AD	MD
p-value	0.84	0.69	0.86	0.7
standard error	0.0427	4.93×10^{-5}	5.39×10^{-5}	4.27×10^{-5}
slope (per year)	0.00014	-0.31×10^{-6}	-0.15×10^{-6}	-0.26×10^{-6}
trend	none	none	none	none

	fibre FA	fibre RD	fibre AD	fibre MD
p-value	0.84	0.84	0.92	0.86
standard error	0.017	1.88×10^{-5}	3.68×10^{-5}	2.16×10^{-5}
slope (per year)	-5.2e-05	0.058×10^{-6}	0.06×10^{-6}	0.058×10^{-6}
trend	none	none	none	none

Figure A.10: Measures of water diffusion in right inferior longitudinal fasciculus. Plots: age differences and trends the across the cohort. Table: summary of regression measures.

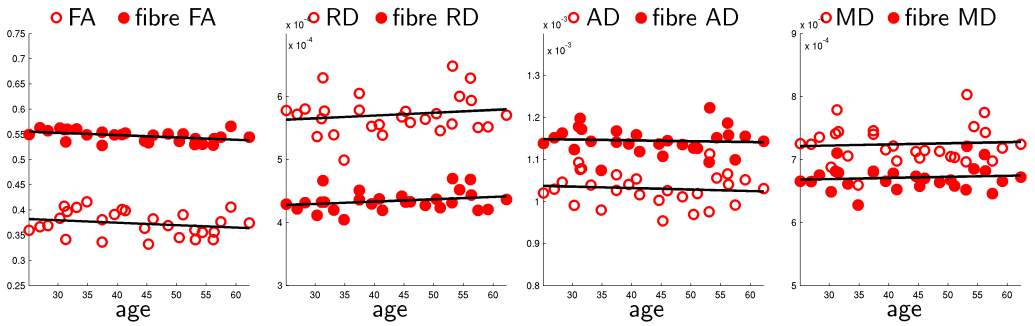

	FA	RD	AD	MD
p-value	0.26	0.43	0.6	0.74
standard error	0.0242	3.15×10^{-5}	3.89×10^{-5}	3.04×10^{-5}
slope (per year)	-0.00048	0.44×10^{-6}	-0.36×10^{-6}	0.18×10^{-6}
trend	none	none	none	none

	fibre FA	fibre RD	fibre AD	fibre MD
p-value	**0.018**	0.19	0.73	0.61
standard error	0.0104	1.57×10^{-5}	3.22×10^{-5}	1.99×10^{-5}
slope (per year)	-0.00045	0.37×10^{-6}	-0.2×10^{-6}	0.18×10^{-6}
trend	↘	none	none	none

Figure A.11: Measures of water diffusion in left uncinate fasciculus. Plots: age differences and trends the across the cohort. Table: summary of regression measures.

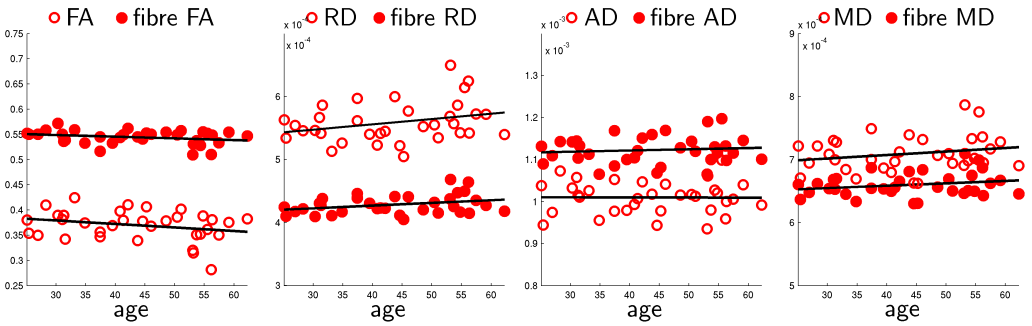

	FA	RD	AD	MD
p-value	0.14	0.093	0.97	0.23
standard error	0.0292	3.1×10^{-5}	3.94×10^{-5}	2.87×10^{-5}
slope (per year)	-0.00069	0.84×10^{-6}	-0.023×10^{-6}	0.56×10^{-6}
trend	none	none	none	none

	fibre FA	fibre RD	fibre AD	fibre MD
p-value	0.14	0.072	0.58	0.2
standard error	0.0138	1.46×10^{-5}	3.35×10^{-5}	1.85×10^{-5}
slope (per year)	-0.00033	0.43×10^{-6}	0.29×10^{-6}	0.38×10^{-6}
trend	none	none	none	none

Figure A.12: Measures of water diffusion in right uncinate fasciculus. Plots: age differences and trends the across the cohort. Table: summary of regression measures.

Tract	#	fibre FA	fibre RD	fibre AD	fibre MD	FA	RD	AD	MD
Genu of corpus callosum	35	.583 (.023)	.435 (.028)	1.25 (.048)	.707 (.03)	.459 (.049)	.553 (.059)	1.18 (.057)	.762 (.05)
Splenium of corpus callosum	35	.657 (.027)	.389 (.035)	1.34 (.061)	.707 (.038)	.558 (.078)	.586 (.17)	1.42 (.15)	.865 (.16)
Left arcuate fasciculus	34	.581 (.015)	.378 (.016)	1.08 (.028)	.611 (.018)	.466 (.032)	.471 (.031)	1 (.035)	.648 (.026)
Right arcuate fasciculus	33	.574 (.012)	.37 (.015)	1.04 (.036)	.592 (.021)	.458 (.023)	.457 (.029)	.957 (.04)	.623 (.029)
Left cingulum bundle	30	.585 (.02)	.371 (.017)	1.06 (.024)	.602 (.014)	.467 (.051)	.45 (.04)	.963 (.032)	.621 (.026)
Right cingulum bundle	29	.571 (.018)	.367 (.018)	1.02 (.032)	.585 (.02)	.436 (.049)	.444 (.039)	.9 (.042)	.596 (.032)
Left corticospinal tract	30	.598 (.021)	.375 (.014)	1.12 (.039)	.622 (.016)	.507 (.049)	.445 (.033)	1.04 (.052)	.642 (.026)
Right corticospinal tract	32	.599 (.019)	.374 (.015)	1.12 (.035)	.622 (.016)	.507 (.041)	.445 (.032)	1.04 (.05)	.644 (.026)
Left inferior longitudinal fasciculus	35	.568 (.018)	.411 (.022)	1.14 (.044)	.654 (.026)	.43 (.045)	.528 (.047)	1.06 (.058)	.705 (.042)
Right inferior longitudinal fasciculus	35	.575 (.017)	.408 (.019)	1.15 (.036)	.654 (.021)	.434 (.042)	.53 (.049)	1.07 (.053)	.709 (.042)
Left uncinate fasciculus	28	.547 (.011)	.434 (.016)	1.15 (.032)	.671 (.02)	.373 (.024)	.571 (.031)	1.03 (.038)	.725 (.03)
Right uncinate fasciculus	34	.544 (.014)	.428 (.015)	1.12 (.033)	.66 (.019)	.37 (.03)	.559 (.032)	1.01 (.039)	.709 (.029)

Table A.1: Tract averages of diffusion measures estimated with the tissue dependent diffusion and diffusion tensor models. # indicates the number of acceptable tract segmentations included in the analysis.

Bibliography

[1] A. L. Alexander, K. M. Hasan, M. Lazar, J. S. Tsuruda, and D. L. Parker. Analysis of partial volume effects in diffusion-tensor MRI. *Magn Reson Med*, 45(5):770–780, May 2001. (Cited on pages 15 and 28.)

[2] D. C. Alexander, G. J. Barker, and S. R. Arridge. Detection and modeling of non-gaussian apparent diffusion coefficient profiles in human brain data. *Magn Reson Med*, 48(2):331–340, Aug 2002. (Cited on pages 11, 17, and 20.)

[3] D. C. Alexander, P. L. Hubbard, M. G. Hall, E. A. Moore, M. Ptito, G. J. M Parker, and T. B. Dyrby. Orientationally invariant indices of axon diameter and density from diffusion MRI. *Neuroimage*, 52(4):1374–1389, Oct 2010. (Cited on page 20.)

[4] J. Ashburner and K. J. Friston. Voxel-based morphometry–the methods. *Neuroimage*, 11(6 Pt 1):805–821, Jun 2000. (Cited on pages 25 and 139.)

[5] Y. Assaf and P. J. Basser. Composite hindered and restricted model of diffusion (CHARMED) MR imaging of the human brain. *Neuroimage*, 27(1):48–58, Aug 2005. (Cited on pages 20 and 27.)

[6] Y. Assaf, R. Z. Freidlin, G. K. Rohde, and P. J. Basser. New modeling and experimental framework to characterize hindered and restricted water diffusion in brain white matter. *Magn Reson Med*, 52(5):965–978, Nov 2004. (Cited on pages 20 and 27.)

[7] A. E. Baird and S. Warach. Magnetic resonance imaging of acute stroke. *J Cereb Blood Flow Metab*, 18(6):583–609, Jun 1998. (Cited on pages 1 and 5.)

[8] P. J. Basser and D. K. Jones. Diffusion-tensor MRI: theory, experimental design and data analysis - a technical review. *NMR Biomed*, 15(7-8):456–467, 2002. (Cited on page 11.)

[9] P. J. Basser, J. Mattiello, and D. LeBihan. Estimation of the effective self-diffusion tensor from the NMR spin echo. *J Magn Reson B*, 103(3):247–254, Mar 1994. (Cited on pages 13, 14, 15, 19, 27, and 66.)

[10] P. J. Basser, S. Pajevic, C. Pierpaoli, J. Duda, and A. Aldroubi. In vivo fiber tractography using DT-MRI data. *Magn Reson Med*, 44(4):625–632, Oct 2000. (Cited on page 21.)

[11] M. E. Bastin, S. Muñoz Maniega, K. J. Ferguson, L. J. Brown, J. M. Wardlaw, A. M. J. MacLullich, and J. D. Clayden. Quantifying the effects of normal ageing on white matter structure using unsupervised tract shape modelling. *Neuroimage*, 51(1):1–10, May 2010. (Cited on page 5.)

[12] M. E. Bastin, J. P. Piątkowski, A. J. Storkey, L. J. Brown, A. M. J. Maclullich, and J. D. Clayden. Tract shape modelling provides evidence of topological change in corpus callosum genu during normal ageing. *Neuroimage*, 43(1):20–28, Oct 2008. (Cited on page 5.)

[13] M. Battaglini, S. M. Smith, S. Brogi, and N. De Stefano. Enhanced brain extraction improves the accuracy of brain atrophy estimation. *Neuroimage*, 40(2):583–589, Apr 2008. (Cited on page 92.)

[14] C. Beaulieu, F. R. Fenrich, and P. S. Allen. Multicomponent water proton transverse relaxation and T_2-discriminated water diffusion in myelinated and non-myelinated nerve. *Magn Reson Imaging*, 16(10):1201–1210, Dec 1998. (Cited on page 14.)

[15] T. E. J. Behrens, H. Johansen-Berg, S. Jbabdi, M. F. S. Rushworth, and M. W. Woolrich. Probabilistic diffusion tractography with multiple fibre orientations: What can we gain? *Neuroimage*, 34(1):144–155, Jan 2007. (Cited on pages 18, 19, 27, 66, 88, 112, and 138.)

[16] T. E. J. Behrens, M. W. Woolrich, M. Jenkinson, H. Johansen-Berg, R. G. Nunes, S. Clare, P. M. Matthews, J. M. Brady, and S. M. Smith. Characterization and propagation of uncertainty in diffusion-weighted MR imaging. *Magn Reson Med*, 50(5):1077–1088, Nov 2003. (Cited on pages 16, 19, 21, 27, 66, 88, 112, and 138.)

[17] I. J. Bennett, D. J. Madden, C. J. Vaidya, D. V. Howard, and J. H. Howard. Age-related differences in multiple measures of white matter integrity: A diffusion tensor imaging study of healthy aging. *Hum Brain Mapp*, 31(3):378–390, Mar 2010. (Cited on pages 83, 86, 87, 99, 100, 101, 106, 141, and 142.)

[18] D. Le Bihan. Looking into the functional architecture of the brain with diffusion MRI. *Nat Rev Neurosci*, 4(6):469–480, Jun 2003. (Cited on pages 4, 5, and 14.)

[19] D. Le Bihan and E. Breton. Imagerie de diffusion in-vivo par résonance. *C R Acad Sci (Paris)*, 301 (15):1109–1112, 1985. (Cited on page 13.)

[20] D. Le Bihan, E. Breton, D. Lallemand, P. Grenier, E. Cabanis, and M. Laval-Jeantet. MR imaging of intravoxel incoherent motions: application to diffusion and perfusion in neurologic disorders. *Radiology*, 161(2):401–407, Nov 1986. (Cited on page 12.)

[21] D. Le Bihan, J. F. Mangin, C. Poupon, C. A. Clark, S. Pappata, N. Molko, and H. Chabriat. Diffusion tensor imaging: concepts and applications. *J Magn Reson Imaging*, 13(4):534–546, Apr 2001. (Cited on page 45.)

[22] C. M. Bishop. *Pattern Recognition and Machine Learning*. Springer, 2006. (Cited on page 35.)

[23] F. Bloch. Nuclear induction. *Physical Review*, 70:460–473, 1946. (Cited on page 7.)

[24] S. Brooks and A. Gelman. General methods for monitoring convergence of iterative simulations. *Journal of Computational and Graphical Statistics*, 1998. (Cited on pages 47 and 50.)

[25] B. Bucur, D. J. Madden, J. Spaniol, J. M. Provenzale, R. Cabeza, L. E. White, and S. A. Huettel. Age-related slowing of memory retrieval: contributions of perceptual speed and cerebral white matter integrity. *Neurobiol Aging*, 29(7):1070–1079, Jul 2008. (Cited on pages 87 and 142.)

[26] A. Z. Burzynska, C. Preuschhof, L. Bäckman, L. Nyberg, S-C. Li, U. Lindenberger, and H. R. Heekeren. Age-related differences in white matter microstructure: region-specific patterns of diffusivity. *Neuroimage*, 49(3):2104–2112, Feb 2010. (Cited on pages 83, 86, 87, 99, 100, 101, 106, 141, and 142.)

[27] F. Calamante, J.-D. Tournier, R. M. Heidemann, A. Anwander, G. D. Jackson, and A. Connelly. Track density imaging (TDI): validation of super resolution property. *Neuroimage*, 56(3):1259–1266, Jun 2011. (Cited on pages 22, 27, and 138.)

[28] F. Calamante, J.-D. Tournier, G. D. Jackson, and A. Connelly. Track-density imaging (TDI): super-resolution white matter imaging using whole-brain track-density mapping. *Neuroimage*, 53(4):1233–1243, Dec 2010. (Cited on pages 22, 27, and 138.)

[29] F. Calamante, J.-D. Tournier, R. E. Smith, and A. Connelly. A generalised framework for super-resolution track-weighted imaging. *Neuroimage*, 59(3):2494–2503, Feb 2012. (Cited on pages 22, 27, and 138.)

[30] M. Catani and D. H. ffytche. The rises and falls of disconnection syndromes. *Brain*, 128(Pt 10):2224–2239, Oct 2005. (Cited on page 83.)

[31] M. Cercignani, M. Inglese, M. Siger-Zajdel, and M. Filippi. Segmenting brain white matter, gray matter and cerebro-spinal fluid using diffusion tensor-MRI derived indices. *Magn Reson Imaging*, 19(9):1167–1172, Nov 2001. (Cited on page 136.)

[32] O. Ciccarelli, G. J M Parker, A. T. Toosy, C. A M Wheeler-Kingshott, G. J. Barker, P. A. Boulby, D. H. Miller, and A. J. Thompson. From diffusion tractography to quantitative white matter tract measures: a reproducibility study. *Neuroimage*, 18(2):348–359, Feb 2003. (Cited on page 24.)

[33] J. D. Clayden, M. E. Bastin, and A. J. Storkey. Improved segmentation reproducibility in group tractography using a quantitative tract similarity measure. *Neuroimage*, 33(2):482–492, Nov 2006. (Cited on pages 24 and 88.)

[34] J. D. Clayden, S. Muñoz Maniega, A. J. Storkey, M. D. King, M. E. Bastin, and C. A. Clark. TractoR: Magnetic resonance imaging and tractography with R. *Journal of Statistical Software*, 44(8):1–18, 10 2011. (Cited on page 88.)

[35] J. D. Clayden, A. J. Storkey, and M. E. Bastin. A probabilistic model-based approach to consistent white matter tract segmentation. *IEEE Trans Med Imaging*, 26(11):1555–1561, Nov 2007. (Cited on pages 24 and 88.)

[36] J. D. Clayden, A. J. Storkey, S. Muñoz Maniega, and M. E. Bastin. Reproducibility of tract segmentation between sessions using an unsupervised modelling-based approach. *Neuroimage*, 45(2):377–385, Apr 2009. (Cited on pages 24 and 88.)

[37] T. E. Conturo, N. F. Lori, T. S. Cull, E. Akbudak, A. Z. Snyder, J. S. Shimony, R. C. McKinstry, H. Burton, and M. E. Raichle. Tracking neuronal fiber pathways in the living human brain. *Proc Natl Acad Sci U S A*, 96(18):10422–10427, Aug 1999. (Cited on page 21.)

[38] J. Crank. *The mathematics of diffusion*. Oxford University Press, 2nd edition, 1975. (Cited on page 2.)

[39] S. W. Davis, N. A. Dennis, N. G. Buchler, L. E. White, D. J. Madden, and R. Cabeza. Assessing the effects of age on long white matter tracts using diffusion tensor tractography. *Neuroimage*, 46(2):530–541, Jun 2009. (Cited on pages 87, 97, 107, 110, 141, and 142.)

[40] F. E. de Leeuw, J. C. de Groot, E. Achten, M. Oudkerk, L. M. Ramos, R. Heijboer, A. Hofman, J. Jolles, J. van Gijn, and M. M. Breteler. Prevalence of cerebral white matter lesions in elderly people: a population based magnetic resonance imaging study. the Rotterdam scan study. *J Neurol Neurosurg Psychiatry*, 70(1):9–14, Jan 2001. (Cited on page 84.)

[41] A. Einstein. *Investigations on the Theory of the Brownian Movement*. Dover publications, 1956. This volume contains five papers on the theory of Brownian motion originally published in German from 1905 onwards. (Cited on page 3.)

[42] C. M. Filley. White matter: organization and functional relevance. *Neuropsychol Rev*, 20(2):158–173, Jun 2010. (Cited on page 83.)

[43] L. R. Frank. Anisotropy in high angular resolution diffusion-weighted MRI. *Magn Reson Med*, 45(6):935–939, Jun 2001. (Cited on pages 14, 15, and 67.)

[44] L. R. Frank. Characterization of anisotropy in high angular resolution diffusion-weighted MRI. *Magn Reson Med*, 47(6):1083–1099, Jun 2002. (Cited on pages 18 and 20.)

[45] O. Friman, G. Farnebäck, and C.-F. Westin. A Bayesian approach for stochastic white matter tractography. *IEEE Trans Med Imaging*, 25(8):965–978, Aug 2006. (Cited on pages 17, 19, 22, 27, and 66.)

[46] O. Friman and C.-F. Westin. Uncertainty in white matter fiber tractography. *Med Image Comput Comput Assist Interv Int Conf Med Image Comput Comput Assist Interv*, 8(Pt 1):107–114, 2005. (Cited on pages 22 and 27.)

[47] M. Gallucci, S. Capoccia, and A. Catalucci. *Radiographic Atlas of Skull and Brain Anatomy*. Springer Berlin Heidelberg, 2007. (Cited on page 59.)

[48] N. Geschwind. Disconnexion syndromes in animals and man. I. *Brain*, 88(2):237–294, Jun 1965. (Cited on page 83.)

[49] N. Geschwind. Disconnexion syndromes in animals and man. II. *Brain*, 88(3):585–644, Sep 1965. (Cited on page 83.)

[50] C. D. Good, I. S. Johnsrude, J. Ashburner, R. N. Henson, K. J. Friston, and R. S. Frackowiak. A voxel-based morphometric study of ageing in 465 normal adult human brains. *Neuroimage*, 14(1 Pt 1):21–36, Jul 2001. (Cited on page 25.)

[51] P. M. Greenwood. The frontal aging hypothesis evaluated. *J Int Neuropsychol Soc*, 6(6):705–726, Sep 2000. (Cited on page 87.)

[52] E. Heiervang, T. E J Behrens, C. E. Mackay, M. D. Robson, and H. Johansen-Berg. Between session reproducibility and between subject variability of diffusion MR and tractography measures. *Neuroimage*, 33(3):867–877, Nov 2006. (Cited on page 23.)

[53] T. Heimann and H.-P. Meinzer. Statistical shape models for 3D medical image segmentation: a review. *Med Image Anal*, 13(4):543–563, Aug 2009. (Cited on page 143.)

[54] M. A. Horsfield and D. K. Jones. Applications of diffusion-weighted and diffusion tensor MRI to white matter diseases - a review. *NMR Biomed*, 15(7-8):570–577, 2002. (Cited on pages 1 and 5.)

[55] T. Hosey, G. Williams, and R. Ansorge. Inference of multiple fiber orientations in high angular resolution diffusion imaging. *Magn Reson Med*, 54(6):1480–1489, Dec 2005. (Cited on pages 18, 19, 27, and 66.)

[56] T. P. Hosey, S. G. Harding, T. A. Carpenter, R. E. Ansorge, and G. B. Williams. Application of a probabilistic double-fibre structure model to diffusion-weighted MR images of the human brain. *Magn Reson Imaging*, 26(2):236–245, Feb 2008. (Cited on pages 18, 27, and 66.)

[57] K. Hua, J. Zhang, S. Wakana, H. Jiang, X. Li, D. S. Reich, P. A. Calabresi, J. J. Pekar, P. C. M. van Zijl, and S. Mori. Tract probability maps in stereotaxic spaces: analyses of white matter anatomy and tract-specific quantification. *Neuroimage*, 39(1):336–347, Jan 2008. (Cited on page 88.)

[58] K. M. Jansons and D. C. Alexander. Persistent Angular Structure: new insights from diffusion MRI data. *Inf Process Med Imaging*, 18:672–683, Jul 2003. (Cited on pages 20 and 22.)

[59] S. Jbabdi, M. W. Woolrich, J. L R Andersson, and T. E J Behrens. A Bayesian framework for global tractography. *Neuroimage*, 37(1):116–129, Aug 2007. (Cited on pages 23, 27, and 143.)

[60] M. Jenkinson, C. F. Beckmann, T. E. J. Behrens, M. W. Woolrich, and S. M. Smith. FSL. *Neuroimage*, 62(2):782–790, Aug 2012. (Cited on pages 17, 58, and 88.)

[61] D. K. Jones. Determining and visualizing uncertainty in estimates of fiber orientation from diffusion tensor MRI. *Magn Reson Med*, 49(1):7–12, Jan 2003. (Cited on pages 16 and 70.)

[62] D. K. Jones. The effect of gradient sampling schemes on measures derived from diffusion tensor MRI: a Monte Carlo study. *Magn Reson Med*, 51(4):807–815, Apr 2004. (Cited on page 9.)

[63] D. K. Jones and M. Cercignani. Twenty-five pitfalls in the analysis of diffusion MRI data. *NMR Biomed*, 23(7):803–820, Aug 2010. (Cited on page 11.)

[64] D. K. Jones, M. R. Symms, M. Cercignani, and R. J. Howard. The effect of filter size on VBM analyses of dt-MRI data. *Neuroimage*, 26(2):546–554, Jun 2005. (Cited on page 25.)

[65] E. Kaden, A. Anwander, and T. R. Knösche. Variational inference of the fiber orientation density using diffusion MR imaging. *Neuroimage*, 42(4):1366–1380, Oct 2008. (Cited on page 20.)

[66] E. Kaden, T. R. Knösche, and A. Anwander. Parametric spherical deconvolution: inferring anatomical connectivity using diffusion MR imaging. *Neuroimage*, 37(2):474–488, Aug 2007. (Cited on page 20.)

[67] E. Kaden and F. Kruggel. Nonparametric Bayesian inference of the fiber orientation distribution from diffusion-weighted MR images. *Med Image Anal*, 16(4):876–888, May 2012. (Cited on page 20.)

[68] M. D. King, D. G. Gadian, and C. A. Clark. A random effects modelling approach to the crossing-fibre problem in tractography. *Neuroimage*, 44(3):753–768, Feb 2009. (Cited on pages 112 and 113.)

[69] E. C. Klawiter, R. E. Schmidt, K. Trinkaus, H.-F. Liang, M. D. Budde, R. T. Naismith, S.-K. Song, A. H. Cross, and T. L. Benzinger. Radial diffusivity predicts demyelination in ex vivo multiple sclerosis spinal cords. *Neuroimage*, 55(4):1454–1460, Apr 2011. (Cited on page 85.)

[70] B. W. Kreher, I. Mader, and V. G. Kiselev. Gibbs tracking: A novel approach for the reconstruction of neuronal pathways. In *Proc. Intl. Soc. Mag. Reson. Med. 16*, 2008. (Cited on page 22.)

[71] S. Kumazawa, T. Yoshiura, H. Honda, F. Toyofuku, and Y. Higashida. Partial volume estimation and segmentation of brain tissue based on diffusion tensor MRI. *Med Phys*, 37(4):1482–1490, Apr 2010. (Cited on page 137.)

[72] K. O. Lim and J. A. Helpern. Neuropsychiatric applications of DTI - a review. *NMR Biomed*, 15(7-8):587–593, 2002. (Cited on pages 1 and 5.)

[73] T. Liu, H. Li, K. Wong, A. Tarokh, L. Guo, and S. T. C. Wong. Brain tissue segmentation based on DTI data. *Neuroimage*, 38(1):114–123, Oct 2007. (Cited on page 136.)

[74] D. J. Madden, I. J. Bennett, A. Burzynska, G. G. Potter, N.-K. Chen, and A. W. Song. Diffusion tensor imaging of cerebral white matter integrity in cognitive aging. *Biochim Biophys Acta*, 1822(3):386–400, Mar 2012. (Cited on page 83.)

[75] D. J. Madden, J. Spaniol, M. C. Costello, B. Bucur, L. E. White, R. Cabeza, S. W. Davis, N. A. Dennis, J. M. Provenzale, and S. A. Huettel. Cerebral white matter integrity mediates adult age differences in cognitive performance. *J Cogn Neurosci*, 21(2):289–302, Feb 2009. (Cited on pages 5, 87, 107, and 142.)

[76] S. Muñoz Maniega, M. Bastin, A. McIntosh, S. Lawrie, and J. Clayden. Atlas-based reference tracts improve automatic white matter segmentation with neighbourhood tractography. In *Proceedings of the ISMRM 16th Scientific Meeting & Exhibition, International Society for Magnetic Resonance in Medicine*, page 3318, 2008. (Cited on pages 24 and 88.)

[77] L. Marner, J. R. Nyengaard, Y. Tang, and B. Pakkenberg. Marked loss of myelinated nerve fibers in the human brain with age. *J Comp Neurol*, 462(2):144–152, Jul 2003. (Cited on page 84.)

[78] J. A. McNab, N. L. Voets, G. Douaud, N. Jenkinson, T. Aziz, and K. L. Miller. A comparison of in vivo and ex vivo diffusion tensor imaging in the same patient. In *Proc. Intl. Soc. Mag. Reson. Med. 16*, 2008. (Cited on page 5.)

[79] K. L. Miller, C. J. Stagg, G. Douaud, S. Jbabdi, S. M. Smith, T. E. J. Behrens, M. Jenkinson, S. A. Chance, M. M. Esiri, N. L. Voets, N. Jenkinson, T. Z. Aziz, M. R. Turner, H. Johansen-Berg, and J. A. McNab. Diffusion imaging of whole, post-mortem human brains on a clinical MRI scanner. *Neuroimage*, 57(1):167–181, Jul 2011. (Cited on page 86.)

[80] S. Mori, B. J. Crain, V. P. Chacko, and P. C. van Zijl. Three-dimensional tracking of axonal projections in the brain by magnetic resonance imaging. *Ann Neurol*, 45(2):265–269, Feb 1999. (Cited on page 21.)

[81] M. E. Moseley, Y. Cohen, J. Kucharczyk, J. Mintorovitch, H. S. Asgari, M. F. Wendland, J. Tsuruda, and D. Norman. Diffusion-weighted MR imaging of anisotropic water diffusion in cat central nervous system. *Radiology*, 176(2):439–445, Aug 1990. (Cited on pages 1 and 5.)

[82] M. E. Moseley, J. Kucharczyk, H. S. Asgari, and D. Norman. Anisotropy in diffusion-weighted MRI. *Magn Reson Med*, 19(2):321–326, Jun 1991. (Cited on pages 1 and 5.)

[83] R. V. Mulkern, H. Gudbjartsson, C. F. Westin, H. P. Zengingonul, W. Gartner, C. R. Guttmann, R. L. Robertson, W. Kyriakos, R. Schwartz, D. Holtzman, F. A. Jolesz, and S. E. Maier. Multi-component apparent diffusion coefficients in human brain. *NMR Biomed*, 12(1):51–62, Feb 1999. (Cited on page 13.)

[84] R. M. Neal. Probabilistic Inference Using Markov Chain Monte Carlo Methods. Technical report, University of Toronto, 1993. (Cited on page 35.)

[85] J. Neil, J. Miller, P. Mukherjee, and P. S. Hüppi. Diffusion tensor imaging of normal and injured developing human brain - a technical review. *NMR Biomed*, 15(7-8):543–552, 2002. (Cited on pages 1 and 5.)

[86] T. Niendorf, R. M. Dijkhuizen, D. G. Norris, M. van Lookeren Campagne, and K. Nicolay. Biexponential diffusion attenuation in various states of brain tissue: implications for diffusion-weighted imaging. *Magn Reson Med*, 36(6):847–857, Dec 1996. (Cited on page 13.)

[87] M. O'Sullivan, D. K. Jones, P. E. Summers, R. G. Morris, S. C. Williams, and H. S. Markus. Evidence for cortical "disconnection" as a mechanism of age-related cognitive decline. *Neurology*, 57(4):632–638, Aug 2001. (Cited on page 87.)

[88] G. J. M. Parker and D. C. Alexander. Probabilistic anatomical connectivity derived from the microscopic persistent angular structure of cerebral tissue. *Philos Trans R Soc Lond B Biol Sci*, 360(1457):893–902, May 2005. (Cited on page 22.)

[89] O. Pasternak, Y. Assaf, N. Intrator, and N. Sochen. Variational multiple-tensor fitting of fiber-ambiguous diffusion-weighted magnetic resonance imaging voxels. *Magn Reson Imaging*, 26(8):1133–1144, Oct 2008. (Cited on page 111.)

[90] O. Pasternak, N. Sochen, Y. Gur, N. Intrator, and Y. Assaf. Free water elimination and mapping from diffusion MRI. *Magn Reson Med*, 62(3):717–730, Sep 2009. (Cited on pages 18, 19, 27, 111, and 137.)

[91] A. Peters. The effects of normal aging on myelin and nerve fibers: a review. *J Neurocytol*, 31(8-9):581–593, 2002. (Cited on page 84.)

[92] A. Pfefferbaum and E. V. Sullivan. Increased brain white matter diffusivity in normal adult aging: relationship to anisotropy and partial voluming. *Magn Reson Med*, 49(5):953–961, May 2003. (Cited on page 85.)

[93] A. Pfefferbaum, E. V. Sullivan, M. Hedehus, K. O. Lim, E. Adalsteinsson, and M. Moseley. Age-related decline in brain white matter anisotropy measured

with spatially corrected echo-planar diffusion tensor imaging. *Magn Reson Med*, 44(2):259–268, Aug 2000. (Cited on pages 5, 85, and 87.)

[94] C. Pierpaoli, A. Barnett, S. Pajevic, R. Chen, L. R. Penix, A. Virta, and P. Basser. Water diffusion changes in wallerian degeneration and their dependence on white matter architecture. *Neuroimage*, 13(6 Pt 1):1174–1185, Jun 2001. (Cited on page 45.)

[95] J. A. Sanders. *Functional Brain Imaging*, chapter 4 - Magnetic Resonance Imaging. Mosby-Year Book, St. Louis, MO, 1995. (Cited on page 6.)

[96] K. Schmierer, C. A. M. Wheeler-Kingshott, D. J. Tozer, P. A. Boulby, H. G. Parkes, T. A. Yousry, F. Scaravilli, G. J. Barker, P. S. Tofts, and D. H. Miller. Quantitative magnetic resonance of postmortem multiple sclerosis brain before and after fixation. *Magn Reson Med*, 59(2):268–277, Feb 2008. (Cited on page 85.)

[97] S. Smith, J. McNab, and K. Miller. Partial-volume modelling in diffusion MRI. In *Proc. Intl. Soc. Mag. Reson. Med. 16*, 2008. (Cited on page 28.)

[98] S. M. Smith. Fast robust automated brain extraction. *Hum Brain Mapp*, 17(3):143–155, Nov 2002. (Cited on pages 58 and 92.)

[99] S. M. Smith, M. Jenkinson, H. Johansen-Berg, D. Rueckert, T. E. Nichols, C. E. Mackay, K. E. Watkins, O. Ciccarelli, M. Zaheer Cader, P. M. Matthews, and T. E. J. Behrens. Tract-based spatial statistics: voxelwise analysis of multi-subject diffusion data. *Neuroimage*, 31(4):1487–1505, Jul 2006. (Cited on pages 25 and 141.)

[100] S. M. Smith, M. Jenkinson, M. W Woolrich, C. F. Beckmann, T. E. J. Behrens, H. Johansen-Berg, P. R. Bannister, M. De Luca, I. Drobnjak, D. E. Flitney, R. K. Niazy, J. Saunders, J. Vickers, Y. Zhang, N. De Stefano, J. M. Brady, and P. M. Matthews. Advances in functional and structural MR image analysis and implementation as FSL. *Neuroimage*, 23 Suppl 1:S208–S219, 2004. (Cited on pages 17, 58, and 88.)

[101] S.-K. Song, S.-W. Sun, W.-K. Ju, S.-J. Lin, A. H. Cross, and A. H. Neufeld. Diffusion tensor imaging detects and differentiates axon and myelin degeneration in mouse optic nerve after retinal ischemia. *Neuroimage*, 20(3):1714–1722, Nov 2003. (Cited on pages 84 and 85.)

[102] S.-K. Song, J. Yoshino, T. Q. Le, S.-J. Lin, S.-W. Sun, A. H. Cross, and R. C. Armstrong. Demyelination increases radial diffusivity in corpus callosum of mouse brain. *Neuroimage*, 26(1):132–140, May 2005. (Cited on page 85.)

[103] E. O. Stejskal and J. E. Tanner. Spin diffusion measurements: Spin echoes in the presence of a timeâĂŘdependent field gradient. *J. Chem. Phys.*, 42:288, 1965. (Cited on page 13.)

[104] A. L. Sukstanskii and D. A. Yablonskiy. Effects of restricted diffusion on MR signal formation. *J Magn Reson*, 157(1):92–105, Jul 2002. (Cited on page 14.)

[105] E. V. Sullivan, E. Adalsteinsson, and A. Pfefferbaum. Selective age-related degradation of anterior callosal fiber bundles quantified in vivo with fiber tracking. *Cereb Cortex*, 16(7):1030–1039, Jul 2006. (Cited on pages 5, 85, and 87.)

[106] E. V Sullivan and A. Pfefferbaum. Diffusion tensor imaging and aging. *Neurosci Biobehav Rev*, 30(6):749–761, 2006. (Cited on pages 1 and 87.)

[107] E. V Sullivan, T. Rohlfing, and A. Pfefferbaum. Quantitative fiber tracking of lateral and interhemispheric white matter systems in normal aging: relations to timed performance. *Neurobiol Aging*, 31(3):464–481, Mar 2010. (Cited on pages 87 and 101.)

[108] E. V Sullivan, N. M. Zahr, T. Rohlfing, and A. Pfefferbaum. Fiber tracking functionally distinct components of the internal capsule. *Neuropsychologia*, 48(14):4155–4163, Dec 2010. (Cited on page 87.)

[109] S.-W. Sun, H.-F. Liang, A. H. Cross, and S.-K. Song. Evolving Wallerian degeneration after transient retinal ischemia in mice characterized by diffusion tensor imaging. *Neuroimage*, 40(1):1–10, Mar 2008. (Cited on pages 84 and 85.)

[110] S.-W. Sun, H.-F. Liang, T. Q. Le, R. C. Armstrong, A. H. Cross, and S.-K. Song. Differential sensitivity of in vivo and ex vivo diffusion tensor imaging to evolving optic nerve injury in mice with retinal ischemia. *Neuroimage*, 32(3):1195–1204, Sep 2006. (Cited on pages 84 and 85.)

[111] Y. Tang, J. R. Nyengaard, B. Pakkenberg, and H. J. Gundersen. Age-induced white matter changes in the human brain: a stereological investigation. *Neurobiol Aging*, 18(6):609–615, 1997. (Cited on page 84.)

[112] H. C. Torrey. Bloch equations with diffusion terms. *Phys. Rev.*, 104:563–565, Nov 1956. (Cited on page 13.)

[113] J.-D. Tournier, F. Calamante, and A. Connelly. Robust determination of the fibre orientation distribution in diffusion MRI: non-negativity constrained super-resolved spherical deconvolution. *Neuroimage*, 35(4):1459–1472, May 2007. (Cited on page 20.)

[114] J.-D. Tournier, F. Calamante, D. G. Gadian, and A. Connelly. Direct estimation of the fiber orientation density function from diffusion-weighted MRI data using spherical deconvolution. *Neuroimage*, 23(3):1176–1185, Nov 2004. (Cited on page 20.)

[115] J.-D. Tournier, S. Mori, and A. Leemans. Diffusion tensor imaging and beyond. *Magn Reson Med*, 65(6):1532–1556, Jun 2011. (Cited on page 11.)

[116] D. S. Tuch, T. G. Reese, M. R. Wiegell, and V. J. Wedeen. Diffusion MRI of complex neural architecture. *Neuron*, 40(5):885–895, Dec 2003. (Cited on page 19.)

[117] M. W. Vernooij, M. de Groot, A. van der Lugt, M. A. Ikram, G. P. Krestin, A. Hofman, W. J. Niessen, and M. M B Breteler. White matter atrophy and lesion formation explain the loss of structural integrity of white matter in aging. *Neuroimage*, 43(3):470–477, Nov 2008. (Cited on page 84.)

[118] S. B. Vos, D. K. Jones, M. A. Viergever, and A. Leemans. Partial volume effect as a hidden covariate in DTI analyses. *Neuroimage*, 55(4):1566–1576, Apr 2011. (Cited on pages 85, 86, and 137.)

[119] R. L. West. An application of prefrontal cortex function theory to cognitive aging. *Psychol Bull*, 120(2):272–292, Sep 1996. (Cited on page 87.)

[120] C. A. M. Wheeler-Kingshott and M. Cercignani. About "axial" and "radial" diffusivities. *Magn Reson Med*, 61(5):1255–1260, May 2009. (Cited on page 85.)

[121] M. W. Woolrich, S. Jbabdi, B. Patenaude, M. Chappell, S. Makni, T. Behrens, C. Beckmann, M. Jenkinson, and S. M. Smith. Bayesian analysis of neuroimaging data in FSL. *Neuroimage*, 45(1 Suppl):S173–S186, Mar 2009. (Cited on pages 17, 58, and 88.)

[122] Y. Zhang, M. Brady, and S. Smith. Segmentation of brain MR images through a hidden Markov random field model and the expectation-maximization algorithm. *IEEE Trans Med Imaging*, 20(1):45–57, Jan 2001. (Cited on pages 65, 92, and 139.)

[123] Y. Zhang, A.-T. Du, S. Hayasaka, G.-H. Jahng, J. Hlavin, W. Zhan, M. W. Weiner, and N. Schuff. Patterns of age-related water diffusion changes in human brain by concordance and discordance analysis. *Neurobiol Aging*, 31(11):1991–2001, Nov 2010. (Cited on pages 97 and 107.)